CHARACTERIZATION OF HUMAN ISLET AMYLOID PEPTIDE VIA IM-MS AND INFRARED SPECTROSCOPY

MASTER THESIS
Freie Universität Berlin

Accomplished at the Molecular Physics Department

of the Fritz Haber Institute of the Max Planck Society

January to July 2019

MICHELE CRISTINE DOS SANTOS PUGINI

Freie Universität Berlin

MAX-PLANCK-GESELLSCHAFT
FRITZ-HABER-INSTITUT

I, Michele Cristine dos Santos Pugini, born December 1991 in Porto Ferreira (Brazil), confirm that I have prepared the master thesis entitled “Characterization of Human Islet Amyloid Peptide via IM-MS and Infrared Spectroscopy” independently and exclusively by myself using only the sources and supports specified in this work.

First Examiner: Prof. Dr. Kevin Pagel

Second Examiner: Prof. Dr. Beate Koksch

ABSTRACT

Protein-misfolding, aggregation and accumulation of insoluble deposits are the hallmark features of a variety of human diseases such as Parkinson's disease and diabetes mellitus type II. The latter is a systemic disorder characterized by insulin resistance, impaired insulin secretion, β-cell apoptosis and islet amyloid formation. Fibrillar aggregates from the self-assembly of human islet amyloid polypeptide (hIAPP) are major component of islet amyloids. Accumulating evidence suggests that not the mature fibrils, but rather smaller, soluble, polymorphic and highly dynamic oligomers preceding the formation of the fibrils are the cytotoxic species. A detailed insight into the structures of the oligomeric intermediates is crucial for identification of potential targets and development of therapeutic strategies. However, the polydisperse nature of these peptides makes their structural characterization challenging. The traditional condensed-phase analytical techniques provide only averaged structural information on the dynamic ensemble. However, information on the structure of isolated species can be obtained by employing gas-phase techniques. Here, infrared action spectroscopy in combination with ion-mobility spectrometry is used to gain insight into the secondary structure of these isolated peptides. The orthogonal combination of these techniques allows to obtain fingerprint vibrational spectra of *m/z*- and conformer-selected species. The secondary structure of the full-length hIAPP, as well as of metal-associated hIAPP and hIAPP in heterogeneous co-assemblies with a fragment of the prion protein ($PrP_{106\text{-}126}$) and the hexapeptide VEALYL were investigated. The obtained data suggests that the secondary structure of the monomeric hIAPP contains a significant fraction of α-helical motifs, which is seemingly maintained upon metal binding, self-assembly, or heterogeneous co-assembly with other peptides. These results provide solid evidence for the importance of helical intermediates in the formation of amyloids.

ACKNOWLEDGMENTS

I would first like to thank Prof. Dr. Gert von Helden and Prof. Dr. Kevin Pagel for accepting me into the group and trusting me to do this work.

I am especially grateful to Prof. Dr. Gert von Helden for his support, guidance during the research and for giving me such an interesting research topic to work with.

I would also like to thank Prof. Dr. Gert von Helden and Prof. Dr. Gerard Meijer for providing the all the equipment and infrastructure necessary to conduct this work.

To Prof. Dr. Kevin Pagel and Prof. Dra. Beate Koksch: Thank you for your time and willingness to evaluate this thesis.

A special thanks to Maike Lettow for all the support and for the patience to teach me how to operate the equipment. Also, for helping me to develop a critical and scientific thinking, making the long hours of beamtime more enjoyable and for teaching me how to be a more responsible and mature (should I say more organized?) person.

I would also like to thank Christian Manz for motivating me since I joined the group.

I am also very greatfull to Eike Mucha, Rayoon Chang, Kim Greis, Carla Kirschbaum, Clemens Richter, Lukas Polawski, Markó Grabárics and Daniel Thomas. Thank you for all your help and support.

Lastly, I would like to thank my family and friends, many of whom are overseas but who have always been supporting me regardless the distance.

TABLE OF CONTENTS

LIST OF ABBREVIATIONS

18c6	18-crown-6
AD	Alzheimer's disease
AFM	Atomic force microscopy
AMP	Antimicrobial peptides
ATD	Arrival time distribution
ATR-FTIR	Attenuated total reflection FTIR
CCS	Collision cross section
CD	Circular dichroism
Db30c10	dibenzo-30-crown-10
DT	Drift tube
EM	Electron microscopy
ESI	Electrospray ionization
FT-IR	Fourier transform infrared
FWHM	Full width half maximum
hIAPP	Human islet amyloid polypeptide
IAPP	Islet amyloid polypeptide
IDP	Intrinsically disordered protein
IM-MS	ion mobility-mass spectrometry
IR	Infrared
IRE	internal reflection element
IRMPD	Infrared Multiple Photon Dissociation
MD	Molecular dynamics
NMR	Nuclear magnetic resonance
PG-1	Protegrin-1
REMD	Replica exchange molecular dynamics
rIAPP	Rat islet amyloid polypeptide
T2D	Diabetes mellitus type II
TEM	Transmission electron microscopy
TOF	Time-of-flight

1. INTRODUCTION

Diabetes mellitus type II (T2D), Parkinson's disease (PD), Alzheimer's disease (AD) and other neurodegenerative diseases share as a common pathological characteristic the formation of amyloid plaques. These amyloid plaques consist of insoluble aggregates of fibrous morphology rich in β-sheet secondary structures.[1-3] Considering the observation of these structures *in vivo*, they were for a long time considered to be the toxic species behind those pathologies.[4] However, studies carried out in recent years have shown that the neurotoxic species are the intermediary structures that anticipate the formation of fibrillary aggregates.[4] These species are highly dynamic and polydisperse oligomers ranging from dimers to protofibrils. Elucidating the precise structure of pre-fibrillar oligomers and the mechanism that leads monomers to fibrils is crucial not only for the selective modulation of the aggregation process, but also helps to clarify fundamental questions about the nature of protein folding.[5, 6]

However, due to their polydisperse, polymorphic and transient nature, these pre-fibrillar oligomers exist in rapid equilibrium between different stoichiometric and conformational states.[7] The characterization of the soluble oligomers using condensed-phase techniques does not provide structural information of the oligomeric species individually, but rather, average information of the ensemble.[5, 8] In order to obtain structural information on isolated species, gas-phase techniques, especially ion mobility spectrometry coupled to mass spectrometry (IM-MS), have been employed in the analysis and characterization of isolated oligomers in the presence of other species. The combination of these two techniques allows the selection of molecular ions based on their mass as well as on their shape and spatial conformations. Therefore IM-MS turned out to be an outstanding tool for the analysis of non-covalently associated protein complexes.[9] The ability of this technique relies on the advent of soft-ionization methods such as electrospray ionization (ESI), which allows the transfer of biomolecules from solution into the gas-phase environment while keeping its native structure. Yet, this analytical approach itself does not provide direct information on the motifs making up the secondary structures of individual toxic oligomers. To overcome this limitation, IM-MS can further be coupled to other orthogonal analytical techniques, such as infrared spectroscopy. Highly secondary structure-sensitive gas-phase IR spectroscopy is then performed on *m/z*- and conformer-preselected early oligomeric intermediates of amyloid-forming species.

One example among well-studied amyloid-forming peptides is the human islet amyloid polypeptide (hIAPP), the major protein component of pancreatic islet amyloidosis which is associated with the pathogeny of type II diabetes (T2D).[10] Pancreatic islet amyloidosis contributes to β-cell dysfunction, cell death, progression of T2D as well as to other complications.[4] In its native state, hIAPP is soluble and mainly monomeric but forms islet amyloids in T2D. Still, little is known about the molecular nature of the toxic hIAPP species, the mechanism of hIAPP amyloid formation and the mechanism of cytotoxicity is not fully understood. However, it has been settled that its toxicity is conformation-dependent.[4] In addition, hIAPP shares the same secretory pathway with the hormone insulin and also high concentrations of zinc and copper ions have been detected in the pancreatic β-cells.[11] These findings raise the question about the role of metal binding and heterogeneous co-association of peptides on hIAPP aggregation.

In this thesis, the structures of early hIAPP intermediates were investigated by a combination of gas-phase techniques, namely IM-MS and IR spectroscopy and furthermore by traditional condensed-phase IR spectroscopy. Likewise, the effect of metal-association and hetero-oligomerization on the aggregation behavior of the investigated intermediates is investigated in the course of the presented work.

2. FUNDAMENTALS

2.1 The Amyloid State of Human Islet Amyloid Polypeptide

2.1.1 AMYLOID DEFINITION

Several neurodegenerative and systemic disorders such as Alzheimer's and Parkinson's disease, prion disease and type 2 diabetes mellitus share the deposition of amyloid plaques as their primary trait. The term amyloid was first used to describe abnormal extracellular deposits of insoluble proteins showing an amylopectin-like aspect.[10] These proteins entering the so-called amyloid state are referred to as intrinsically disordered proteins (IDPs) and in the amyloids found in vivo they form elongated, unbranched fibers composed of many-stranded β-sheets.[1, 12] This operational definition of amyloid has been adopted by the community of pathologists.[1] Additionally, the amyloid fibrils bind the dye Congo red or thioflavine T (ThT) and show green birefringence when viewed between polarizers.[12]

Since amyloid formation has also been observed *in vitro* and similar fibers are formed by denatured proteins[13], a molecular-based definition has been adopted by biophysicists. This definition excludes the requirement that the fibers have to be extracellular and disease related. According to this structure-related definition, amyloid fibers display the *cross-β fiber diffraction pattern* (Figure 1)[1], an X-ray diffraction signature.[14] This pattern reveals that the fibril's most notable repeating feature is a set of β-sheets parallel to the fiber axis. The hydrogen-bonded strands are perpendicular to this axis and the β-sheets can be either parallel or antiparallel. Additionally, the sheets adopt an "in register" arrangement where their side chains are on top of one another along the fibril axis[1].The separation distance between identical side chains is 4.8 Å in parallel sheets and 9.6 Å in antiparallel sheets.[1]

Short segments of amyloid-forming proteins that form microcrystals and fibers with similar morphology to the entire protein fibers have been used for the determination of the architecture of cross-β spines.[14] These studies revealed that the amyloid protofilament consists of β-sheets running along the length of the crystals.[1] The side chains of the sheets within the protofilament are tightly interdigitated resembling the teeth of a zipper. The steric zippers are classified according to their sheet-to-sheet arrangement: (i) face to face (class 1), (ii) face to back (classes 2 and 4), (iii) pack with opposite edges up (class 4), (iv) with antiparallel strands (classes 5-8). Figure 2 shows the atomic structures of steric-zipper protofilaments from amyloid-forming proteins. Many proteins contain several steric zipper-forming segments from different classes within their primary sequences, and therefore, some amyloid spines can be formed by different steric zippers from the same protein.[1]

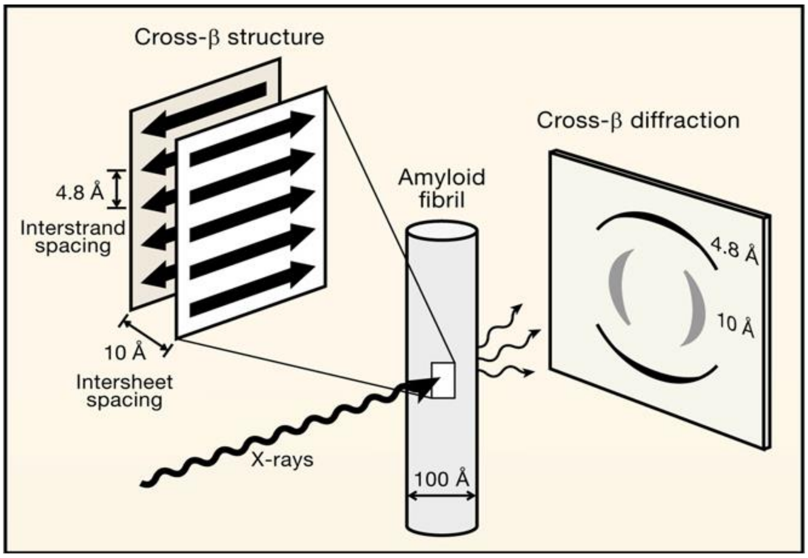

Figure 1.The characteristic diffraction pattern observed for cross-β structures when X-ray is directed on amyloid fibers. Figure taken from Eisenberg *et al.*[1]

IDPs may enter the amyloid state when a segment has backbone amide N-H and C=O groups exposed, allowing their coupling into hydrogen bonds with other protein chains. The process of amyloid formation initiates with the lag phase. During the lag-phase, unfolding/misfolding of the monomers generates species capable of undergoing oligomerization.[15] Three or four protein molecules expose their amyloid-forming segments forming a stable oligomer nucleus which template the bonding pattern of the fiber spine.[14] Since formation of stable oligomeric nuclei is a thermodynamically unfavoured process, the lag phase is the rate-determining step of amyloid formation.[16] Taking this into account, only exposure of amyloid-forming segments is not sufficient for amyloid formation. The monomer concentration must be high enough to overcome the entropy against formation of ordered fibers. Formation of the nucleus initiates the elongation phase, where monomers can join the nucleus which grows and extends at an exponential rate to fibrils. Moreover, breakage of the fibrils supply new fibril ends for elongation, and thus affect the kinetics of fibrillar growth.[1] Finally, the saturation phase is reached when the monomer concentration is critically low and fibril elongation is terminated (Figure 3). The rate-limiting lag-phase can be circumvented in the pre-formed nuclei. These nuclei can act as fibrillar seeds that template monomer refolding and assembly into amyloid fibrils.[5, 16]

Among all the species formed during the process of amyloid formation, the mature fibrils are the most thoroughly investigated species due to their high stability.[16] While fibrils can be identified by the above mentioned methods congo red and ThT assays, atomic force microscopy (AFM) and transmission electron microscopy (TEM) are the methods of choice for the classification of peptide self-assemblies such as oligomers, proto-fibrils and amyloid fibrils consisted of varying numbers of strands and amorphous aggregates.[16, 17] Secondary structure transition during amyloid formation have been monitored using circular dichroism (CD), fourier-transform infrared (FTIR) and nuclear magnetic resonance (NMR) spectroscopy.[16] However, accumulating evidence has attributed toxicity not to the mature fibrils but to the transient oligomers populating the lag phase. Due to their highly dynamic and transient nature, characterization of the toxic oligomeric species is still challenging and, to date, the mechanism leading from monomers to aggregates remains unclear.

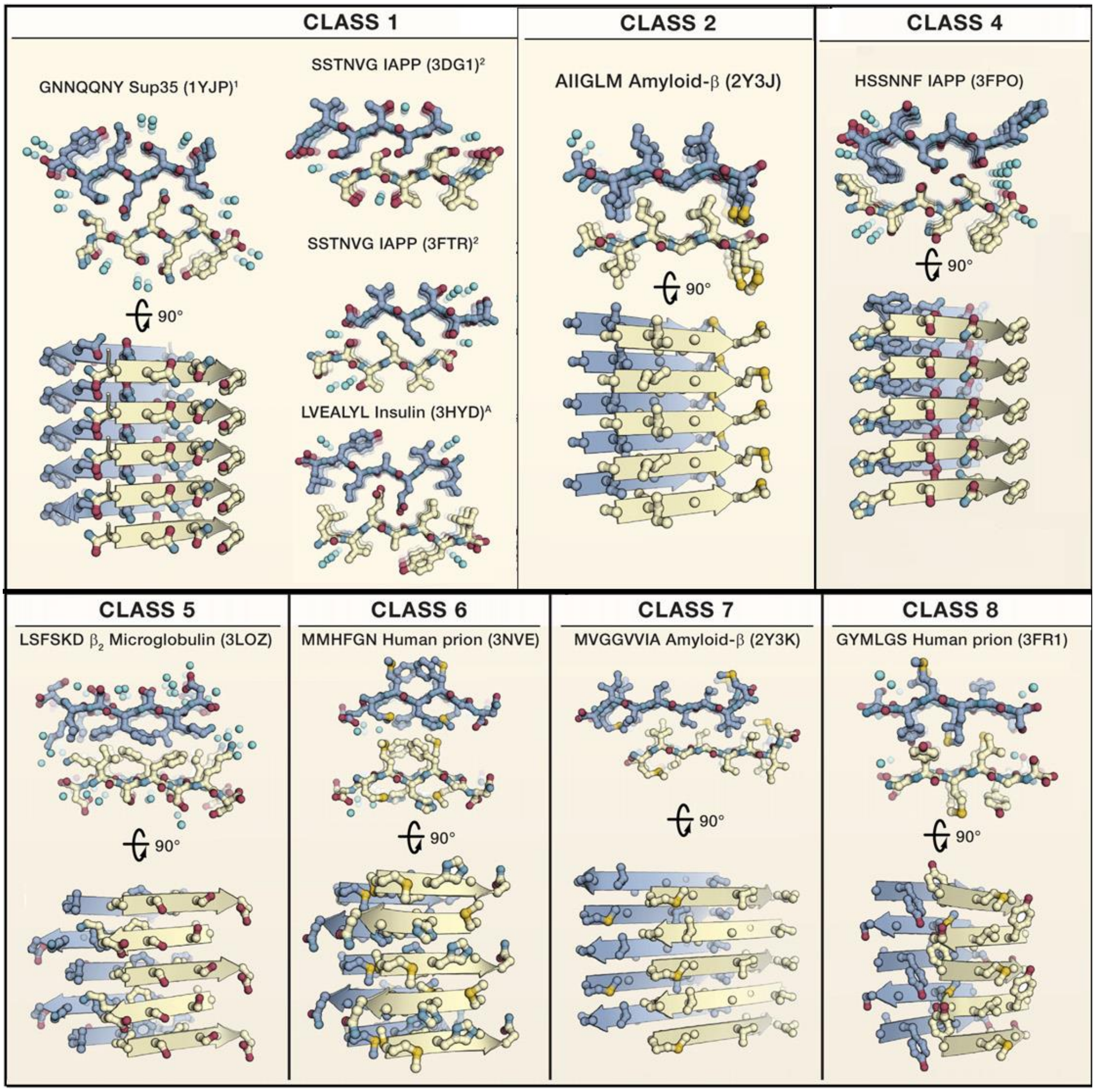

Figure 2. Atomic structures of steric zippers protofilaments from amyloidogenic proteins. Figure taken from Eisenberg *et al.*[1]

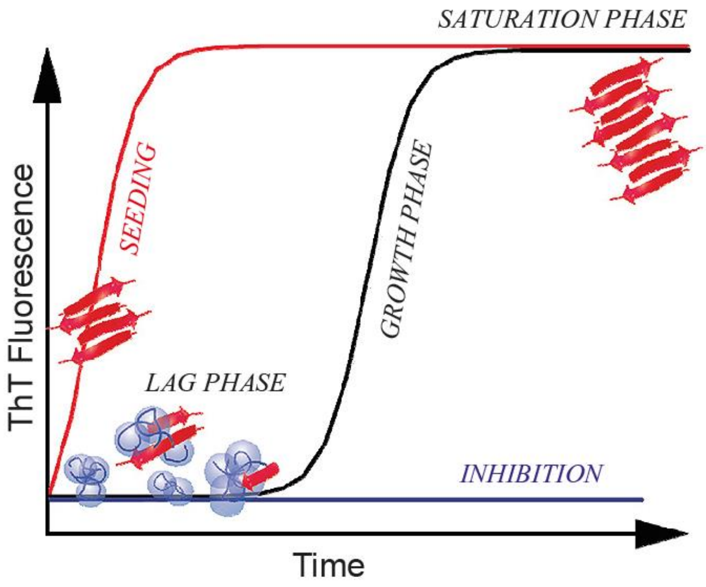

Figure 3. Amyloid formation pathway. Figure adapted from Hoffmann *et al.*[5]

2.1.2 BIOLOGICAL ROLE OF hIAPP

hIAPP is a 37-residue peptide and the major component in the islet amyloids in the pancreas (these pancreatic islets are also known as the islets of Langerhans). The peptide is translated as an 89-residue long pre-pro hormone and is matured along with insulin through the secretory pathway.[18] Cleavage of a 22-residue signal peptide and formation of an intramolecular disulfide bridge upon transporting the protein from the endoplasmic reticulum (ER) to the trans-Golgi network yields the pro-form (pro-IAPP). Pro-IAPP is further processed in the Golgi and insulin secretory granules. The prohormone convertases PC2 and PC1/3 cleave the N- and C-terminal flanking peptides.[18] Finally, carboxypeptidase E catalyzes the cleavage of the dibasic residues to form a Gly, which is then amidated by the peptidyl amidating mono-oxygenase complex (see Figure 4).[19]

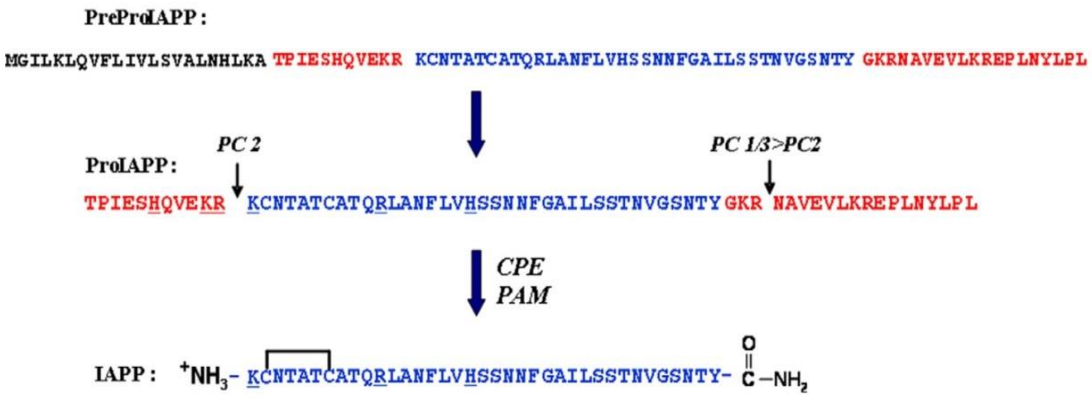

Figure 4. Processing of human PreProIAPP to form mature IAPP. Figure taken from Cao *et al.*[19]

hIAPP is co-secreted with insulin from the β-cells according to nutrient influx.[10, 19] Its physiological function is not fully understood, but the conserved sequence homology species imply functional significance.[10] The peptide has the function of an anorectic hormone in the central nervous system, reducing caloric intake, controlling gastric emptying[20] and maintaining glucose homeostasis.[21] hIAPP is believed to be involved in regulating the secretion of glucagon[16, 22-24] and to play a role in regulating the glucose levels in blood by inhibiting insulin secretion from the pancreas.[22]

The peptide is stored in the halo region of the insulin secretory granules while insulin is localized in the dense core of the granule.[19] Its small size, fast dynamics and unstable secondary structure are linked to its inherent tendency to aggregate into insoluble fibrils.[25] These aggregates are the major component of the extracellular amyloid plaques observed in pancreatic islets of patients with T2D[10] which is characterized by insulin resistance, defective insulin secretion, loss of β-cell mass and β-cell apoptosis.[20, 26] However, the hIAPP concentration in secretory vesicles is in the millimolar range and is much higher than the concentration required to promote rapid amyloid formation *in vitro.*[16] This suggests that a series of factors such as intragranular pH, interaction with insulin, interaction with metal ions and oxidative stress may play a role on inhibition or stimulation of hIAPP aggregation.

Although T2D has been associated with extracellular accumulation of amyloid deposits, there is sufficient evidence that hIAPP aggregation starts in intracellular spaces. As pro-IAPP was also observed in amyloid deposits[27], it is suggested that it acts as an aggregation template for further hIAPP accumulation intra- and extracellularly.[20] Intracellular oligomerization and fibrillation are thus proposed to be the first steps of the hIAPP-induced cytotoxicity which is associated to disruption of the membrane integrity.[16] Three models for the hIAPP-mediated membrane disruption have been proposed (Figure 4): (1) electrostatic interaction between the cationic residues and anionic lipids lead to an increased local concentration and enhanced orientation of the peptide at the interface of the membrane promoting initial amyloid nucleation.[28, 29] Consequently, membrane integrity is disturbed by fibril growth resulting in thinning and fragmentation[30]; (2) the toxic oligomer hypothesis predicts structural transition of hIAPP monomers bound to the membrane from a disordered structured into a partially α-helical conformation followed by oligomerization.[31] The hydrophobic on-pathway oligomers permeate the membrane causing membrane disorder by a detergent-like mechanism[32]; (3) in the pore theory, hIAPP forms non-selective ion channel-like pores resulting in insufficient homeostasis.[33] Therefore, membrane-mediated amyloid formation takes place intracellularly inducing β-cell death. The final deposition of amyloid plaques in the extracellular space impairs islet structure and function.[16]

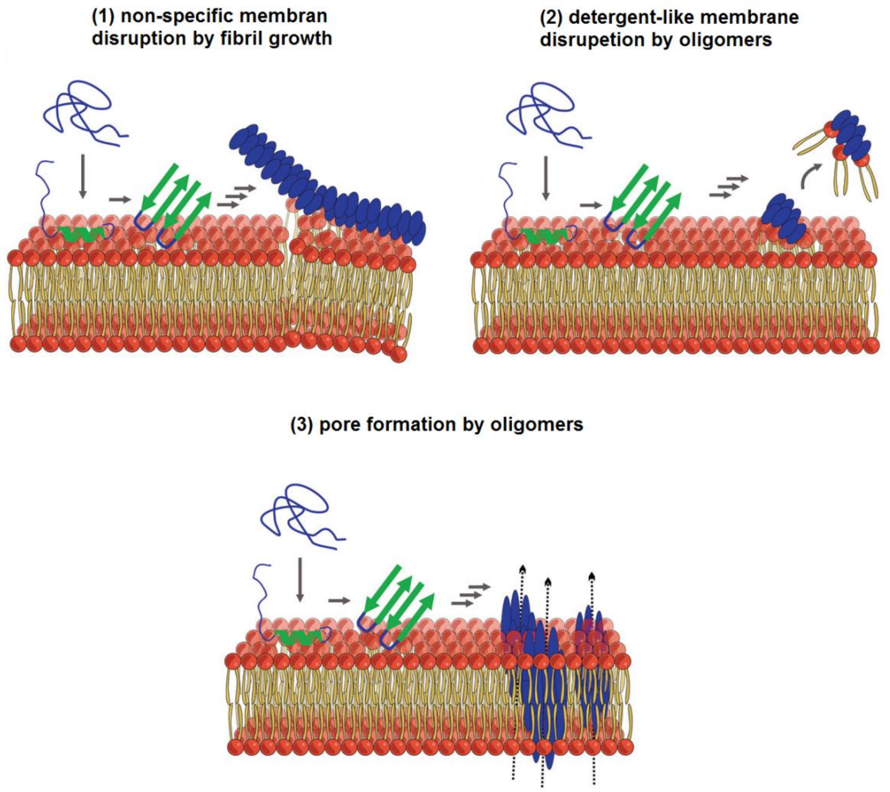

Figure 5. Mechanisms proposed for hIAPP-mediated membrane disruption. Figute Taken from Owen *et al.*[16]

2.1.3 STRUCTURAL CHARACTERIZATION OF hIAPP

hIAPP amyloid fibrils adopt a cross-β architecture commonly observed for amyloidogenic peptides. In hIAPP protofibrils the seven first residues may not be involved in the β-structure core due to conformational constraints imposed by the disulfide bridge.[19] The atomic level model proposed for hIAPP fibrils is derived from NMR studies. In this model, β-strands are in parallel, in register arrangement. The protofibrils are composed by two columns of hIAPP monomers adopting a U-shaped structure. In fibrils, each monomer contains of two β-strands connected by a loop. They encompass the residues 8-17 and 28-37.[34] The β-strands are involved in intermolecular hydrogen bonds with neighboring polypeptide chains within the same column but not in intramolecular hydrogen bonds.[19] Additionally, the residues Arg11, Ala13, and Phe15 are solvent-exposed.[19] A second atomic level model was proposed based on X-ray crystallographic studies of fragments derived from hIAPP. This model is similar to the one developed from NMR data expect for differences in details of the atomic packing in the monomers, differences in the bimolecular interface between two hIAPP monomers, and differences in the register at the bimolecular interface.[19, 35]

In both presented models, the 20–29 segment forms the partially ordered loop region that connects the two strands, albeit 2D IR experiments have shown that these the residues 23–27 form parallel β-sheet structures in oligomeric intermediates. Further, IM-MS coupled to IR spectroscopy revealed that extended NFGAIL oligomers exhibit a significant extent of β-sheet conformations.[36] Based on the results obtained from two dimensional IR experiments (2D-IR), Serrano *et al.* propose that the free energy necessary for disruption of the oligomeric β-sheet structure and rearrangement into the structure of the fibril slows aggregation, lengthening the lag phase, and stabilizing the population of the oligomers.[37, 38]

Like other peptides, hIAPP follows an aggregation pathway comprising a lag, a growth and a saturation phase. Recent time-resolved biophysical and biological studies performed by Abedini *et al.* have proved the time-dependency of hIAPP toxicity to β-cells.[4] In their work, aliquots of a buffered and incubated hIAPP solution were added at various time points over the course of the aggregation pathway and applied to β-cells. Real-time biophysical characterization by ThT assays TEM concurrent with toxicity assessment in β-cells revealed that a pre-amyloid lag-phase intermediates upregulate oxidative stress, inflammation and apoptosis.[4] Further analysis by sodium dodecyl sulfate polyacrylamide gel electrophoresis (SDS-PAGE) of aliquots of toxic lag phase intermediates showed a distribution of oligomers ranging from monomers to hexamers. The same distribution of hIAPP oligomers were also observed by IM-MS studies within two minutes after initiating amyloid formation.[39] These results reinforce previous evidences that transient soluble oligomers rather than mature fibrils are the cytotoxic species. However, similar distribution of oligomers of non-toxic rIAPP and other hIAPP-variants are also observed suggesting that cellular toxicity rely rather on conformational properties of the transient oligomers than on their size.[4. Various groups have been intensively working on the characterization of these toxic intermediate oligomers that populate the lag phase and on disentangling the mechanism for amyloid formation.

An important factor to be considered is the environment where the aggregation takes place and transfer physiological conditions into *in vitro* experiments. Oxidative environments have been shown to affect the kinetics of hIAPP aggregation. In cells, the redox state of the ER is shifted towards reducing conditions in T2D resulting in folding deficiencies.[40] ThT assays supported by NMR experiments showed that $hIAPP^{red}$ aggregates faster than $hIAPP^{ox}$. EM and solution-state heteronuclear single quantum coherence NMR (HSQC-NMR) experiments of hIAPP aggregates at different redox states revealed different morphologies of the fibrils formed by $hIAPP^{red}$ and $hIAPP^{ox}$. These results indicate that aggregation shifts the equilibrium to the reduced state of the peptide. Therefore, external factors having impact on the ER redox state could trigger hIAPP aggregation in cells.[41]

CD spectroscopy in combination with solution-state NMR experiments on reduced and oxidized forms of hIAPP monomers revealed strong helical propensity for the N-terminal half of the peptide (residues 8–17) and a random coil conformation for the C-terminal half of the peptide.[41, 42] Other studies also showed that the same residues adopt a fully helical structure when bound to membrane surfaces or micelles.[42, 43] However, in comparison to $hIAPP^{ox}$, $hIAPP^{red}$ showed a smaller helical propensity. These results suggest that the disulfide bridge at the N-terminus stabilizes the helical conformation and consequently protects the peptide from aggregation.[41] Miranker and coworkers[31] also detected a decrease in the helical content throughout the same region when the disulfide bond is reduced. However, the lower extent of helices was correlated to a decrease in fibril formation.[31] The structure of mature fibrils is known from solid-state NMR experiments. In the strand-turn-strand structure adopted by hIAPP monomers in amyloid fibrils, the N- and C-terminal strands involve the residues 8–17 and residues 28–37, respectively. Based on the structure of mature fibrils, Miranker proposed a model for oligomerization based on parallel helix-helix interactions.[31] The helical conformations are stabilized by negatively charged membranes. Their association in parallel leads to a high local concentration of amyloidogenic regions in the required arrangement for β-sheet formation, thus acting as catalyst for fibrillation.[31]

Other hypothesis for hIAPP aggregation through β-sheet conformers without involving α-helical intermediates has also been suggested. Using a combination of IM-MS and MD simulations, Dupius *et al.* proposed β-hairpin as the structures of the early intermediates preceding hIAPP aggregation.[8] IM-MS results identified two distinct conformers for the triply and quadruply protonated hIAPP monomers. The compact +4 ion has a helix-coil type secondary structure whereas a β-hairpin was assigned to the extended +4 monomer. To the dominant +3 hIAPP conformer a compact β-sheet-rich structure was assigned.[8] The hIAPP dimer was also analyzed by IM-MS.[44] The experimental collision cross section (CCS) for the dominant structure and the respective estimated CCS fit well, assuming no change in the monomer structure with dimer formation. This suggests that the dominant dimeric conformer assembled from the β-hairpins.[44] The results published by the Bower's group are consistent with previous suggestions that hIAPP populates two conformers, where one is more amyloidogenic than the other.[45] Moreover, identification of a monomeric β-hairpin gives experimental evidence for the "early conformation transition" mechanism, by which nucleation starts from ordered structures and conformational transition from unordered to β-structure occur before nucleation.[8, 46]

As controversial as the experimental evidences published so far, theoretical work has not yet achieved a consensus on the structure of intermediate oligomers. REMD simulations performed by Reddy *et al.* revealed three stable conformations for the peptide in solution: an α-helical conformation comprising the residues 9–17 with β-sheet domain between residues 24–28 and 31–35; a β-hairpin with a turn at residues between 20 and 23; and a random coil conformation. α-helical and β-hairpin structures in solution are stabilized by intrapeptide hydrogen bonds and are enthalpically preferred over random coils which are stabilized by peptide-water hydrogen bonds.[47] Moreover, long molecular simulations showed that the α-helical conformation can spontaneously convert into the β-hairpin. The stability of the α-helical structure is believed to be affected by interaction of the residues 24–28 near the C-terminus with the α-helical segment, leading to misfolding into a β-hairpin. In the rat IAPP, the presence of proline residues near the C-terminus prevents destabilizing interactions, leading to a more stable native state.[47]

Whereas previous MD simulations support the early conformation transition mechanism via the β-hairpin early oligomers, recent large-scale discrete MD revealed accumulation of helical intermediate states before aggregation in agreement with results showed by *in* *vitro* studies.[35, 41, 42] MD simulations showed that formation of hIAPP aggregates from monomers to hexamers is a dynamic process involving inter-exchanges between different species.[48] These intermediates are on average composed mainly of helical conformations. Similarly, the 8–20 fragment assembled into helix-rich oligomers ranging from dimers to decamers by shielding the hydrophobic surface of the helices.[49] In both simulations, the content of β-sheet conformations increased wit oligomer size accompanied from a decrease in coil structures while the overall helical content remained constant. The highest content of β-sheet structures within the full-length hIAPP was found for pentamers and hexamers and β-sheet was the dominant secondary structure observed for hIAPP 8–20 oligomers higher than decamers. Analysis of secondary structure propensity per residue indicates high propensities to form α-helices by the residues 8–15 in both monomers and higher order oligomers. Weakly populated β-sheet structures formed by residues around 16–20 and 24–28 and the relatively high propensity of the residues 21–23 to adopt turn conformations are consistent with a β-hairpin structure in this region.[48]

These simulations support an aggregation mechanism by which nucleation initiates with formation of helical oligomers assembled direct from isolated helical monomers. Conformation transitions into β-sheets occur inside the oligomers and are more significant for pentamers and hexamers. The last step proposed for this oligomerization process is the conversion of the β-sheet-rich oligomers to β-barrel structures, i.e. β-rich oligomers in the shape of a barrel, which were indicated to be the toxic.[48] These toxic β-barrel oligomers have been recently discovered in the aggregation of a fragment from the protein αB-crystalline.[50] Experimental characterization and computational modeling also indicated formation of β-barrel by other peptides.[51] Further MD simulations on short peptides derived from hIAPP and other peptides suggested that β-barrel oligomers are the common intermediates for amyloids assembling into cross-β like aggregates.[52] These structures have also been proposed as the toxic oligomer species since their capability of interfacing across the membrane bilayer is compatible with the “amyloid-pore” hypothesis of amyloid toxicity.[53]

2.1.4 INTERACTION OF AMYLOIDS WITH TRANSITION METALS

The morphology of hIAPP fibrils and the kinetics of fibrillization highly depend on the environmental conditions.[54] While the hIAPP aggregates are readily observed *in vitro* at lower concentrations, the peptide is accumulated at millimolar concentration *in vivo*. As there is no difference in the amino acid sequence within the peptide in diabetic and nondiabetic individuals, external factors in the cellular environment might act as triggers for aggregation by stabilizing the protein at high concentrations.[55] The role of metals in hIAPP aggregation has been increasingly explored by several groups due to its potential biomedical importance.[11] In particular, zinc and copper ions have been widely associated with T2D.

The highest concentration of zinc in the body is found in the β-cells, where it is stored with hIAPP and insulin. The high content of zinc in these cells can be explained with the packaging of crystalline insulin, which needs two zinc ions per insulin hexamer.[56] Moreover, the relationship between zinc deficiency in the granules and the occurrence of T2D have implicated that zinc ions prevent peptide aggregation as zinc supplements have shown to decrease β-cell death.[57] In contrast, the inductive effect of zinc on hIAPP aggregation has also been reported.[57]

Despite of these numerous evidences for the importance of these metal ions in T2D, the exact structure of the species formed upon metal-binding as well as the mode of coordination remains elusive. Two Zn(II) coordination models have been proposed for hIAPP monomers, both involving the His18 residue. At physiological pH, zinc is coordinated to the N-terminal amine together with the imidazole nitrogen of His18 and two molecules of water (Fig. 6, left).[58, 59] Besides the His18, an oxygen atom of the contiguous Ser19 is likely to coordinate to zinc (Fig.6, right).[60] Furthermore, ESI-MS data has identified a small population of hIAPP monomer bound to two zinc atoms at millimolar concentrations of $ZnCl_2$, suggesting that hIAPP possess a second Zn(II) binding site with weak-affinity.[57] This monomer bound to two zinc atoms is believed to be the key for the proposed bimodal effect on hIAPP fibrillogenesis.[60]

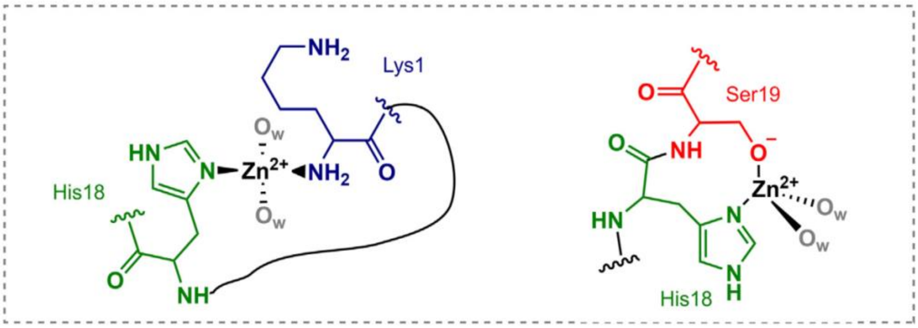

Figure 6. Two Zn(II) coordination models for hIAPP.[58]

According to Ramamoorthy's group, the effect of zinc ions on hIAPP aggregation depends on their concentration and different stages of the aggregation process.[11] At low concentrations, zinc has an inhibitory effect on fibril formation by increasing the lag time. This hypothesis suggests that zinc ions stabilize the prefibrillar aggregates, thus preventing equilibrium towards mature fibrils.[61] More specifically, zinc forms very stable off-pathway hexameric species with hIAPP while inhibiting the formation of the dimer. The presence of Zn(II)-bound hexamers at low zinc concentrations were confirmed by MD simulations.[62] The electrostatic repulsion of adjacent β-sheets in presence of zinc is also proposed to modulate inhibition.[60] At higher concentrations zinc ions show an opposite effect where they promote the formation of aggregates.[57, 60] In contrast, AFM studies have reported a reverse behavior, i.e. inhibition of aggregation at higher zinc concentrations.[56] These contrasts rely on the hIAPP concentration, which has to be sufficiently high to lead formation of high-molecular weight oligomers.[62]

It is important to keep in mind that amyloidogenic peptides exist in a highly dynamic equilibrium between transient species and each oligomer may have different affinities for metal ions. IM-MS has been used in order to investigate which transient species show higher affinity to metal ions and to estimate the conformation of the metal-associated oligomers. Bowers *et al.* have identified two conformers for the Zn(II)-hIAPP monomers with charge state +4. The abundance of the extended hIAPP monomer in the presence of zinc was higher in comparison to metal-free hIAPP. Based on these results, Bowers *et al.* suggest that higher zinc concentrations stabilize the extended β-hairpin hIAPP conformer, which then becomes less amyloidogenic.[56]

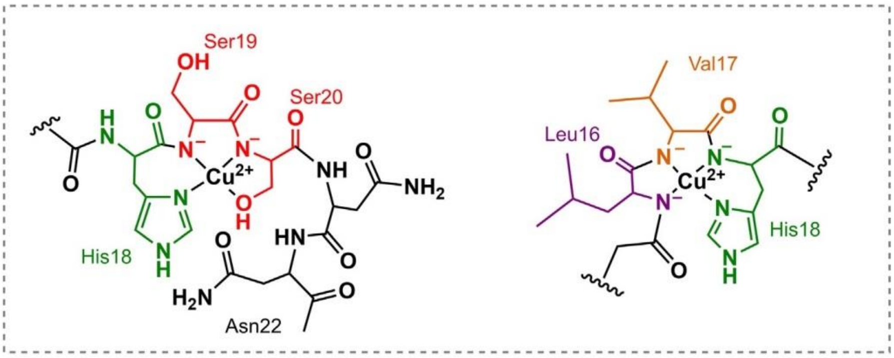

Figure 7. Two Cu(II) coordination models for hIAPP.[58]

The elevated copper levels in serum observed in T2D also suggest a direct relationship between copper ions and hIAPP aggregation. The role of copper-complexation on hIAPP aggregation is equally discussed in recent literature. Several studies have shown an increase in production and accumulation of toxic hydrogen peroxide in the presence of Cu(II) *in vitro.*[63] However, generation of specific oligomeric species, rather than production of hydrogen peroxide has been proposed to be crucial for cytotoxicity of hIAPP in the presence of copper.[64]

Similar to Zn(II), a consensus on the coordination mode of Cu(II) to hIAPP monomers has not yet been reached. Riba *et al*. proposed that Ala25 and a second residue near the C-terminus are the possible binding sites for copper ions in full-length hIAPP.[65] However, a variety of experimental and theoretical approaches support that the residues 18–25 are responsible for metal coordination within hIAPP.[57, 66-68] In the proposed models, the anchoring role played by His18 is undeniable.[58] The two amide groups adjacent to the His establish the coordination towards the C- or N-terminal region.[58] Based on spectroscopy and computational studies, Quintanar's group has proposed an equatorial binding motif towards the C-terminus at physiological pH, where the copper ion is complexed to three nitrogen atoms and one oxygen atom (3N1O).[66] In this model, copper is coordinated with the imidazole nitrogen of His18 and two deprotonated nitrogen amides of the Ser19 and Ser20 residues. The Ser20, furthermore, coordinates to the copper with an oxygen atom either from the alcohol side chain or from the carbonyl group.[66] In the model proposed by Magrí *et al*., apart from His18, three deprotonated amides are involved, forcing the coordination toward the N-terminus.[69]

While the role of zinc on amylin aggregation is more complex and still a matter of debate, the inhibition of fibril formation by copper is more widely accepted. It was suggested that the presence of Cu(II) increases the barrier for oligomerization, thereby extending the lag phase and slowing down the rate of aggregation.[11] Using mass spectrometry, Li *et al*. showed that Cu(II) inhibits fibril formation by preventing formation of hIAPP dimers.[70] Further evidence is provided by CD spectroscopy and TEM experiments. Lee and coworkers have shown that the secondary structure of hIAPP in the presence of copper ions is mainly random coil. They also reported formation of small and globular non-fibrillar Cu(II)-hIAPP aggregates with distinct morphologies from those formed by Zn(II)-hIAPP and metal-free hIAPP.

Lee *et al.* also performed ion mobility studies on zinc-bound hIAPP and compared the results to copper-bound hIAPP. Based on IM-MS experiments and MD simulations, they reported the higher affinity of Cu(II) for the compact conformation. According to Lee *et al.*, these differences rely on local changes around His18.[67] The Cu(II)-hIAPP in solution has a maximum charge of +3. Even in the gas phase, the Cu(II)-coordinated region remains as +1 charge state as in metal-free hIAPP. In the case of Zn(II)-hIAPP, formation of the +4 ion involves protonation of two possible sites. Due to the distribution of positive charges, the local structure around His18 is rearranged to accommodate the zinc ion. The differences in the coordination chemistry of zinc and copper ions toward amylin have been pointed as one of the reasons leading to distinct aggregation pathways of metal-coordinated hIAPP.[67]

2.2 TECHNIQUES AND METHODS

2.2.1 ION MOBILITY-MASS SPECTROMETRY

Gas-phase techniques offer a good alternative to condensed-phase analytical techniques to provide structural information on isolated species derived from a complex ensemble. Especially IM-MS has been employed in the analysis and characterization of isolated molecules in the presence of other species. As a separation technique, IM-MS has been extensively applied in structural biology. In the field of amyloid research, species with the same *m/z*-ratio can derive from different homo-oligomers. With ion-mobility separation prior to *m/z*-selection, individual conformers of an assembly can be investigated individually.

The basic principle of ion mobility spectrometry (IMS) is based on the characteristic mobility of ions, or the ability of ions to move through a certain medium, which depends on their shape, charge and mass. Ions are guided through a cell that is filled with an inert neutral buffer gas such as helium or nitrogen, under the influence of a weak electric field. During their trajectory, the ions suffer more or less number of collisions with gas molecules according to their size, shape and charge. Compact ions are more mobile and therefore pass through the cell faster than more extended ions. Multiply charged ions have a higher mobility than singly charged ions of same *m/z*. In this way, ions of the same *m/z*-ratio and different conformations can be separated within the mobility cell.

Thus, while MS determines the *m/z*-ratio of an analyte ion, IMS separates them based on their size and shape. The recorded drift time can be converted into a collision cross section (CCS), which is an intrinsic property depending on the ion's overall structure and also independent of the utilized instrument parameters and conditions.

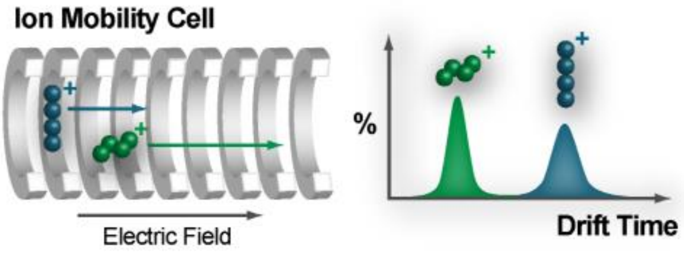

Figure 8. Scheme of an ion mobility separation. In this figure, separation based on the shape of the molecules is presented.

2.2.2 COLLISION CROSS-SECTION CALCULATION

The collision cross section (CCS) is an intrinsic property of a molecule and is related to its shape. Under controlled conditions, the CCS value is independent of instrument parameters, enabling the creation of databases. In order to experimentally determine the CCS, all the instrument parameters and settings must be accurately known. The drift velocity v of the ion is the product of ion mobility constant K and the electric field E,

$$v = K * E = K\frac{V}{L} \tag{1}$$

The velocity is determined by measuring the time the ions require to traverse the drift cell, t_D and it is proportional to the inverse mobility ($1/K$) as well as the inverse of the electric field ($1/E$). Therefore, the mobility of an ion can be determined from the slope of a plot with t_D versus $1/V_d$, where V_d corresponds to the drift voltage. The intercept, t_0, corresponds to the time the ions require from the end of the drift region to the detector (Figure 9)

$$t_D = \frac{L}{KE} + t_0 = \frac{L^2}{KV_d} + t_0 \tag{2}$$

In low-field conditions, the velocity of the ion is directly proportional to the electric field by the proportionality ion mobility constant K and is related to the ion's collision cross-section (Ω) by the Mason-Schamp-equation[9] (Equation 3.3)

$$\Omega = \frac{3ze}{16N}\frac{1}{K_0}\sqrt{\frac{2\pi}{\mu k_B T}} \tag{3}$$

where $z^* e$ is the ionic charge, N the drift gas number density, μ the reduced mass of the ion and the drift gas, k_B the Boltzmann constant, and K_0 the reduced ion mobility (Equation 2).[9] When coupled to mass spectrometry, the mass and charge are known and the CCS can be calculated.

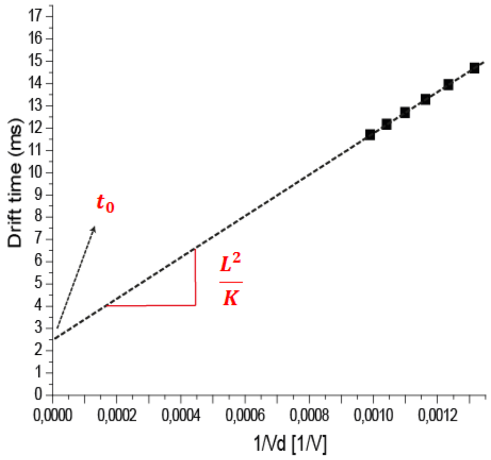

Figure 9. Determination of the mobility of an ion. The measured drift times are plotted against the invert of the drift voltages. The intercept, t_0 gives the dead time and the slope the mobility K.

2.2.3 INFRARED SPECTROSCOPY

An IR spectrum results from transitions between quantized vibrational states when a molecule absorbs resonant IR light. Nonlinear molecules with N atoms have 3N degrees of freedom. Three of them represent translational motion and three represent rotational motion about the x, y and z axes. The remaining 3N-6 degrees of freedom refer to the vibrational modes. Because rotation of a linear molecule about its axis does not lead to displacement of the atoms, linear molecules lose one of the rotational degrees of freedom and have an additional vibrational mode. Thus, the number of vibrational modes of a linear molecule is 3N-5.[71] For each vibrational mode all atoms vibrate at a certain frequency, ν_i. Atoms vibrating with harmonic motion (i.e. obeying Hooke's law) have an harmonic potential well as depicted by the dashed lines in Figure 10.

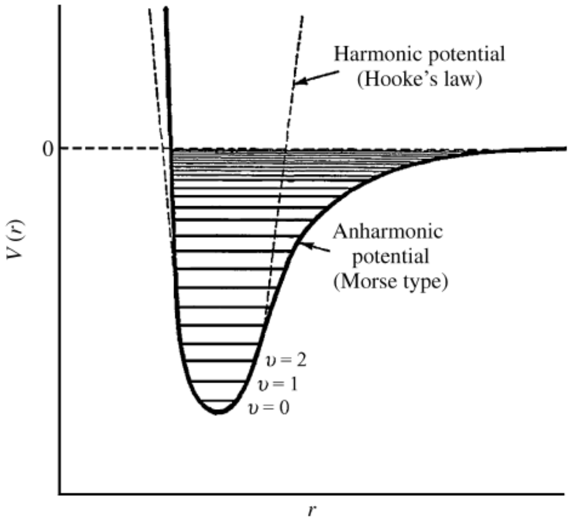

Figure 10. Harmonic (dashed line) and Morse-potential (solid line) of a diatomic molecul as a function of the atomic displacement during vibration.[71]

The vibrational energy states for modes in which atoms have a harmonic motion can be described by the equation

$$V_{i\upsilon} = h\nu_i\left(\upsilon_i + \frac{1}{2}\right) \tag{4}$$

where h is Planck's constant, υ_i the vibrational quantum number of the i-th mode and ν_i the vibrational frequency given in units of wavenumber (cm^{-1}). Vibrational transitions occur only if the dipole moment of the molecule, μ, changes during the vibration, i.e., where Q_i are normal coordinates used to describe the vibrational motion of the atoms. Depending on the element of symmetry that a molecule has, some vibrational modes may be degenerate. As a consequence, more than one mode has a given vibrational frequency whereas others may be completely forbidden and the number of fundamental absorption bands is usually less then 3N-6.[71]

However, molecular vibrations deviate are anharmonic and the variation of the potential energy as a function of the displacement of atoms from their equilibrium positions are described by an anharmonic Morse-potential (represented by the solid line in Figure 10) and is given by the expression

$$V_{i\upsilon} = h\nu_i\left(\upsilon_i + \frac{1}{2}\right) + h\nu_i x_i\left(\upsilon_i + \frac{1}{2}\right)^2 \tag{5}$$

where x_i is the *anharmonicity constant*. In the harmonic picture no transitions where $\Delta\upsilon_i \geq \pm1$ would be allowed. The anharmonicity relaxes this selection rule, and therefore, weak overtone and combination bands can be observed in the mid-infrared spectrum along with fundamental bands.

Many vibrational modes have a frequency that is characteristic for certain functional groups and is barely affected by the environment within the molecule. Other bands occur at frequencies that vary from a molecule to another containing a particular functional group. These bands are known as *fingerprint bands* and their vibrational frequencies are influenced by intra- and intermolecular effects.[72]

In protein analysis, five typical bands can be observed in an IR spectrum due to absorption of protein backbone. These bands derive from the normal modes of the amide group. Amide A and B bands occur at wavenumbers above 3000 cm^{-1} and correspond to the N-H stretching vibrations. The amide I band between 1600 and 1700 cm^{-1} has the strongest absorption of IR light and is caused by C=O stretching vibration with minor contributions with the out-of-phase C-N stretch and N-H bending. The amide II band at 1500-1600 cm^{-1} arises mainly from the out-of-phase combination of the NH in plane bend with the CN stretching vibration. Lastly, the amide III band, found in the 100-1400 cm^{-1} region, is derived from the in-phase combination of NH bending and CN stretching along with deformation vibrations of CH and NH. The amide I band is highly sensitive to the secondary structure of proteins and peptides and is used to obtain structural information from the spectral features.[72]

2.2.4 ATTENUATED TOTAL REFLECTION–FOURIER TRANSFORM INFRA-RED SPECTROSCOPY

Infrared spectroscopy consists is one of the classical methods of structure determination of small molecules and has been shown to be a powerful tool for gaining insight into protein structure.[72] The two most traditional methods are transmission and attenuated total reflection (ATR) spectroscopy. In transmission measurements, IR light is passed through a cuvette containing the sample before it reaches the detector. The sample absorbs the light according to the Lambert-Beer law[71]:

$$I(v) = I_0 e^{-\sigma(v)ln} \qquad (6)$$

In the ATR technique the sample is placed in contact with an infrared transparent surface with a high refractive index called internal reflection element (IRE). IR light is directed at the interface between the sample and the IRE. When the angle of incidence is greater than the critical angle, the incident IR light is totally reflected.[72, 73] Despite of the sample being confined to the IRE, the electromagnetic field of a photon is oriented perpendicularly to its path. This electromagnetic field is also referred as evanescent wave. At the point of the contact between the sample and the IRE, the field extends from the interface into the sample and decays exponentially with the distance from the surface. The strength of the electrical field, E, can be written as a function of the distance z from the surface

$$E = E_0 e^{-\gamma z} \tag{7}$$

where E_0 is the strength of the electrical field at the surface. The distance from the surface where the evanescent wave still interacts with the sample can be approximated as the distance from the surface at which the intensity of E has attenuated to $1/e$ of its initial intensity E_0. This distance is called *depth of penetration*, d_p, corresponds to $1/\gamma$ from the equation 3.5. and it is depends directly on the wavelength of the incident radiation, λ, the angle of incidence θ and the relative refractive index of the sample and IRE (n_2/n_1).[72-74]

$$d_p = \frac{\lambda}{2\pi n_1\left(\sin^2\theta - \left(\frac{n_2}{n_1}\right)^2\right)^{\frac{1}{2}}} \tag{8}$$

Modern spectrometers used in routine measurements are usually Fourier transform infrared (FTIR) spectrometers. The heart of any FTIR spectrometer is an interferometer.[72. Figure 11 depicts the commonly used Michelson interferometer. It consists of a fixed and a movable mirror and a beam splitter. Light emitted from the light source reaches the beam splitter. Half of the emitted light is reflected towards the fixed mirror and then reflected back towards the beam splitter where approximately 50% traverses to reach the detector. The other half of the emitted light passes the beam splitter and reaches the movable mirror. There it is reflected back to the beam splitter where 50% of the light is reflected towards the detector. The two beam combines, leading to constructive or destructive interference depending on their difference in the travelled path. The light intensity as a function of the position of the movable mirror is measured. The resulting interferogram corresponds to a Fourier transform of the spectrum. The computer performs a second Fourier transform converting the measured data back into a spectrum.[72]

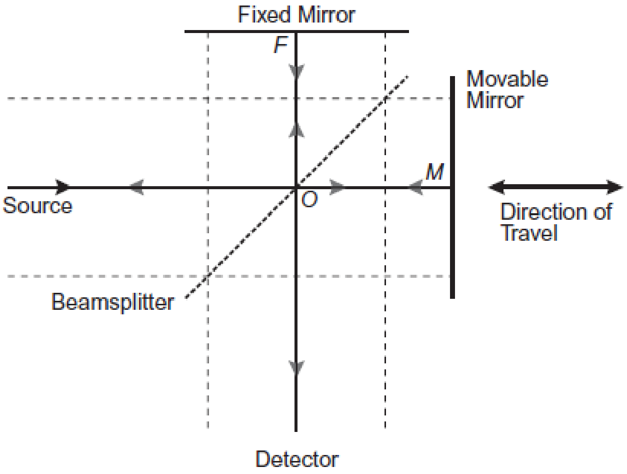

Figure 11. Sketch of a Michelson Interferometer.[73]

2.2.5 ACTION SPECTROSCOPY

When performing spectroscopy in the gas-phase, samples are optically diluted and direct absorption IR spectroscopy techniques cannot be applied in this case. In Eq. 3.6, the product of number density and optical path length is typically so small that the difference between $I(\nu)$ and I_0 is not measurable. Alternatively, *action spectroscopy* methods monitor the effect of IR radiation on molecules. Such effects include changes in ionization yield, quantum state, fluorescence yield, fragmentation or electron detachment.[75] The number of molecules affected by the IR radiation can be expressed by:

$$N(\nu) = N_0 e^{-\sigma(\nu)\Phi(\nu)} \tag{9}$$

where $\Phi(\nu)$is the photon fluence. However, large systems such as covalently bound molecules or noncovalent and very stable complexes have a very high threshold to dissociation which is much higher than the energy of a single IR photon. Therefore, absorption of multiple photons by a single ion is needed to induce dissociation. This experimental method is named infrared multiple photon dissociation spectroscopy (IRMPD) and in this approach a high flux of photons is required, which is achieved with the use of high intense laser sources such as free-electron lasers (FEL).

2.2.6 INFRARED MULTIPLE PHOTON DISSOCIATION

IRMPD is an activation method used in gas-phase spectroscopy based on the sequential absorption of multiple photons. When the radiation frequency is resonant with the vibrational transitions of a molecule, photons are absorbed leading to an increase in its internal energy. However, in the here considered process, the multiple photon excitation is not a process where the absorption of photons from a monochromatic laser source occurs in one vibrational ladder in a stepwise manner (υ=0 → υ=1…). This lies on the fact that molecular vibrational potentials are inherently anharmonic. In the anharmonic picture of the vibrational potential, the spacing between adjacent vibrational levels decreases as the vibrational quantum number increases. This effect is commonly referred as *anharmonicity bottleneck.*[75, 76]

The anharmonicity introduces terms in the potential that lead to coupling between normal modes. Due to this coupling, energy flux from a vibrational mode into another is possible, so that an excited vibrational level can be deactivated by intramolecular vibrational redistribution (IVR).[76]Therefore, another photon can be absorbed as soon as the fundamental vibrational level is deactivated. The efficiency of the multiple photon excitation (MPE) depends largely on the rate of the IVR process, which for polyatomic molecules at room temperatures, occurs in sub-ns timescale. As a consequence of the sequential multiple photon absorption and subsequent depletion of the excited vibrational mode, the vibrational excitation is randomized over the entire molecule leading to an increase in its internal energy. When the threshold is achieved, usually the weakest bond breaks.[75, 76] The Figure 12 depicts the IRMPD fragment spectra of the polyalanine peptide used in this thesis. The absorption of resonant light induces fragmentation of the parent ion generating b and y-type fragments. IR spectrum is then obtained from the intensities of the parent and fragment ions.

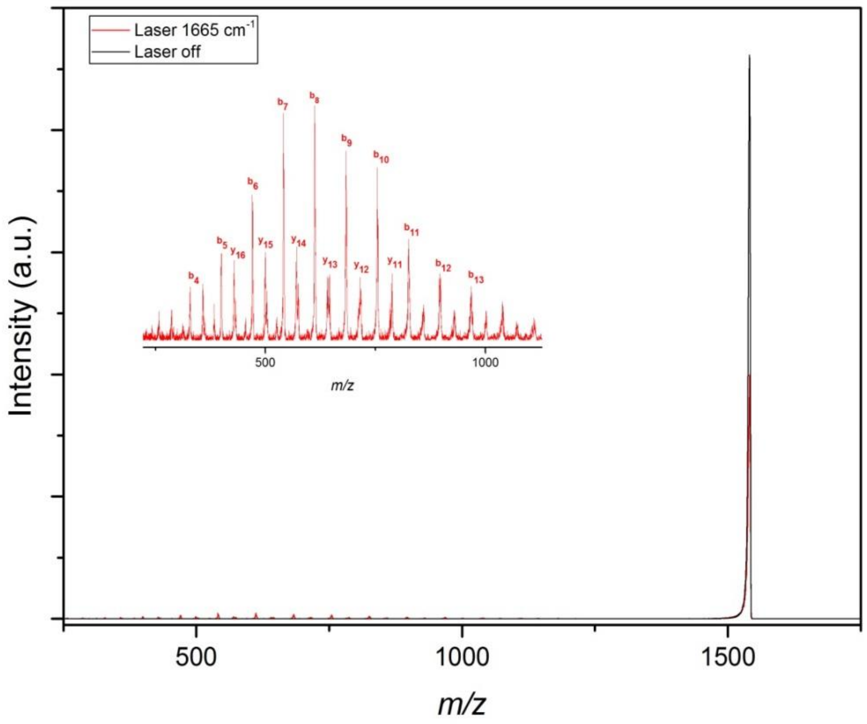

Figure 12. Photofragmentation mass spectra of polyalanine.

Free-Electron Laser (FEL)

The experimental methods in the gas-phase described in the previous sections rely on the use of tunable IR laser sources capable of providing a high photon flux. This is achieved by the use free-electron lasers (FEL).

In the FHI-FEL, electrons provided by an electron gun are accelerated close to the speed of light by two consecutive linear accelerators (linac). The relativistic electrons are then injected into the resonator, which consist in two highly-reflective mirrors positioned at each end of an undulator. The undulator is a periodic magnetic device that forces electrons into an oscillatory motion. There, the produced radiation is captured in a laser cavity, where the circulating light pulses interact with further electron bunches, thus increasing the intensity of the radiation by 10^6–10^8 magnitudes of order. For coherent radiation to be produced, the wavelength has to correspond to an integer of the pathlength difference over one undulator period. Since this gap is tunable, radiation with different wavelengths can be emitted. A schematic depiction of the FHI-FEL used in here presented experiments is given in Figure 13. This FEL facility provides intense and tunable light in the regime of 3 to 50 μM.

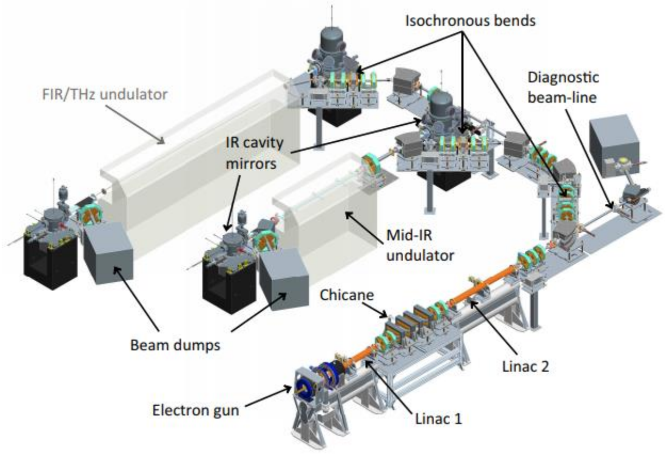

Figure 13. Schematic setup of the Fritz Haber Institut free-electron laser (FHI-FEL). The FIR/THz undulator will be built in the future.

3. EXPERIMENTAL SECTION

3.1 Sample Preparation

The peptides VEALYL, human and rat islet polypeptide (IAPP), all with C-terminal amide were purchased from GenScript Biotech Corporation. The peptides Protegrin-1 (PG-1) and a fragment of the prion peptide ($PrP_{106–126}$) were purchased from Anaspec. Polyalanine and the peptide tendamistat were provided by the group. Peptide samples were used without further purification. hIAPP, rIAPP, $PrP_{106–126}$ and PG-1 were dissolved in 100% 1,1,1,3,3,3-hexafluoro-2-isopropanol (HFIP) to a concentration of 500 μM and aliquots of 20 μL were taken and dried overnight. The peptides were freshly dissolved at different concentrations prior each experiment. All other standard chemicals and solvents were purchased from Sigma Aldrich.

Model Peptides

Polyalanine was dissolved in H_2O with formic acid (FA) (50%) to a concentration of 500 μM. For ATR-FTIR experiments, the sample was dissolved in ^2H_2O to a concentration of 5 mg mL^{-1}.

Tendamistat was dissolved in NH_4AcO (5mM, pH 7) with 0,1% FA to a final concentration of 100 μM. To perform IRMPD spectroscopy of tendamistat-crown ether adducts, tendamistat was dissolved in H_2O:MeOH (1:1, v/v) to a final concentration of 100 μM with 500 μM of 18-crown-6. For ATR-FTIR experiments, the sample was dissolved in ^2H_2O to a concentration of 7,5 mg mL^{-1}.

PG-1 were resuspended for IM-MS experiments in H_2O:MeOH (1:1, v/v) to a final concentration of 50 μM. Reduction of the disulfide bond was performed by adding 2-mercaptoethanol (10%, v/v) to the sample. For IRMPD spectroscopy of PG-1-crown ether adducts, a stock solution of dibenzo-30-crown-10 (db30c10) was prepared in H_2O:ACN (1:1, v/v) and added to the fresh peptide solution of 50 μM with same solvent conditions to yield a DB30C10/PG-1 solution of 10:1. For IRMPD experiments of PG-1 oligomers, the peptide was diluted to 200 μM in H_2O:MeOH (1:1, v/v).

Human Islet Amyloid Polypeptide

For IM-MS and IRMPD experiments, dry hIAPP and rIAPP were resuspended in NH4AcO (5 mM, pH 7):MeOH (1:1, v/v) to a final concentration of 50 μM. For solution-phase IR measurements, samples were redisolved in ^2H_2O to a final concentration of 7.5 mg mL^{-1}.

hIAPP-metal adducts

A stock solution of 10 mM of zinc chloride ($ZnCl_2$) and copper chloride ($CuCl_2$) was prepared. Prior to the measurements, the peptides were diluted in H_2O to yield a concentration of 50 μM for the respective peptide and and 500 μM for the respective metal salt.

Heterodimers

Dry $PrP_{106–126}$ was dissolved in H_2O:MeOH (1:1, v/v) to a final concentration of 50 μM and subsequently added to the hIAPP and rIAPP solutions with same solvents to yield a 25 μM: 25 μM solution.

A stock solution of 500 μM VEALYL was prepared in H2O and added to a hIAPP solution in NH_4AcO (10 mM) to generate a 1:1 VEALYL/hIAPP ratio.

3.2 ATR-FTIR

For measuring the solution-phase IR spectroscopy, the BioATR- FTIR instrument from Bruker Optik (Ettlingen, Germany) was used. The spectrometer is equipped with a multi-reflection ATR cell and a photovoltaic LN-MCT detector. The circular sampling area consists of an ATR-crystal made of silicon and has a radius of 2mm. The experimental parameters are given in Table 1.

Table 1. Typical parameters for ATR-FTIR.

Experimental Settings	
Spectrometer Aperture	1 mm
Resolution	2 cm^{-1}
Number of Background Scans	100 scans
Number of Scans:	100 scans
Source	MIR
Detector	LN-MCT
Scanner Velocity	40 Hz

3.3 DT-IM-IRMPD

In order to obtain information on the secondary structure of oligomeric species, ion- mobility spectrometry, mass spectrometry and infrared spectroscopy are combined in a single experimental set-up. The drift tube-ion mobility (DT-IM) experiment (see Figure 14) was designed and built at the department of Molecular Physics at the Fritz Haber Institute of the Max Planck Society in Berlin.

In the experimental set-up, the sample is transferred into the gas phase by nano-electrospray ionization source (nESI) using borosilicate capillaries coated with Pt/Pd. This is an appropriate technique for the ionization in biomolecules because it allows direct transfer of fragile macromolecules into the gas phase with minimal impact on the native, solution-phase structure.[8]The generated ions are subsequently collected in the entrance funnel that is operated with radio frequency (RF). In the entrance funnel, ions are radially collimated, trapped for a time interval on the millisecond scale and then injected into the mobility cell (drift tube), where ion mobility separation takes place. Ions travel through the mobility cell under the influence of a weak, homogeneous electric field. A second funnel (exit funnel) is positioned at the exit of the mobility cell to focus the diffusionally scattered ions. Two ring ion guides then lead the ions to the high-vacuum stages with a quadrupole mass filter followed by a second quadrupole of identical dimensions.

Two different detectors can be used according to the purpose of the experiment. When leaving the second quadrupole, ions can be pulsed perpendicularly towards the "time-of-flight" (TOF) mass analyzer for acquisition of the mass spectrum, or be detected directly by the linearly positioned detector in order to record the time the ions take to cross the cell (arrival time distributions, ATD).

To perform IRMPD spectroscopy on conformer and *m/z*-selected species, conformers of a given mobility can be selected by means of electrostatic deflection after the drift tube so that only ions within a narrow range of drift time are allowed to enter the mass filter where the *m/z*-selection takes place. Isolated species are irradiated with infrared radiation provided by a high coherent light source, the in-house free-electron laser (FEL). Multiple photons are absorbed inducing subsequent fragmentation, which is detected with the TOF analyzer. The IRMPD spectrum is obtained by recording the fragmentation yield as a function of the wavelength in the infrared range, as previously described in section 2.2.6. The typical experimental parameters used in this thesis are listed in Table 2. All the parameters were optimized in each experiment in order to obtain a good signal for the investigated species.

All spectra were scanned twice from 1400 to 1800 cm^{-1} and averaged. The measurements were carried out using different laser power settings. The term “high” laser power settings refers to more focused conditions and 100% attenuation, assuming that radiation with approximately 100 mJ energy is produced. “Low” laser power settings refer to less focused conditions and less attenuation.

Table 2. Typical parameters for DT-IM.

Drift pressure (He)	3–5 mbar
Electric field inside of the DT (V/cm)	10–20 V/cm
Temperature	20–25 °C
Needle voltage	0,5–1,2 kV
Injection voltage	30–150 V
Drift voltages	850-1200 V
RF entrance funnel	300–700 kHz
RF exit funnel	350–500 kHz

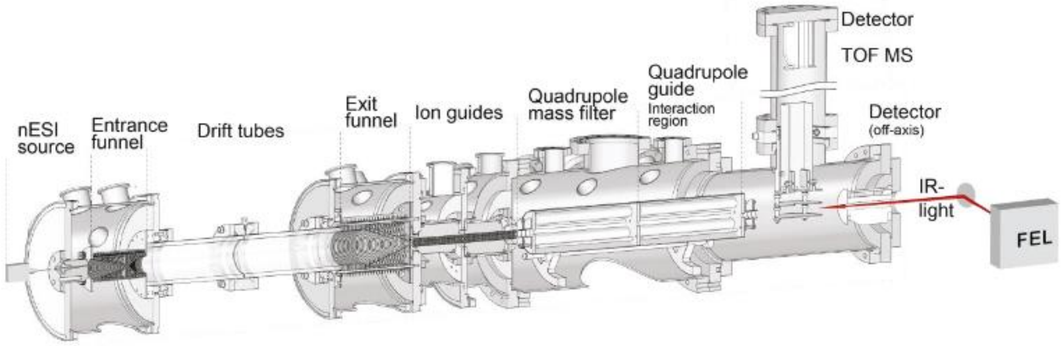

Figure 14. Schematic representation of the home-built Drift Tube-Ion Mobility spectrometer (DT-IM-MS).

3.4 Fitting Procedure of the IRMPD Spectra

Three distinct methods were used in this thesis to evaluate the amide I band. The position of the absorption bands are determined by its center at the full width half maximum (FWHM) as depicted in Figure 15 for an individual scan of one hIAPP conformer. When the amide I band has a reproducible shape, i.e. similar shapes are observed over a series of measurements and with different instrument conditions, the position at the maximum intensity is determined “by eye” as a particular feature of the band.

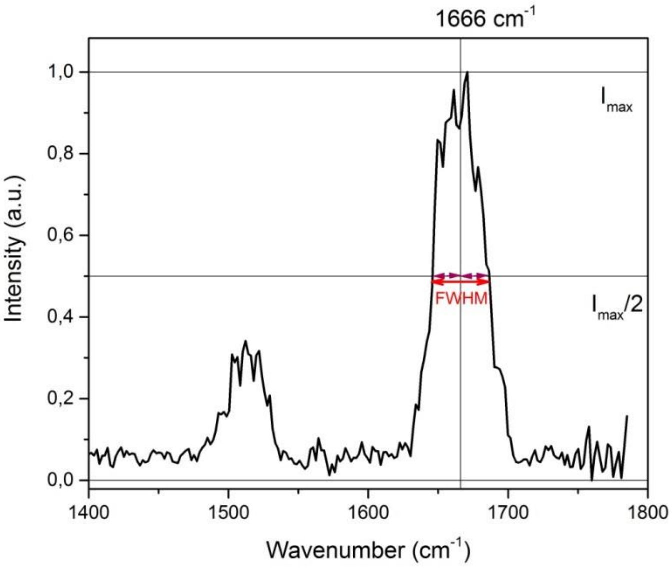

Figure 15. Determination of the center position of the amide I band.

When applicable, deconvolution of the amide I band were performed in order to estimate the β-sheet content within the peptide as commonly applied in condensed phase. However, gas-phase IR spectroscopy is governed by the more complicated IRMPD process and the resulting IR intensity is not a direct function of the number of absorbed photons. The content of β-sheet motifs contributing to the spectral band can still be derived from the deconvolution of the IRMPD spectrum. In this procedure, the spectral features are fit with multiple Gaussian functions according to the equation 3.10.

$$\mathrm{I}=\sum_n \frac{A(n)}{\sigma(n)*\sqrt{\pi/2}} * exp\left[-\frac{2\{x-x_c(n)\}^2}{\sigma(n)^2}\right] \tag{10}$$

where the parameters $x_c(n),\ \sigma(n)$, and $A(n)$denote the peak center, peak width and area of the *n*-th Gaussian, respectively. The amide I features at 1600-1700 cm^{-1} are fitted with six Gaussians using the constraints in the peak center and width shown in Table 3. The Gaussian at 1560–1600 cm^{-1} (n=0) is used to correct the baseline below 1600 cm^{-1}. The fraction of β-sheet signature, *F(β)* is determined from the areas of the Gaussians according to equation 3.11, where *A(n)* is the area of the *n*-th Gaussian. The A(6) is taken into account only for antiparallel β-sheet-containing peptides whereas for parallel β-sheet structures only Gaussian A(1) and A(2) is needed.

$$F(\beta) = \frac{A(1)+A(2)+A(6)}{\sum_{n=1}^{6} A(n)} \tag{11}$$

Table 3. Constraints in the peak center and width for the fitting amide I with multiple Gaussians.

n	Peak center	Peak width (σ)
0	1560–1600 cm^{-1}	0–30 cm^{-1}
1	1600–1630 cm^{-1}	0–30 cm^{-1}
2	1620–1640 cm^{-1}	0–30 cm^{-1}
3	1640–1660 cm^{-1}	0–30 cm^{-1}
4	1650–1680 cm^{-1}	0–30 cm^{-1}
5	1660–1690 cm^{-1}	0–30 cm^{-1}
6	1680–1710 cm^{-1}	0–30 cm^{-1}

3.5 Data Analysis

Analyzis of the obtained raw data (drift times, FT-IR and IRMPD spectra) and calculation of the collision cross-sections (CCSs) were performed using the program Origin Pro 2016 (OriginLab Corporation, Northampton, MA, U.S.A.). Data and schemes were depicted with Adobe Illustrator CS6 (Adobe Systems GmbH, München, Germany). All the IRMPD spectra were wavelength calibrated and power corrected.

4. RESULTS AND DISCUSSION

4.1 Model Peptides

Infrared spectroscopy has been shown to be a powerful tool to provide structural information of peptides and proteins. A suitable vibration to investigate the secondary structure of these biopolymers is the so called amide I band. The oscillation is related to the stretching vibration of the C=O bond present in the peptide backbone. The position of the amide I is hardly affected by amino acid side chains but is highly sensitive to the intramolecular hydrogen bonding pattern and that is specific to the secondary structure.[72] Since shifts in the position of the amide I are an indicative of structure transitions, IR spectroscopy can be used to probe the structure of the intermediary oligomeric species of amyloidogenic peptides as well as follow the process of amyloid formation. To interpret the experimental data, IR spectra of so called model molecules can be used to compare the position of vibrational bands. These models should have a well-defined and also well-studied secondary structure. In condensed phase, IR spectra of various model peptides are readily available. In the gas phase, however, the availability of IR spectra of comparable molecules is limited. Nevertheless, the position of IR bands should not be strongly shifted and it is common to reference the position of IR bands in the condensed phase.

To find suitable candidates for model peptides in the gas phase, three peptides were chosen according to their structures determined by other analytical techniques. The IR spectra of *m/z*- and conformer-selected species were measured and compared with the spectra in solution-phase. A alanine based peptide serves as a model for helical structures. The pepetide tendamistat and the structurally restrained peptide protegrin were chosen to investigate β-sheet and β-hairpin secondary structures, respectively, in the gas phase.

4.1.1 POLYALANINE

The strong α-helix forming character of alanine amino acids and the ability of long-chain polyalanine peptides to form α-helices in solution at physiological conditions have been already reported from studies based on condensed-phase techniques.[77-79] Theoretical studies and experiments performed in the gas phase showed that an α-helix is the preferred structure of polyalanine carrying a Lys residue at the C-terminus.[78-80] Within this thesis, ion mobility and IRMPD spectroscopy experiments of the 20-residue peptide Ac-Ala_{19}-Lys-OH are performed. IRMPD spectrum of Ac-Ala_{19}-Lys-OH has been previously measured using a different experimental set-up. For further information on IRMPD spectroscopy of alanine based peptides, the reader is kindly referred to Schubert's work.[80] The investigated peptide is capped at the N-terminus with an acetyl group to avoid protonation at this site. The mass spectrum and the ATDs are shown in Figure 16. The mass spectrum shows the singly charged monomer whose protonation site is likely the sidechain amino group of lysine.[78]

The singly and double charged monomers have very similar collision cross sections of 374 and 364 $Å^2$ respectively suggesting the same overall structure for both ions. The measured CCS values are also in agreement with the cross sections obtained for the same peptide previously reported by Jarrold and coworkers, who assigned helical structures for these alanine-based peptides in the gas-phase.[79]

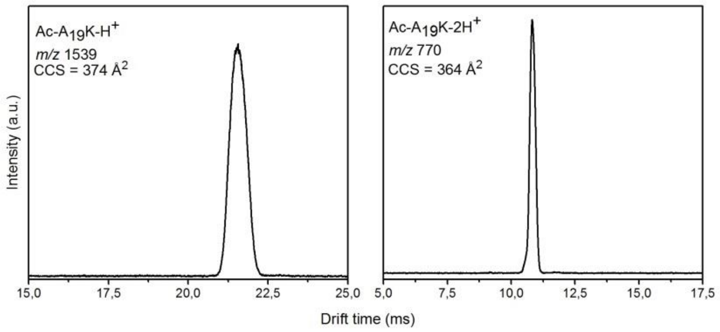

Figure 16. ATDs of singly and doubly charged Ac-Ala$_{19}$-Lys-H monomers.

The *m/z*- and conformer-selected singly charged monomer was further interrogated with laser light. The absorption of resonant light lead to fragmentation of the peptide, producing b and y fragments. The resulting IRMPD spectrum is shown in Figure 11 (Section 2.2.6). The narrow amide I band centered at 1667 cm^{-1} indicates that Ac-A$_{19}$-KH$^+$ ion adopts a helical conformation in vacuum, as also predicted by theoretical calculations.[79, 81] According to Jarrold, the helix is stabilized in vacuum mainly by two factors: an optimized hydrogen bonding and the interaction of the charge with the helix dipole.[78]

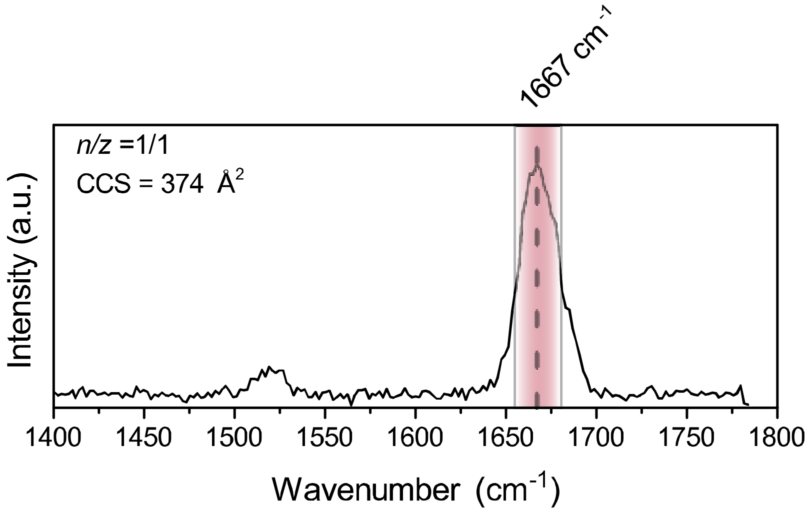

Figure 17. Gas-phase infrared spectrum of the conformer-selected Ac-Ala$_{19}$-KH$^+$ ion. The region colored in pink demarcates the typical absorption region for α-helix secondary structure.

To investigate and compare the secondary structure in solution, the IR spectrum of the peptide dissolved in ^2H_2O to a final concentration of 7,5 mg mL^{-1} was measured with a commercial ATR-FT-IR spectrometer The spectrum in the range of 1550 to 1750 cm^{-1} (Figure 18) shows the amide I band positioned at 1674cm^{-1}. A shift in the position of the amide I band with relation to the gas-phase spectrum is yet expected since condensed-phase and solvent-depleted environments provide different levels of perturbations for the C=O oscillators. Nevertheless, the positions of the amide I bands in the gas phase and condensed phase are comparable.

The ion mobility and spectroscopic results presented here, together with previous published theoretical and experimental work[78-80] supports the choice of the polyalanine-based peptide Ac-Ala_{19}-Lys-OH as a model peptide for α-helix structures in the gas-phase.

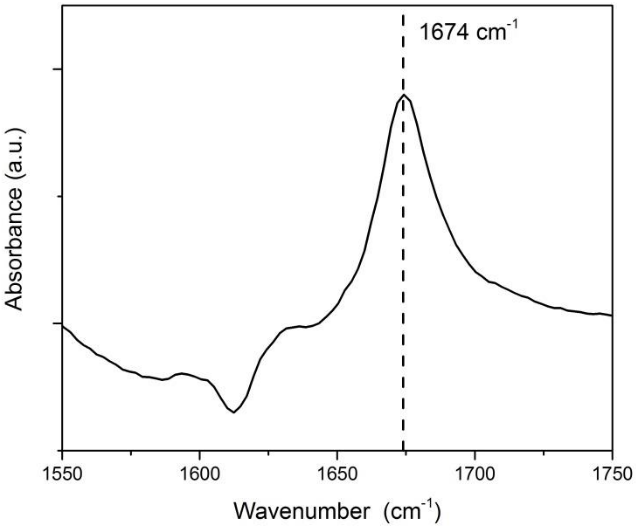

Figure 18. ATR-FTIR spectrum of the peptide Ac-Ala_{19}-KH^+.

4.1.2 *TENDAMISTAT*

The first candidate for the investigation of a β-sheet containing pepetide in the gas-phase is the α-amylase inhibitor peptide tendamistat. Tendamistat consists of 74 amino acid residues (7958 amu) containing two disulfide bridges between the Cys^{11}-Cys^{27} and Cys^{45}-Cys^{73}. It is known for its tight binding to mammalian enzyme α-amylase.[82] Its secondary structure in solution previously determined by NMR contains two three-stranded antiparallel β-sheets interconnected by loops and irregular structure.[83] Its large propensity for β-sheet conformations and the absence of α-helical structures in the condensed phase make tendamistat an attractive model peptide to indicate β-sheet secondary structure of size- and *m/z*-selected species.

In order to perform IRMPD spectroscopy, fragments of the investigated molecule have to be easily generated upon absorption of multiple photons provided by an intense IR laser light source. Because of the relative high stability of large peptides, their complexation with other molecules can produce known fragmentation channels obtained with absorption of less photons, which can be used to obtain a good quality IRMPD spectrum. Crown ethers were reported to be a useful tool in charged amino acids recognition in gas-phase.[84] Here, we use the 18-crown-6 (18c6) complexation ability with protonated lysine side chains to measure an IRMPD spectrum. The Figure 19 shows the ATDs of the quadruply and quintuply charged ions. The +4 ion has a CCS of 904 Å^2 whereas two conformers were fitted in the broad ATD of the +5 ion with 913 and 970 Å^2.

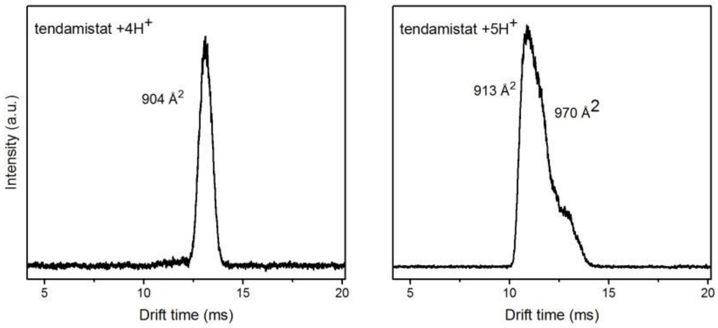

Figure 19. ATDs of monomeric tendamistat ions.

The bare +5 ion was selected to perform IRMPD spectroscopy due to the insufficient signal of the ion complexed with 18c6 molecule. The IRMPD spectrum of the 5$^+$ ion features a symmetric amide I band centered at 1665 cm^{-1}, a typical region for α-helical and turn-like structures. This could be associated to the loss of the β-sheet structure during transfer from solution into the gas-phase as a result of Coulomb repulsion and intramolecular self-solvation disrupting the hydrogen network.[84] In addition, the broader and asymmetric amide I band for the +4 tendamistat-18c6 complex displays a high intensity around 1640 cm^{-1} which could indicate some content of β-sheet motif. The +4 ion experiences less Coulomb repulsion and its native-like structure could be stabilized by its coordination to the crown-ether molecule which caps the protonated lysine side chain avoiding its collapse onto the protein backbone.[84]

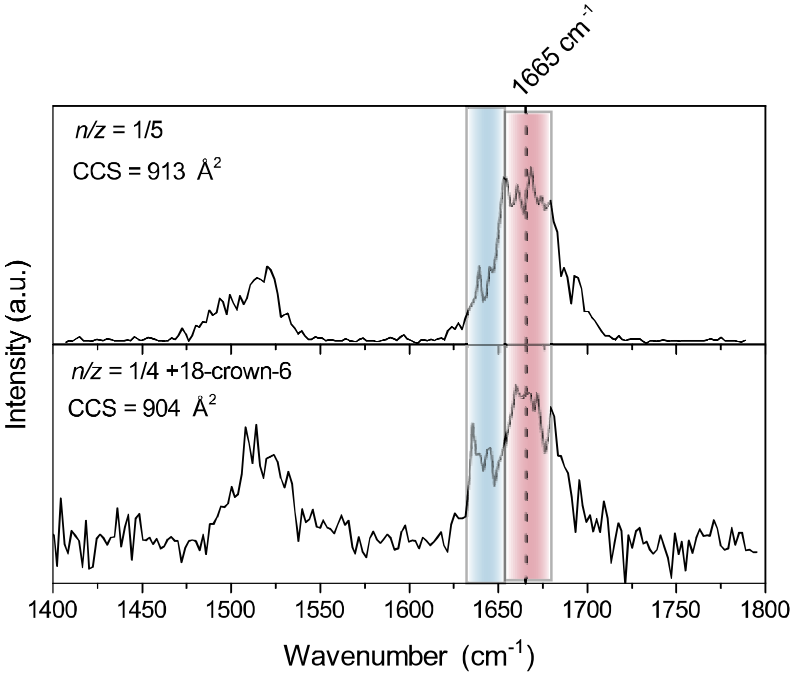

Figure 20. IRMPD spectra of *m/z*- and conformer-selected tendamistat ions. The regions colored in blue and pink demarcate the typical absorption regions for β-sheet and α-helix secondary structures, respectively.

In order to compare the structure of tendamistat in vacuum and in the condensed phase, the IR spectrum was acquired in ^2H_2O in a concentration of 7,5 mg mL^{-1} with the ATR-FTIR instrument. The solution-phase structure of tendamistat has previously been reported to adopt mostly a β-sheet motif.[83, 85] The spectrum shown in Figure 21 displays a maximum absorption at 1639 cm^{-1} and a shoulder around 1675 cm^{-1}, both referred to as an indicative of β-sheet conformation. Moreover, the narrow band located at 1515 cm^{-1} can be attributed to the C-C stretching vibration of the aromatic ring of tyrosine side chains.[85] The absence of any features which could be assigned to α-helical or unordered structures also confirms that tendamistat adopts mainly a β-sheet motif in solution. However, since the monomers do not show a β-sheet signature in the gas phase, tendamistat cannot serve as a proper model here.

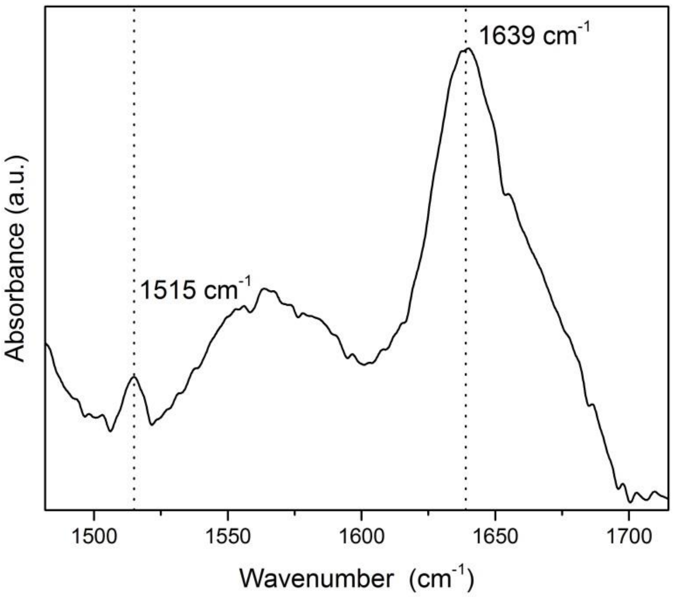

Figure 21. ATR-FTIR spectrum of tendamistat solution.

4.1.3 PROTEGRIN

Protegrins are small cysteine-rich antimicrobial peptides (AMPs) that contain 16-18 amino acid residues and possess a strong antibiotic activity. Their cytotoxic activity on cell membranes lies on the presence of positively charged amino acid residues which strongly interact with the negatively charged lipid headgroups of the outer leaflets of bacterial cell membranes.[86] The short peptide Progetrin-1 (PG-1) is composed of 18 amino acid residues and is one of the five native isomers known which were first isolated from porcine leukocyte cells.[87] Six positively charged arginine residues contribute to its antibiotic effect favoring the interaction with bacterial membranes.[88, 89] Four cysteine residues, form two intramolecular disulfide bonds at ^{6}Cys-^{15}Cys and ^{8}Cys-^{13}Cys positions that hold the peptide in a β-hairpin-like structure. More recently, MD simulations and AFM studies have shown that PG-1 has a similar behavior as the amyloidogenic Aβ peptides in solution and on lipid bilayers.[86, 90] On the anionic surface of lipid bilayers, PG-1 was reported to form ion channels with β-sheet subunit morphology similar to Aβ ion channels.[86, 90] Investigations using ThT staining and further MD simulations have suggested that PG-1 forms fibrils in water with twisted β-sheet morphology showing a cross β-structure which is also observed in amyloid fibrils.[86] These results and its restrained structure could potentially make PG-1 a good candidate for a β-hairpin model in the gas phase.

Due to the importance of the disulfide bonds in the stabilization of the β-hairpin conformation and in the biological activity of PG-1[87], we first performed IM-MS studies of the monomer both with open and closed disulfide bridges. The reduction of the disulfide bonds were carried out with 2-mercaptoethanol (ME) via the nucleophilic attack of the disulfide bond by ME and generation of a mixed disulfide intermediate.[91] The efficiency of the reduction with ME was confirmed by measuring the high-resolution mass spectra of the intact and reduced peptides.

Figure 22 shows the ATDs and the experimental CCs of the monomeric species before and after reduction of the disulfide bonds. As expected, the monomers with open disulfide bridges show slightly longer drift times as the reduction of the number of intermolecular interactions within the β-hairpin can lead to more expanded conformers. The diagram presented in Figure 23 shows the increase of the CCSs with charge state for the monomeric species. For both intact and open species in general, Coulomb repulsion leads to unfolding of more compact structures at low charge states into more extended conformations at higher charge states. Interestingly, no significant difference in the experimental CCSs for the doubly charged monomers was observed (395 Å^2 and 393 Å^2 for intact and open monomer, respectively). At lower charge states the disulfide bonds stabilize the structure of the β-hairpin and the electrostatic repulsion does not lead to a substantial change in CCSs. The effect of the disulfide bond breakage on the structure becomes more significant as the charge increases. All in all, the charge-induced unfolding of the monomers with open disulfide bridges is more pronounced than in the intact species.

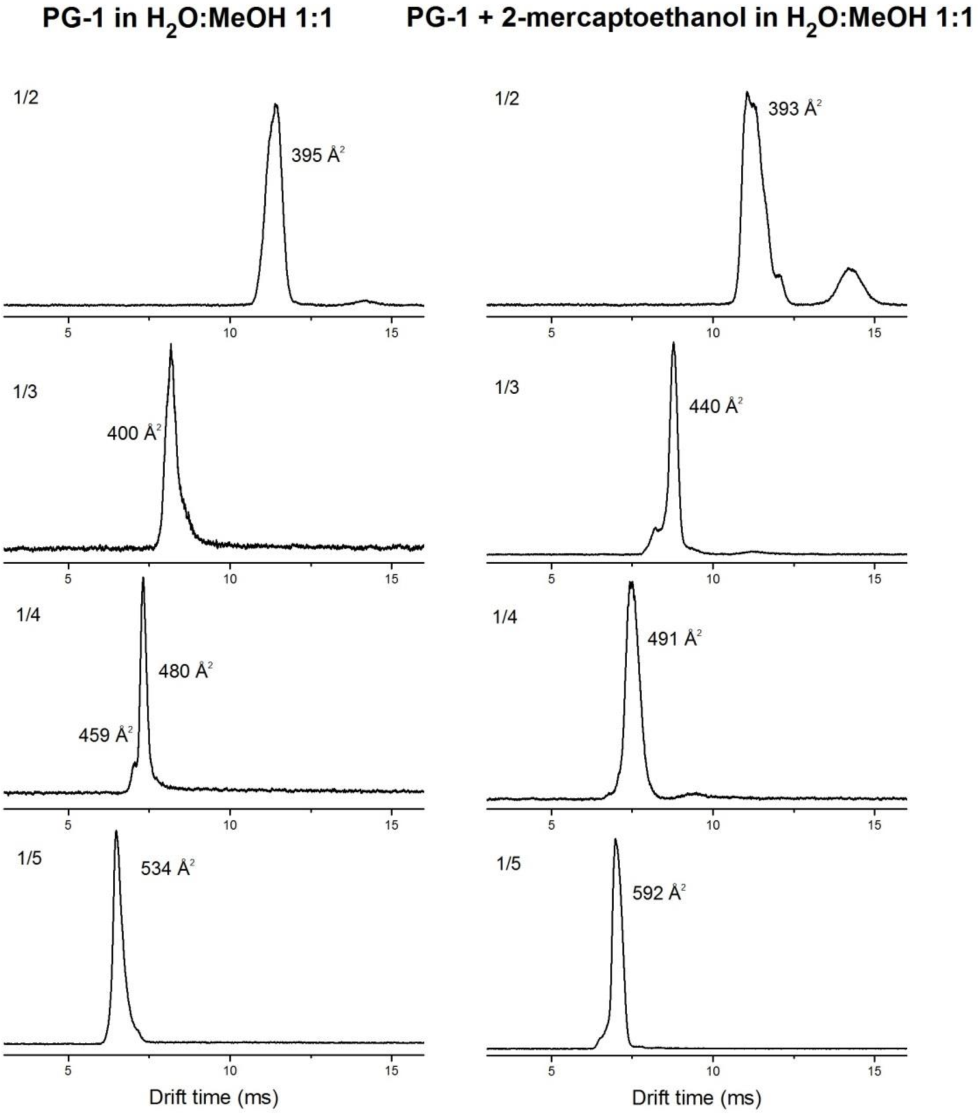

Figure 22. ATDs of the monomeric PG-1 ions with intact and reduced disulfide bonds.

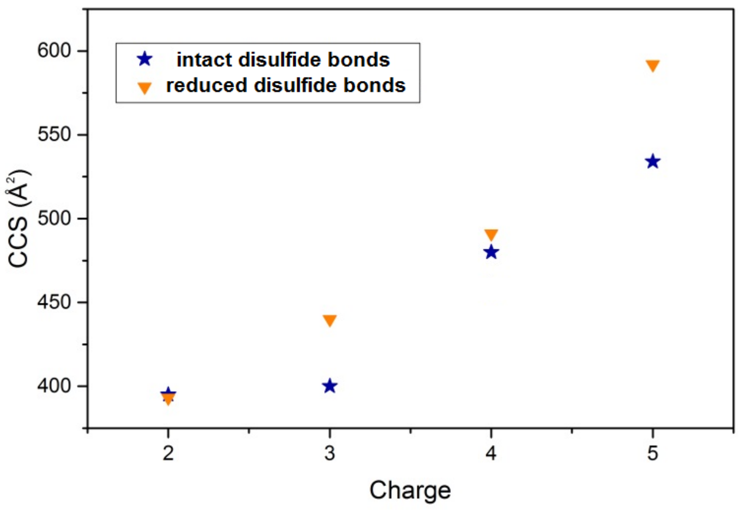

Figure 23. Plot of CCS vs. charge state for monomeric PG-1 with intact and reduced disulfide bonds.

In order to perform action spectroscopy with the PG-1 monomers, we again make use of the complexation ability of amino acid side chains with crown ethers. Protegrin possess six arginine residues with high affinity to dibenzo-30-crown-10 molecules (db30c10). The protonated guanidinium side chain of arginine residues form stable noncovalent complexes with db30c10 in the gas-phase. The stabilization of these complexes occurs through hydrogen bonding and ion dipole-interactions between the protonated guanidinium group and the 10 oxygen atoms of the crown-ether.[92] Prior to spectroscopy experiments, IM-MS experiments were performed. Each complexed crown ether adds a *m/z*-value of $\frac{536}{z}$ to the *m/z*-value of the bare ions, where 536,26 u is the exact mass of db30c10, *z* is the charge of the monomer and *n* is the number of complexed crown ethers (*n*=0 to 6). However, not all the possible adducts were observed in a measurable quantity.

The increase in the molecule's CCSs as the number of db30c10 increases is an expected effect due to the mass and size addition of each crown ether to the complex. Nonetheless, a counter effect is observed for +2 ions. The addition of the first db30c10 leads to a decrease of 7% in relation to the bare monomer's CCS and the second crown-ether increases the CCS only in 1.5% (See Appendix A.3 and Table A.1). This compaction effect was previously observed for specific peptides and charge states by Warnke *et al.* and is a result of the capping charged lysine residues that have no proximate interaction partner. In solution, the protonated guanidinium side chains of the arginine residues are either involved in salt bridges with TFA counter-ions or in interaction with solvent molecules.[84] In the absence of solvent, the charged side chains take part in intramolecular interactions, coordinating to the backbone carbonyl groups, which will not be available to participate in stabilizing hydrogen bonds. The disruption of the hydrogen bonds within the protein backbone can lead to the destabilization of the secondary and tertiary structures. When db30c10 is added, the protonated arginine side chains are capped with the crown-ether molecules. For the +2 ions the complexation of the first two db30c10 adds to two of the arginine side groups leading to a stabilization of a more compact structure.

An interesting observation is the increase in population of the compact conformer with cross section of 455 Å^2 of the bare quadruply charged monomer (*m/z* 539) when db30c10 is present in the solution. A possible explanation is that the attachment of db30c10 stabilizes the compact conformer in solution, whose structure is transferred into the gas-phase and the detachment takes place in the entrance funnel prior ion mobility separation. Alternatively, variations in the instrument settings such as needle voltage could promote the population of this conformation between two measurements.

To obtain more information on the secondary structure of the monomers, IRMPD spectroscopy was performed with the bare +3 ion, and with +3, +4 and +5 ions containing 3, 3 and 5 db30c10 molecules, respectively. The +4 ion containing 4 crown ether molecules was not investigated due to its similar *m/z*-ratio with other complexes and the limited mass resolution of the quadrupole mass filter. The obtained spectra are shown in Figure 24. All investigated monomeric species feature an amide I band centered around 1663–1665 cm^{-1}. This spectral region is typical for helical and type II β-turn secondary structures. According to Farhner *et al.*, the monomeric PG-1 in solution is described as an antiparallel β-sheet arrangement from residues 4 to 8 and 13 to 17 containing mostly non-polar amino acid residues whereas the residues 9–12 form the loop region characterized as a type II β-turn where the positive arginine residues are clustered.[93, 94] However, the residues 1–3 and 18 are not involved in the hydrogen network that stabilizes the β-sheet arrangement and were reported to be unstructured regions.[93, 94] The spectral position around 1660 cm^{-1} is difficult to interpret because two different structural motives can absorb here. With respect to the restrained structure, the IR signature for the monomers of PG-1 possibly indicates the presence of a type II β-turn secondary structure.

A noticeable feature present in all spectra of the monomeric protein-db30c10 complexes shown in Figure 24 is the high intensity of the peak near 1500 cm^{-1}. To ascertain the origin of this intense band, the ion of *m/z* 554 corresponding to the db30c10+NH_4^+ adduct is investigated and the spectrum is shown in Figure 24-e. The result shows that this peak mainly stems from vibration of the db30c10 and not from backbone amide I vibrations. The strong absorption at 1496 cm^{-1} close to the position of the amide II band is related to the aromatic ring stretching of the two crown ether phenyl groups.

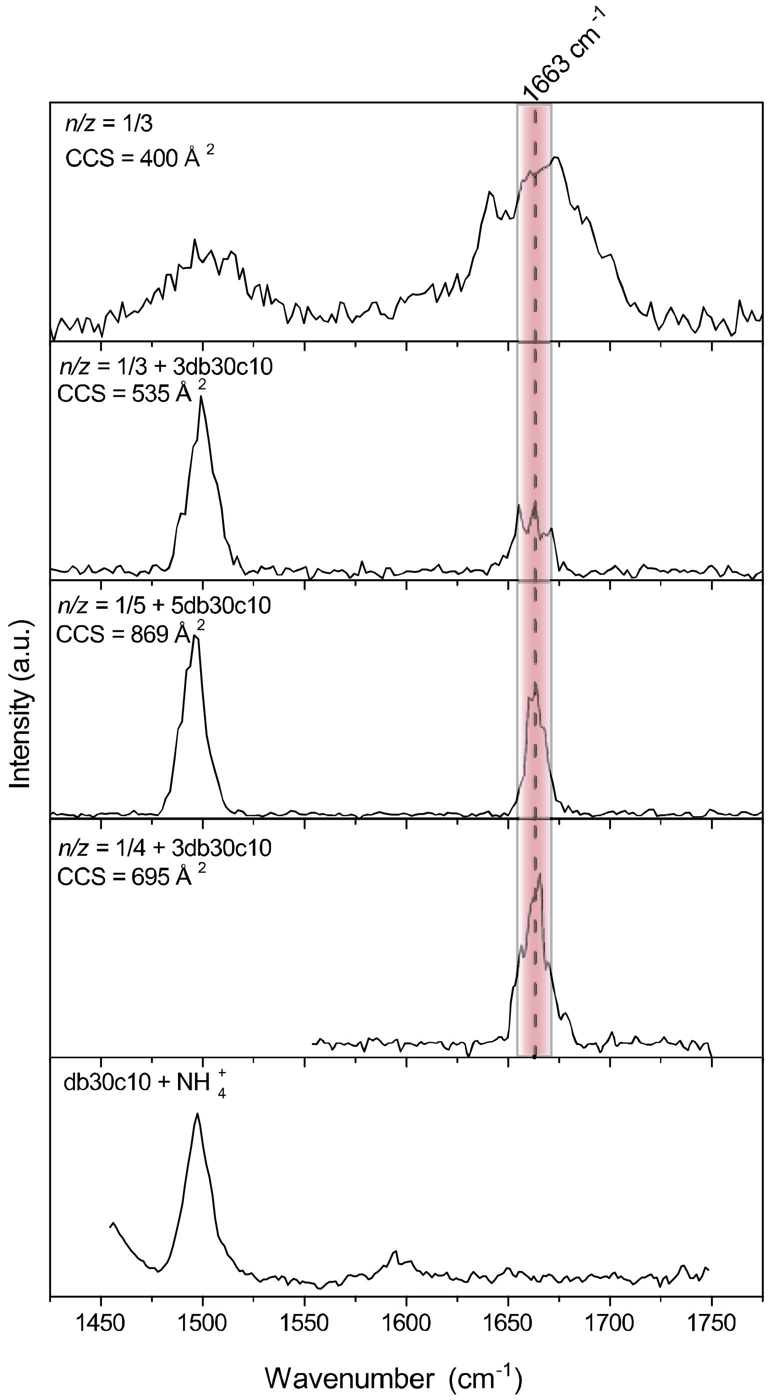

Figure 24. IRMPD spectra of *m/z*- and conformer-selected PG-1-crown ether adducts. The region colored in pink demarcates the typical absorption region for α-helix secondary structure. The spectrum of the adduct with *m/z*=941 were recorded from 1550 to 1750 cm^{-1}.

As the β-sheet content increases with oligomer size, we further performed oligomer-selective IRMPD spectroscopy using higher concentrated solutions to investigate the PG-1 assembly into dimers and trimers. Figure 25 shows the IRMPD spectra of the dimeric and trimeric PG-1. The spectra were acquired at low laser power settings so that the amide II band shows low intensity and the amide I band is well-resolved. The spectra of both species feature broad and asymmetric amide I bands so that only the position determined by the FMHW is not a good indicative of the secondary structure content of the molecule. The maximum absorption for the dimer and trimer occurs at 1650 cm^{-1} and 1645 cm^{-1} respectively. In addition to this main absorption regions, the dimer amide I band displays high intensities around 1670–1685 cm^{-1} and a shoulder at lower wavenumbers (approximately at 1625–1630 cm^{-1}). The same characteristic shoulders with lower intensity can also be observed at both sides of the amide I band in the spectrum of the +3/4 ion. These secondary spectral bands indicate a population of C=O oscillators absorbing at these wavenumbers, and therefore suggest the presence of more than one structural family. Although the absorption between 1645 and1650 cm^{-1} is the typical regions observed for random coil and α-helix secondary structures, the spectral bands at lower and higher wavenumber also suggest antiparallel β-sheet structures. One would expect, in this case, the maximum absorption around 1630 cm^{-1}, as a characteristic absorption for β-sheets. However, a β-hairpin absorbs at higher wavenumbers, because the vibrational excitons can delocalize over only two strands rather than 3 or more, which is necessary for lower β-sheet vibrational frequencies.[47] Another possible reason for the higher vibrational frequencies are the free C=O oscillators in the positions 1–3 which are possibly not involved in a strong hydrogen bonding network in the monomer.

The implication of antiparallel β-sheet arrangement is in agreement with previous MD simulations performed by Jang *et al.* which proposed two models for the dimer assembly: an antiparallel β-sheet with a turn-next-to-tail (shown in Figure 27) and a parallel β-sheet with a turn-next-to-turn.[94] In the turn-next-to-tail association, the characteristics of the amide I band of the gas-phase IR spectrum of the dimers and trimers supports the assumption of an antiparallel arrangement between the monomers. To estimate the β-sheet content, we deconvoluted the amide I region for the +2/3 ion (Figure 26). The deconvolution reveals a β-sheet content of 38% by employing the expected characteristic absorptions of the β-sheet secondary structures as constraints. Although this value is in agreement with previous results and modeling, this is only an approximation since is not possible to absolutely quantify the relative populations from a gas-phase IR spectrum.[36]

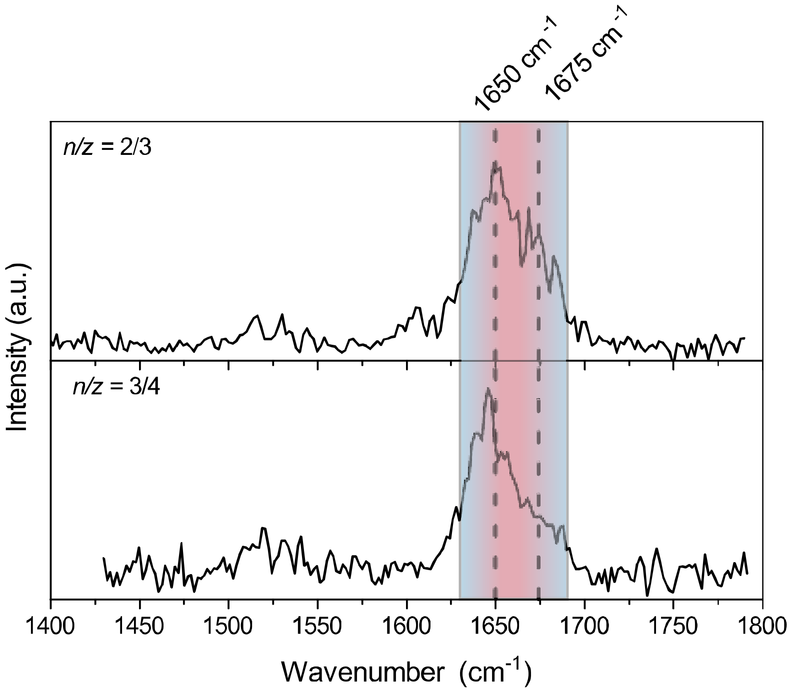

Figure 25. IRMPD spectra of *m/z*- and conformer selected PG-1 oligomers. The regions colored in blue and pink demarcate the typical absorption regions for β-sheet and α-helix secondary structures, respectively.

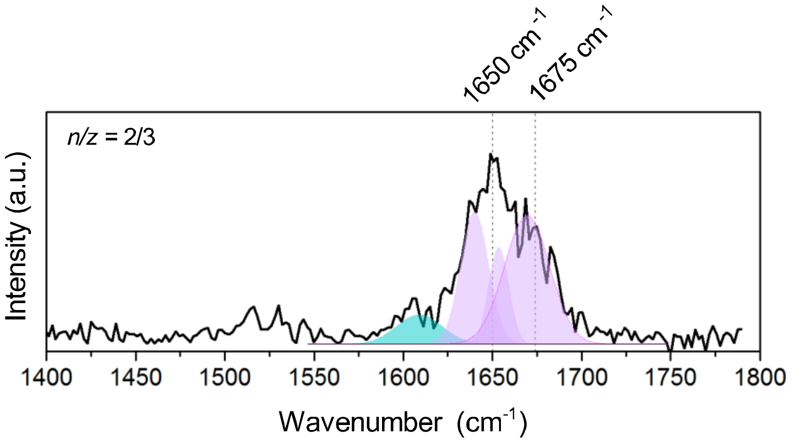

Figure 26. Deconvolution of the amide I band of the PG-1 dimer.

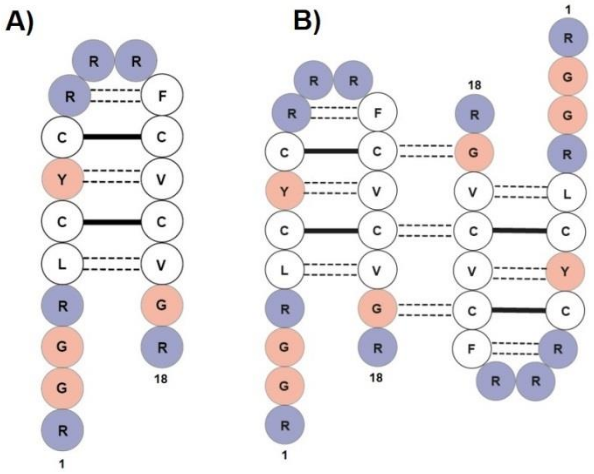

Figure 27. Topological diagram of PG-1 A) monomer and B) dimer in antiparallel β-sheet. Solid lines indicate the disulfide bonds, and dotted lines indicate hydrogen bond. Positively charged Arg residues are depicted by purple beads, whereas polar and hydrophobic residues are depicted by shell pink and white beads, respectively. Reproduced from Jang *et al.*[94]

In conclusion, despite the well-established structure of PG-1 monomers in solution, the gas-phase spectra cannot be used as a model for a β-hairpin. In contrast to the α-helix secondary structure, which is defined by a uniform and well-defined conformation, β-sheet and β-hairpin comprise a much broader conformational class involving a wide range of topologies as a result of different assemblies of multistranded arrays[95], and therefore, the seek for an ideal model for monomeric β-hairpin in the gas-phase is challenging. However, characteristic signatures for β-hairpin start appearing for oligomers. Based on the broad and asymmetric features of the amide I band, i.e. a secondary population of oscillators absorbing at higher and lower vibrational frequencies, the spectrum of the PG-1 low-order oligomers could in principle be used as a reference for β-sheet content.

4.2 Human Islet Amyloid Polypeptide

Aggregation of human islet amyloid polypeptide (hIAPP) and extracellular accumulation of amyloid plaques has been increasingly associated with the pathogeny of type 2 diabetes.[10] Recent studies have proposed that early intermediary oligomers are the toxic species instead of the mature fibrils and different aggregation trajectories and oligomerization pathways for hIAPP have emerged supported by different experimental techniques in combination with theory. Interestingly, although they differ only in six amino acid residues in the “core mutation region” (R18H, L23F, P25A, V26I, P28S, and P29S, as shown in Figure 28), human IAPP forms fibrils composed by highly ordered β-sheet structures while rat IAPP does not form fibrils.[96]

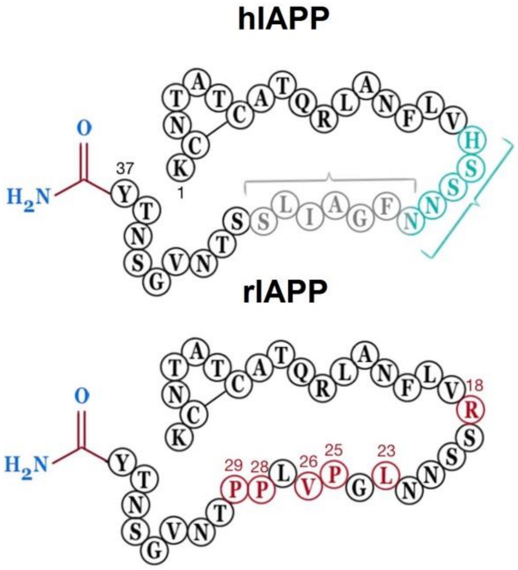

Figure 28. Comparison of primary structure of hIAPP and rIAPP. The section colored in grey show the amyloidogenic region (22–28). The cyan section represents the segments with high affinity toward metal ions. Differences in residues in the primary sequence of rIAPP are emphasized in red. Figure taken from Alghrably *et al.*[11]

Using a combination of IR spectroscopy and IM-MS, we here investigate the structure of the isolated early aggregation species, *i.e.* monomers and dimers, as well as differences between human and rat IAPP. The mass spectrum of hIAPP shows mainly the triply and quadruply charged monomers as well as the quintuply charged dimer. Smaller peaks can be assigned to the 1/5 and 2/7 ions. Higher-order oligomers are observed for neither the aforementioned peptide solutions nor solutions with higher peptide concentrations. The protonation sites on rIAPP are likely the Lys1, Arg11, and Arg18 residues for the 3+ charge state and protonation of the N-terminus generates the +4 ion. The +3 charge state of hIAPP arises from protonation of the Lys1 and Arg11 residues and the N-terminus. Further protonation of His18 gives rise to the +4 charge state. The protonation of His18 can either be a result of the ESI process or the solution pH.[8]

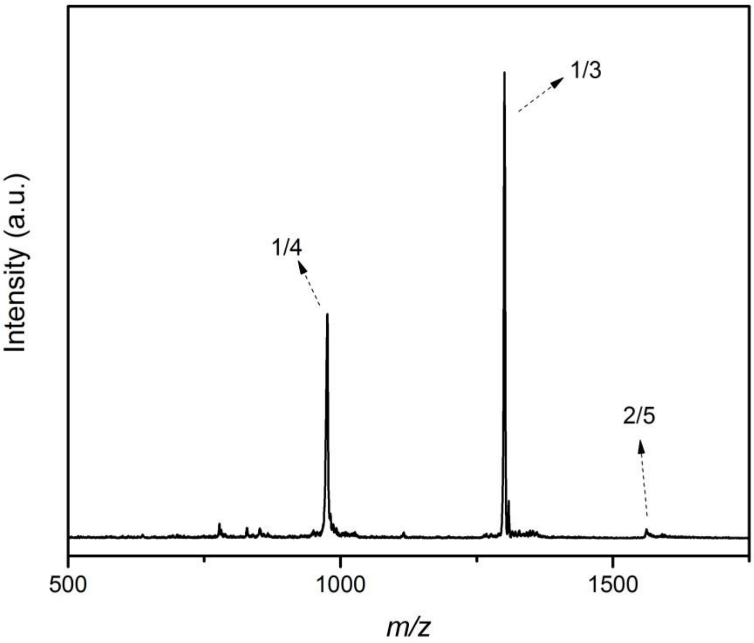

Figure 29. nESI time-of-flight mass spectra of hIAPP solution.

The first conformational insight into the monomers and dimers are obtained from ion-mobility experiments. Figure 30 shows the ATDs for the monomeric and dimeric ions of the human and rat variants and the respective experimental CCSs are listed in Table 4.

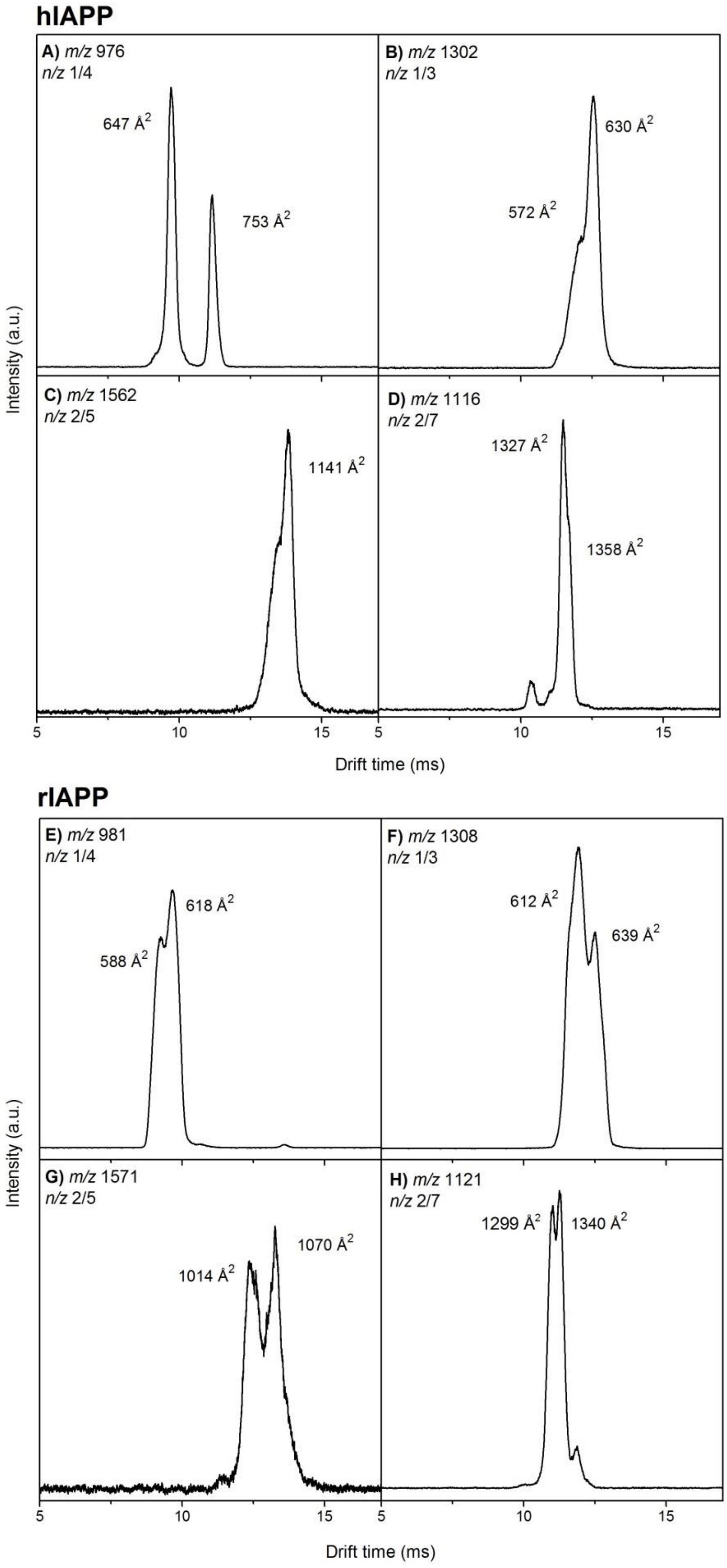

Figure 30. ATDs of hIAPP and rIAPP ions.

Table 4. Measured CCSs of *m/z*-selected hIAPP and rIAPP ions.

Peptide	**CCS (Å^2)**			
hIAPP	1/4	647	753	
	1/3	572	630	
	2/5	1141		
	2/7	1327	1358	
rIAPP	1/4	588	618	
	1/3	612	639	
	2/5	1014	1070	
	2/7	1299	1340	1400

The ATDs of both hIAPP and rIAPP indicate the presence of two dominant groups of conformers for the +3 and +4 charge states as well as for the dimers. The +3 hIAPP have two major conformers with CCSs of 572 and 630 Å^2, and +3 rIAPP two conformers with 612 and 639 Å^2. The ATD of the +4 hIAPP shows two baseline separated peaks with CCS of 647 and 753 Å^2 while the ATD of the +4 rIAPP features two less well-resolved peaks with CCSs of 588 and 618 Å^2. The ATD for the quintuply protonated dimer of hIAPP has one major feature at longer drift times with a CCSs of 1141 Å^2 and the dimeric rIAPP shows two main peaks with CCS of 1014 and 1070 Å^2. In addition, 2/7 hIAPP and rIAPP ions were observed from the solutions containing Zn(II) and Cu(II), respectively. The broad shape of the ATDs, however, suggests the presence of minor structural families contributing to the arrival time distributions. The extended +3 conformer has a CCS that is 10% larger than compact conformer while the extended +4 conformer is 16% larger in CCS than its compact conformer. This large difference in CCS for the +4 ion suggests two conformational families with significantly different secondary structures.

Yet, the performed ion mobility studies do not provide direct experimental information about the secondary structure and structure assignment solely based on computational simulations can lead to erroneous interpretation. Here, we performed IRMPD spectroscopy of the early monomeric intermediates to extract further structural information. The Figure 31 shows the IRMPD spectra of the *m/z*- and conformer-selected hIAPP monomers.

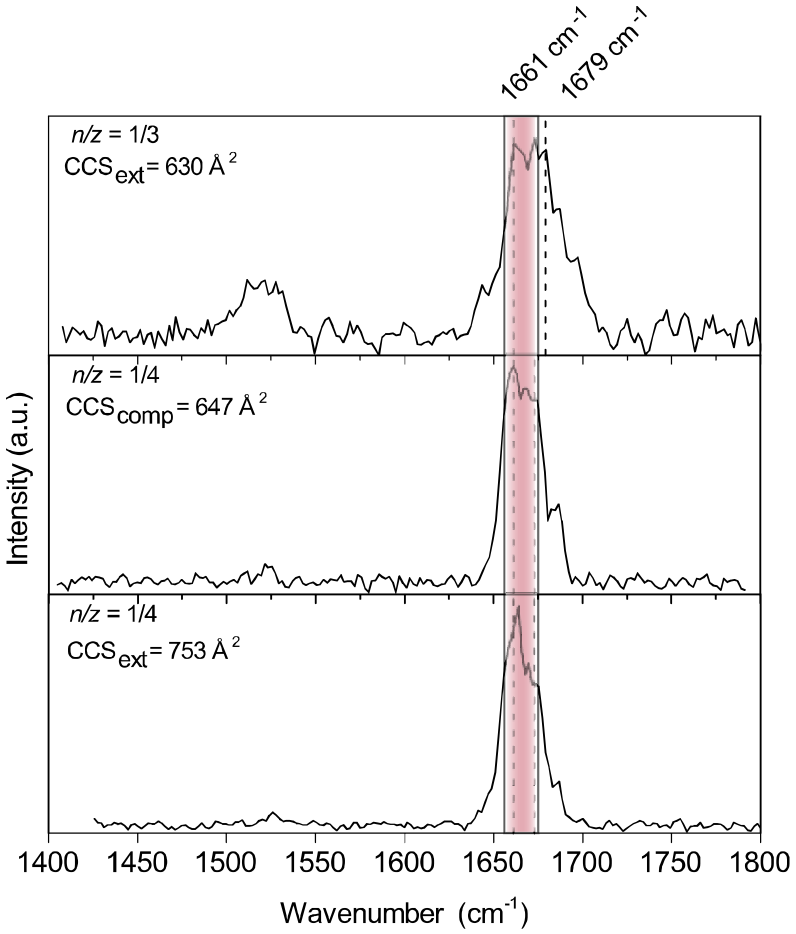

Figure 31. IRMPD spectrum of m/z- and conformer-selected hIAPP monomers. The region colored in pink demarcates the typical absorption region for α-helix secondary structure.

The IR spectra of the compact and extended +4 ions feature narrow amide I bands centered around 1665 cm^{-1}. They also display a characteristic maximum absorption at 1661 cm^{-1} and the most compact conformer a second maximum absorption at 1673 cm^{-1}. The spectrum of the +3 ion displays a broader amide I band centered at 1671 cm^{-1} with maximum absorptions at 1661 and 1679 cm^{-1}. It is important to emphasize the reproducibility of the maximum absorptions and the shape of the amide I band displayed by the monomers. Further, based on the knowledge that amyloidogenic oligomers are mainly composed of β-sheet structures and on previous observations that the extent of β-sheet increases with the oligomer size[49], we also investigated the secondary structure of the dimer (Figure 32). The dominant conformer of +2 /5 shows amide I band centered at 1663 cm^{-1} and maximum absorption at 1656 cm^{-1}. The spectrum of the extended conformer of the 2/7 ion displays a symmetric amide I band centered at 1663 cm^{-1}, whereas the compact conformer has a amide I band positioned at 1665 cm^{-1}.

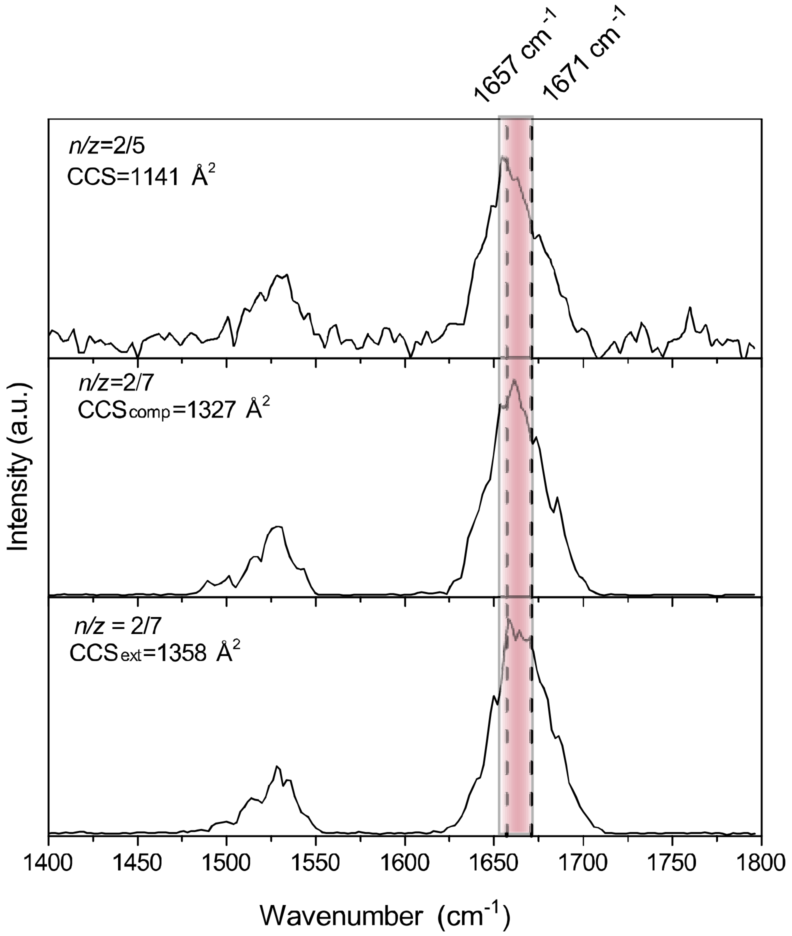

Figure 32. IRMPD spectrum of *m/z*- and conformer-selected hIAPP dimers. The region colored in pink demarcates the typical absorption region for α-helix secondary structure.

The similar characteristics compared with the IRMPD spectrum of polyalanine (Figure 17) presumably suggest a considerable extent of α-helix motifs within the peptide. The absence of β-sheet signature in the IR spectra of the monomers and dimers is consistent with results stemmed from solution-phase techniques previously reported by other groups.[41, 49]

In order to investigate structural characteristics of rIAPP oligomers that are related to its lack of amyloidogenicity, we also performed IR spectroscopy of the rIAPP species. The IRMPD spectra of the rIAPP monomers shown are shown in Figure 33. The amide I bands for both the compact and extended quadruply protonated monomers are centered at 1668 cm^{-1}. The compact conformer amide I band is slightly asymmetric showing a maximum absorption at 1660 cm^{-1}. The IRMPD spectra of +3 ions feature symmetric amide I bands centered around 1670 cm^{-1}. The spectrum of the compact conformer of the 2/5 rIAPP ion (Figure 34) displays an amide I band positioned at 1661 cm^{-1}, while the amide I band of the extended dimer is centered 1657 cm^{-1}.

The spectral features displayed by all the investigated species indicate predominance of helical structures. The higher vibrational frequencies shown by the +3 ions suggest the presence of turn-like motifs. Identification of spectral features that can be assign to α-helix motifs is in good agreement with previous solution NMR studies, which shows that the residues 5–19 adopt α-helical conformations[47], and with REMD simulations which also predicted α-helix- and turn-based structural families for the +4 rIAPP monomers.[8]

The absence of β-sheet structure for the rIAPP monomers is already expected as the rat form is known to be stable and non-amyloidogenic. The difference in the structure between the human and rat IAPP lies on the mutations sites in the region high β-sheet propensity. This region in the rIAPP sequence contains proline mutations which has an intrinsic low amyloidogenicity and are disruptive to secondary structure. Moreover, proline isomerization leads to multiple stable conformations of the peptide backbone, as can be seen in wide ATDs of rIAPP ions, and therefore inhibits symmetric self-association of the peptide.[42]

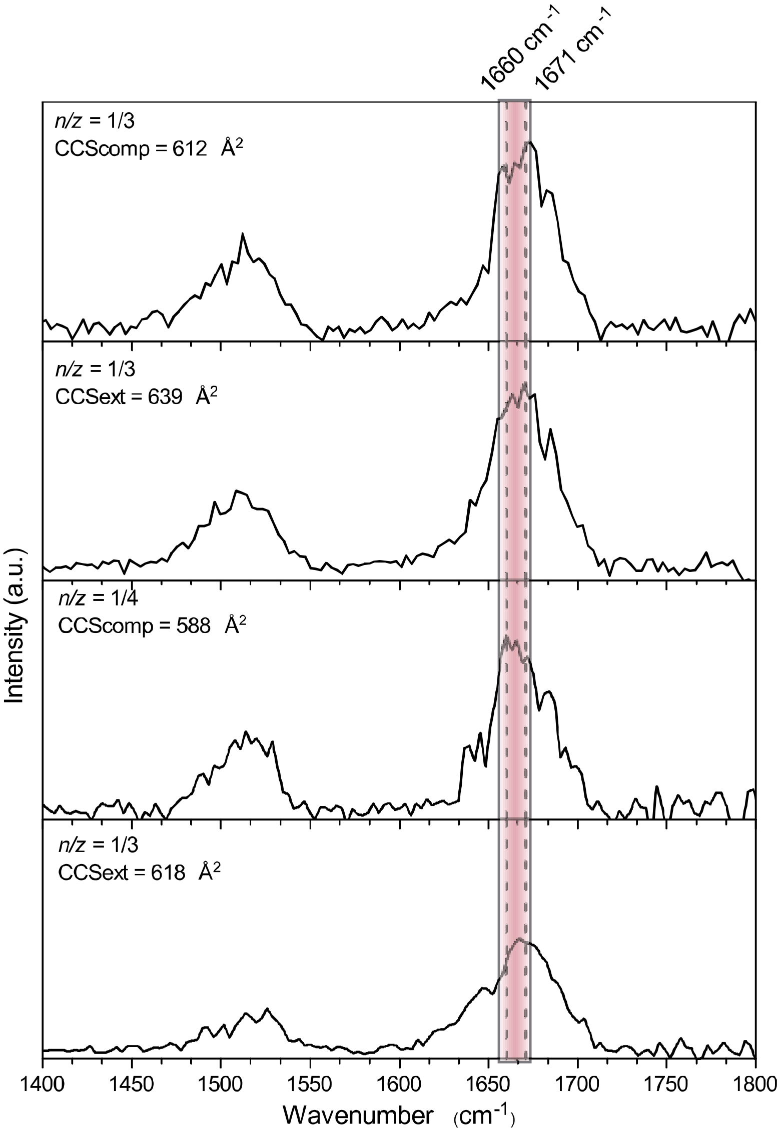

Figure 33. IRMPD spectrum of *m/z*- and conformer selected of rIAPP monomers. The region colored in pink demarcates the typical absorption region for α-helix secondary structure.

The absence of β-sheet features in the amide I band for monomeric and dimeric hIAPP species contrasts the aggregation mechanism where toxic β-sheet-rich oligomers are formed before nucleation. On the other hand, the results presented here suggest that another mechanism take place in the aggregation of hIAPP. Unfortunately, in the experimental conditions employed any higher-order oligomers were observed in a measurable quantity.

The aggregation process of amyloid peptides can be followed by FTIR spectroscopy. The solution-phase IR spectra of hIAPP and rIAPP shown in Figure 35 were recorded during 24 hours. The IR spectrum of hIAPP clearly shows the transition of random coil (1648 cm^{-1}) and α-helix structures to b-sheet-rich aggregates (1617 cm^{-1}). The formation of β-sheet-rich fibrils could be observed after 40 minutes. We also measured the solution-phase IR spectrum of rIAPP. The broad amide I band reveals an average of α-helix (1656 cm^{-1}), random coils (1641–1648 cm^{-1}) and β-sheet (1626 cm^{-1}) structures in solution. In contrast to hIAPP, no shift can be observed in the amide I band of rIAPP over 24h due to its stability towards fibril formation.

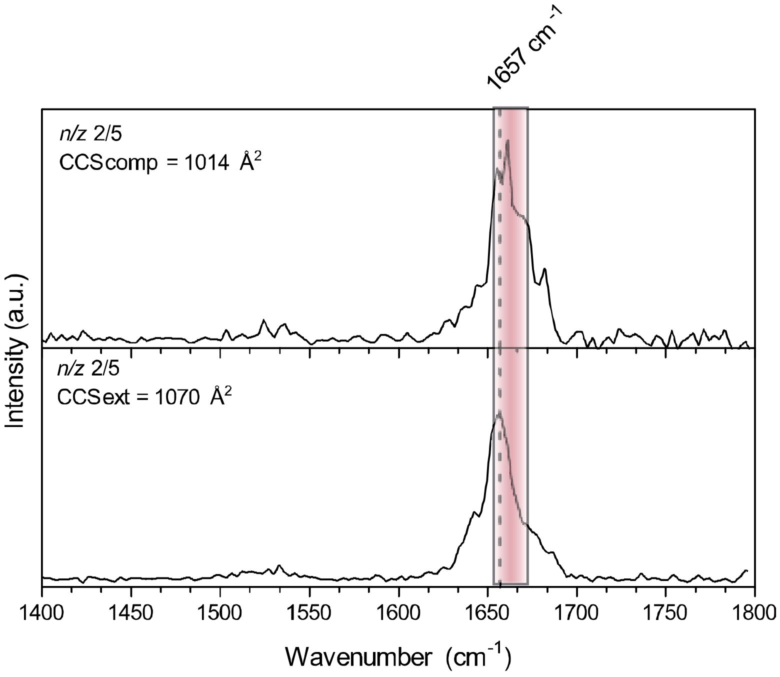

Figure 34. IRMPD spectrum of *m/z*- and conformer selected of rIAPP dimers. The region colored in pink demarcates the typical absorption region for α-helix secondary structure.

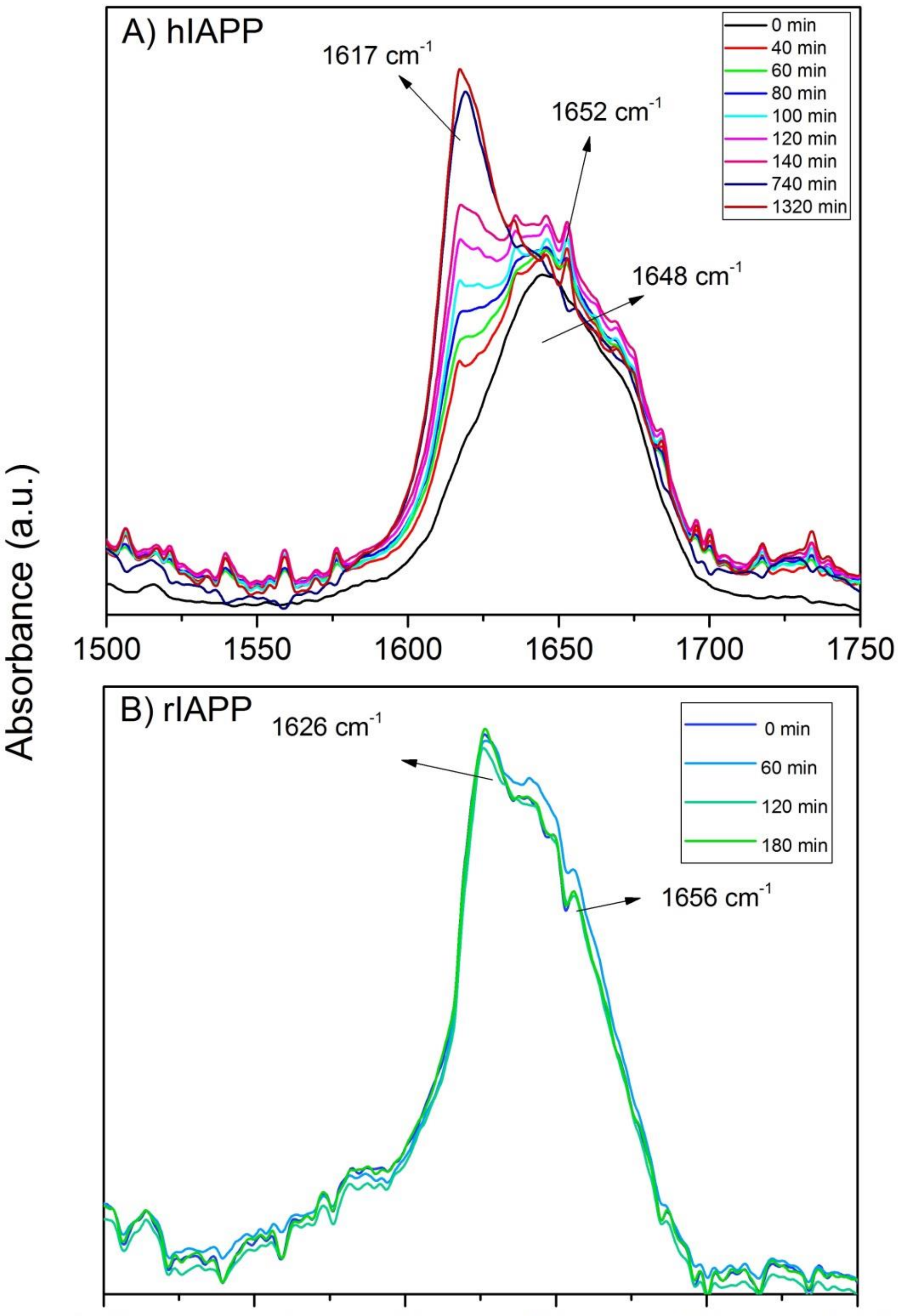

Figure 35. ATR-FTIR spectra of A) hIAPP and B) rIAPP solutions acquired as a function of time.

4.3 hIAPP – metal adducts

In addition to amyloid formation, elevated serum copper levels and zinc deficiency are also observed in patients affected by T2D. Several studies also have found correlation between the loss of fibril formation and metal-hIAPP association, suggesting that metal-coordination plays a role in hIAPP aggregation. We investigate here possible conformational changes upon adducts formation between hIAPP with Zn^{2+} and Cu^{2+} ions.

The measured mass spectra depicted in Figure 36 presents the similar charge distribution as the one obtained from the pure hIAPP solution. In addition to the +3 and +4 metal-free hIAPP monomers, the metal-associated +4 and +5 hIAPP are also observed with relatively high intensity. The relative intensity between the holo ($[hIAPP+M^{2+}+2H^+]^{4+}$, where M^{2+} is the metal ion) and apo ($[hIAPP+4H^+]^{4+}$) form is bigger for the Cu(II)-hIAPP than for the Zn(II)-hIAPP adduct. The relative affinity of copper towards toward hIAPP (K_a ~8.9×10^7 M^{-1}) is larger than for zinc (9.1×10^5 M^{-1}).[67] The higher affinity of Cu(II) toward hIAPP can also be used to explain the wider variety of adducts formed, including Cu(II) complexed with dimeric.

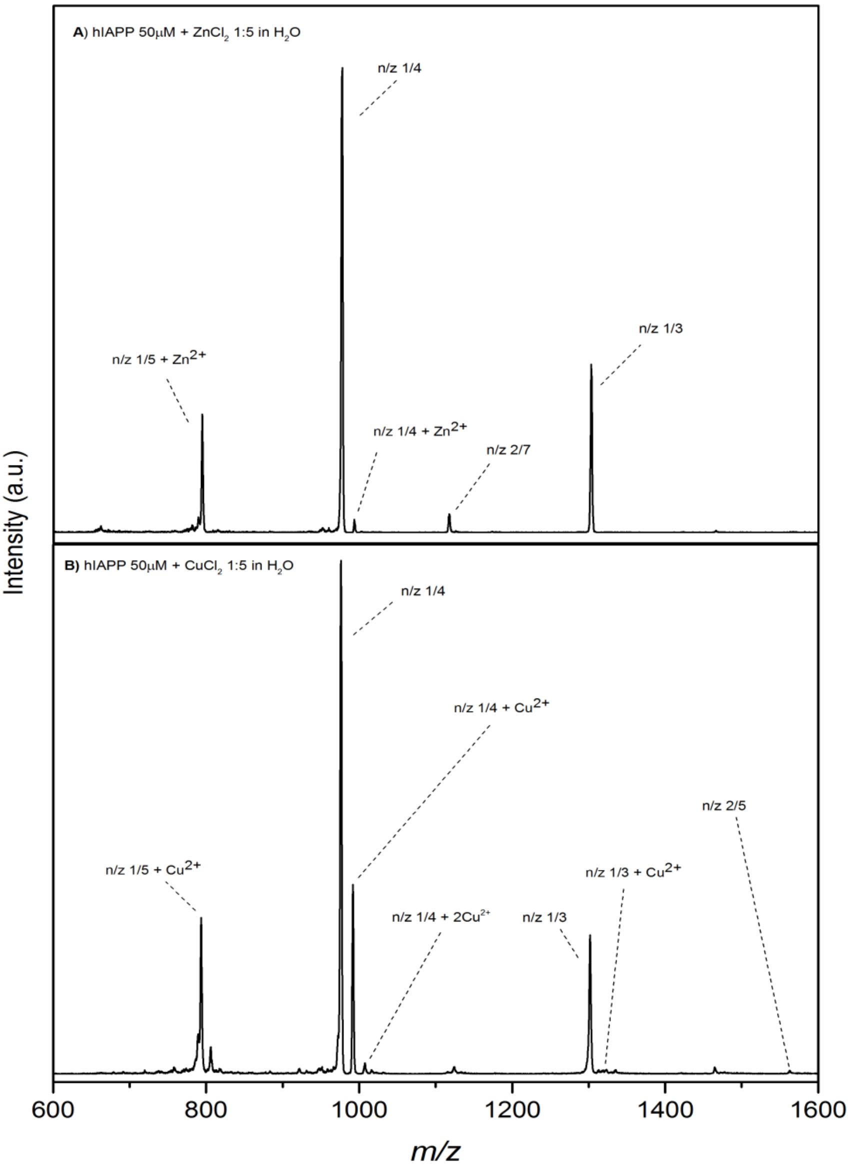

Figure 36. nESI time-of-flight mass spectra of A) Zn(II)- and B) Cu(II)-containing hIAPP solutions.

To better understand the role of metals in hIAPP structures, we investigated the conformational features of metal-associated hIAPP monomers and compared these to metal-free hIAPP. The measured ATDs for Zn(II)- and Cu(II)-bound hIAPP ions are shown in Figure 37 and 38. In addition to the major compact and extended conformers observed for the metal-free 4+ state, a third structural family with a CCS of 687 Å^2 is present for the Zn(II)-associated 4+ ion. The +5 charge state was also observed as a single conformer with cross section of 772 Å^2. The ATD for the +6 monomer features two equals populated structures with cross sections of 793 and 847 Å^2.

It is interesting to compare the ATD features of +4 metal-free hIAPP and Zn(II)-hIAPP. The relative abundance of the compact and extended conformers also change upon metal association. In the absence of metal ions, +4 hIAPP exists mainly in a compact conformation. When Zn(II) is added to the solution, the relative population of the extended structural family increases. This result suggests a higher affinity of Zn^{2+} by the extended conformer. In addition, our results show three well resolved peaks corresponding to three structural families for the +4 monomers.

We detected a similar trend for the Cu(II)-associated hIAPP. Cu(II) also preferentially binds to the extended hIAPP +4 monomer, and a third conformation with CCS of 702 Å^2 emerges from Cu(II)-hIAPP interaction. The broad ATDs for +3 and +4 ions bound to one and two copper atoms, respectively, indicate various conformations. For these species, multiple Gaussians were fitted and main features with cross sections of 621, 688 and 754 Å^2 for the +4 ion and 593 and 626 Å^2 for the +3 ion were assigned as the dominant structures. The results presented here contrast with the results reported by Lee and coworkers, which predict that Cu(II) preferentially associates to the compact hIAPP monomer.

At a first glance, the information obtained from the ion mobility studies suggests that both Zn(II) and Cu(II) in solution increase the relative abundance of the extended conformer. According to the Bowers's group, the extended conformer corresponds to a β-hairpin precursor to toxic oligomers, and therefore, these ions would have an inductive effect on hIAPP aggregation.[56]

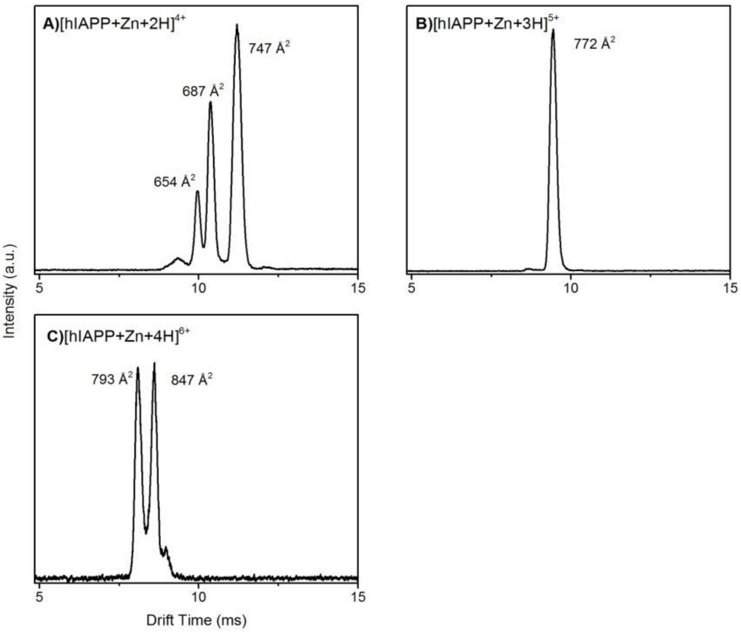

Figure 37. ATDs of *m/z*-selected Zn(II)-hIAPP adducts.

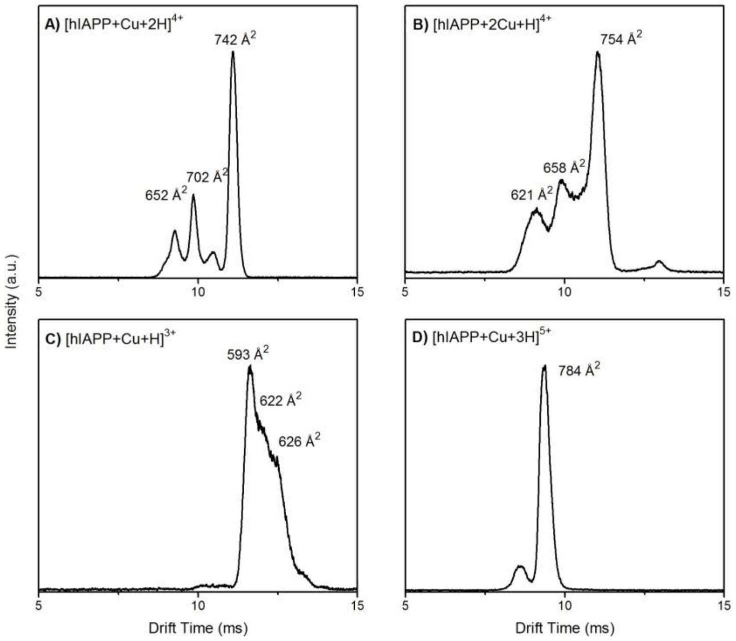

Figure 38. ATDs of *m/z*-selected Cu(II)-hIAPP adducts.

The secondary structure of hIAPP-metal adducts were probed by irradiation with IR light. The IRMPD spectra of the Zn(II)-hIAPP in the +4 charge state are shown in Figure 39. The center of the absorption band determined at the FWHM matches the amide I frequency in polyalanine (see Figure17). Yet, the peak of the most compact conformer appears to have two maximum at 1660 and 1677 cm^{-1} with equal intensities. The second compact conformer shows only one maximum at 1660 cm^{-1} and the second maximum reappears with weaker intensity in the amide I band of the most extended conformer. Likewise, the three Cu(II)-hIAPP conformers show absorption bands centered at 1667 cm^{-1} (see Figure 40). The amide I band of the most compact conformer also shows two maximum at 1660 and 1673 cm^{-1}. The center of the absorption band of the conformer with a CCS of 702 $Å^2$ matches with its maximum. In addition to maximums at 1658 and 1676 cm^{-1} can also be observed. The highest intensity of the absorption band of the most extended conformer occurs at 1660 cm^{-1}.

All the investigated species show spectral features typical of α-helical structures. This suggests that segments within the molecules possibly adopt α-helical conformations. The high population of C=O bonds in the compact Zn-hIAPP monomer absorbing at 1677 cm^{-1} might indicate also the presence of turn-like structures inside the peptide. These structures are also present in smaller proportions in the most extended monomer. Moreover, a slight blue shifted in the frequency in relation to the second maximum observed for the metal-free hIAPP +4 monomers, could suggest a local rearrangement within a turn-like motif to accommodate the zinc ion. The similar spectral features observed for the Cu-associated hIAPP species demonstrate that zinc- and copper-bound hIAPP adopt related secondary structures.

The similar content of secondary structures within the Zn- and Cu- associated hIAPP monomers even though Cu(II) and Zn(II) are reported to induce distinct hIAPP aggregation pathways, is an interesting result. According to the spectroscopic data, metal ions do not preferentially bind to a β-hairpin, but rather to an extended α-helix-rich conformation. Different effects and aggregation pathways have been proposed by other groups based on theoretical simulations, TEM, IM-MS and solution-phase spectroscopy. Our results, however, do not show any change in the morphologies of the early monomers and oligomers formed prior aggregation. It is also difficult to predict if metal ions have a toxicity inducing or inhibitory effect since it is still unclear which conformers are the toxic species formed during fibrillation.

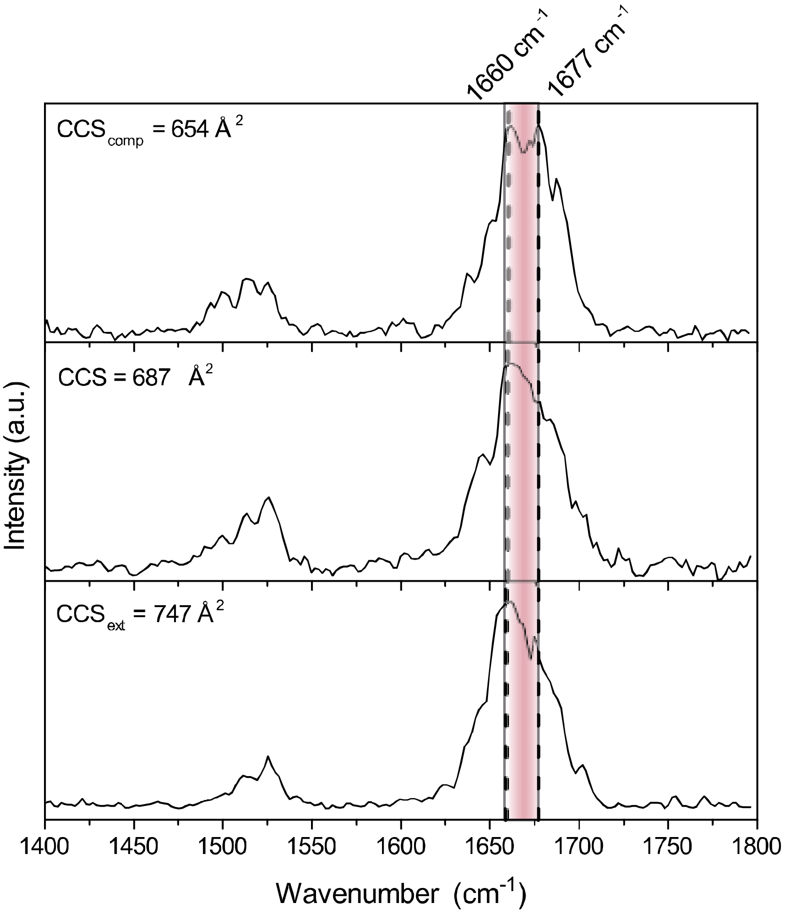

Figure 39. IRMPD spectra of Zn(II)-associated $[hIAPP+Zn+2H]^{4+}$ monomeric ions. The region colored in pink demarcates the typical absorption region for α-helix secondary structure.

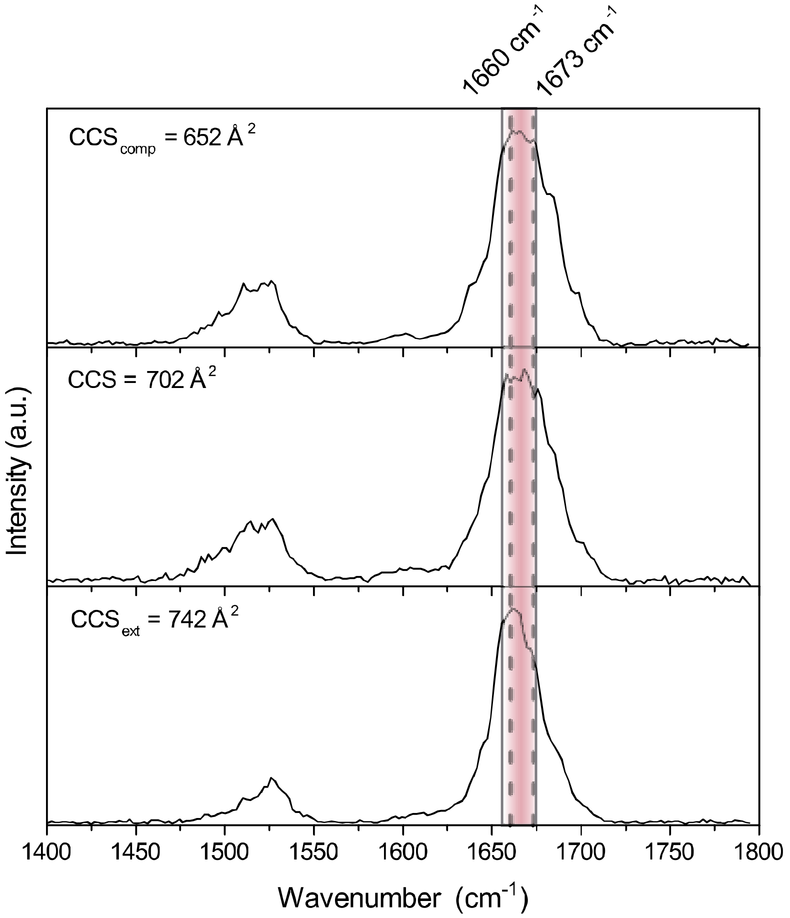

Figure 40. IRMPD spectra of Cu(II)-associated $[hIAPP+Cu+2H]^{4+}$ monomeric ions. The region colored in pink demarcates the typical absorption region for α-helix secondary structure.

4.4 Heterodimers

4.4.1 HIAPP:PRP

Observation of coaggregated heterogeneous pepetides *in vitro* and also the presence of hetero-associated pepetided *in vivo* have been giving evidence for a prion-like interplay occurring between various amyloidogenic proteins. The association between prion ($PrP_{106–126}$) and IAPP is particularly interesting as they show almost no sequence homology, and yet heterogeneous fibrils and aggregates have been observed.[97] In this thesis we performed IM-MS and IRMPD experiments in order to elucidate structural changes as a consequence of the heterogeneous co-assembly.

Heterodimers hIAPP:PrP and rIAPP:PrP were observed at the +4 and +5 charge states. The ATDs of hIAPP:PrP dimer at +4 and +5 charge states (Figure 41) show one dominant conformer for each species with cross section of 984 and 981 Å^2 respectively. In addition to the compact and extended conformations, a third structural family of the +4 heterodimer is populated with a cross section of 721 Å^2. The ATDs of the rIAPP monomers and heterodimers are likewise interesting. The most compact structure with cross section of 588 Å^2 is not observed in the presence of PrP in the solution, but two extended conformers emerge in these conditions with cross sections of 721 and 749 Å^2, similarly as observed for hIAPP. These results suggest that PrP induces the formation of extended conformations in both peptides, even though they show distinct propensities to aggregate. At the +4 charge state, the ATD of rIAPP:PrP heterodimers shows two dominant peaks with CCS of 934 and 1669 Å^2, the latter being assigned to the (4+4)/8 hetero-oligomer. The +5 heterodimers show a compact structure of 933 Å^2 and an extended structure with 1050 Å^2. The compact structures at both charge states have similar cross sections to hIAPP:PrP heterodimers, suggesting similar interaction between these two peptides and prion.

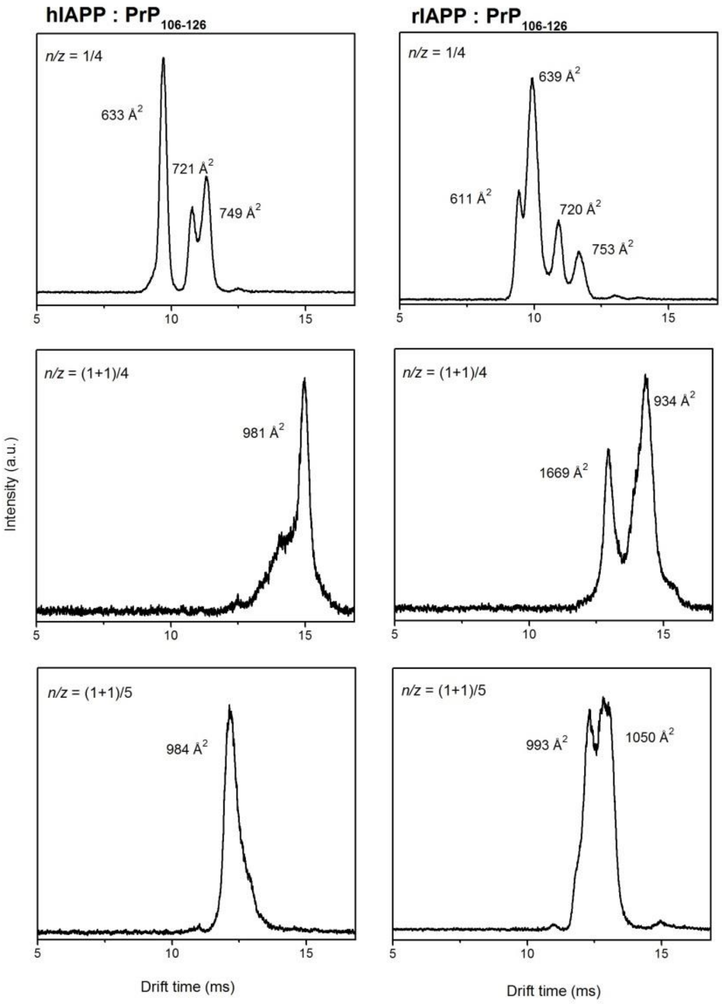

Figure 41. ATDs of m/z-selected hIAPP and rIAPP monomers and hIAPP:PrP$_{106–126}$ and rIAPP:PrP$_{106–126}$ heterodimers.

To gain insight on the content of secondary structures of the early oligomers, the hIAPP and rIAPP monomers as well as their heterodimers were further investigated with IR laser light. The IRMPD spectra (Figure 42) of the (1+1)/4 and (1+1)/5 hIAPP heterodimers resemble each other, where both feature amide I bands centered at 1664 cm^{-1}. The IRMPD spectra of the intermediary and extended +4 monomers (Figure 43) show asymmetric amide I bands centered around 1664 cm^{-1} with high intensities at lower (~ 1642 cm^{-1}) and at high wavenumbers (~1685 cm^{-1}). The IR spectrum of the hIAPP +3 monomer also shows a blue shifted amide I band. Its central position is located at 1671 cm^{-1} with high intensities around 1690 cm^{-1}.

The IRMPD spectra of the rIAPP 4+ monomers and rIAPP:PrP$_{106–126}$ heterodimers are shown in Figure 44. The spectrum of the heterodimer at +4 charge state features an amide I band centered at 1667 cm^{-1}, while the +5 heterodimer shows amide I bands positioned at 1661 cm^{-1}. Figure 45 shows the IRMPR spectra of the rIAPP monomers measured from the solution containing $PrP_{106–126}$. The conformer with a cross section of 611 $Å^2$ has an amide I band centered at 1671 cm^{-1}. A slight red shift is observed for the monomer with CCS of 720 $Å^2$ whereas the spectrum of the most extended conformer with CCS of 753 $Å^2$ shows an amide I band shifted to higher wavenumbers.

The absorption frequencies and the shape of the bands displayed be the investigated species suggest structurally distinct conformations. The center of the amide I band featured by both dimers matches with the position of its maximum intensity in the typical region of α-helix structures. As reported by Ilitchev *et al.*, the region 8-20 of hIAPP is responsible for interaction with PrP. This region is known to adopt α helical conformation.[97] Interestingly, the spectra of the hIAPP monomers originating from the solution containing $PrP_{106–126}$ resemble the spectra of the PG-1 oligomers rather than spectra of hIAPP from the pure solution. Since the amide I bands of PG-1 dimer and trimer spectra are also flanked on both sides, comparing these spectral features could suggest in principle some antiparallel β-sheet content within the hIAPP monomer. However, the spectra of the monomers in the solution containing $PrP_{106–126}$ were acquired at higher power settings than those measured from the pure hIAPP solution. Therefore, the saturation of the band can lead to an erroneous assignment of β-hairpin motif.

Similar to hIAPP:$PrP_{106–126}$ heterodimers, the spectroscopy results suggest that rIAPP and $PrP_{106–126}$ also associate into α-helix-rich structure. Moreover, the spectral features displayed by the rIAPP monomers indicate different hydrogen networks in the individual species. The lower vibrational frequency possibly indicates a higher extent of hydrogen bonding within a helical-rich structure.

The differences in the spectra of the hIAPP and rIAPP monomers measured from the pure and $PrP_{106–126}$-containing solution imply that an equilibrium exists between the heterodimers and monomers in solution. After association, the $PrP_{106–126}$ seems to induce the formation of new structures as well as structural changes in hIAPP and rIAPP monomers as indicated by shifts in the absorption frequencies.

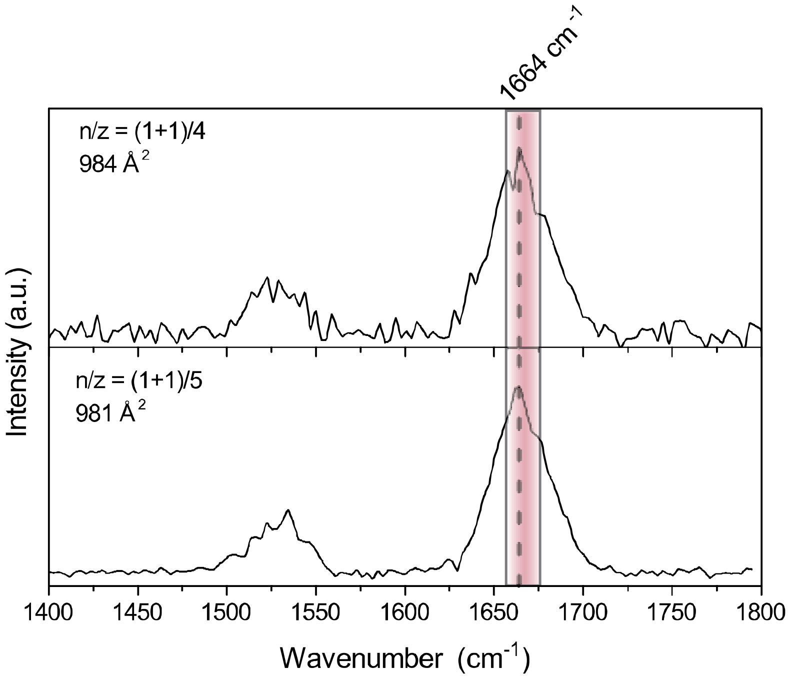

Figure 42. IRMPD spectra of *m/z*- and conformer-selected hIAPP-PrP$_{106\text{–}126}$ heterodimers. The region colored in pink demarcates the typical absorption region for α-helix secondary structure.

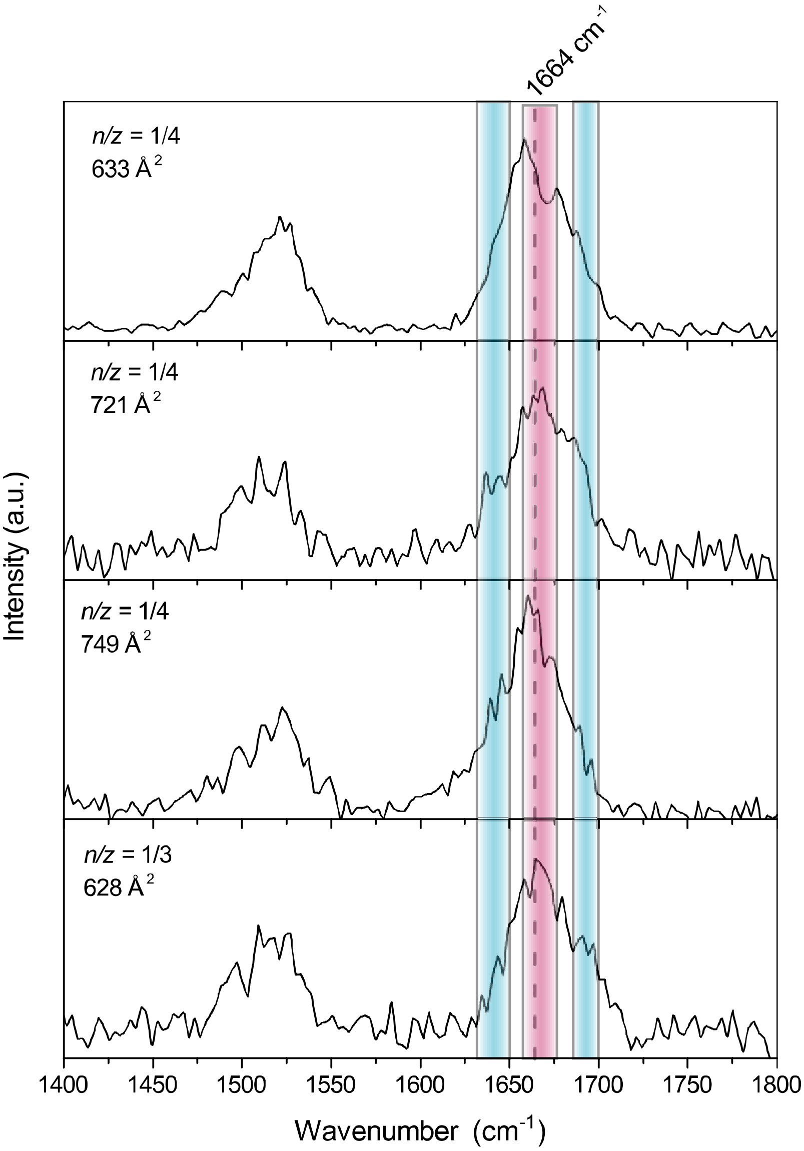

Figure 43. IRMPD spectra of *m/z*- and conformer-selected hIAPP monomers measured from the $PrP_{106-126}$-containing solution. The regions colored in blue and pink demarcate the typical absorption regions for β-sheet and α-helix secondary structures, respectively.

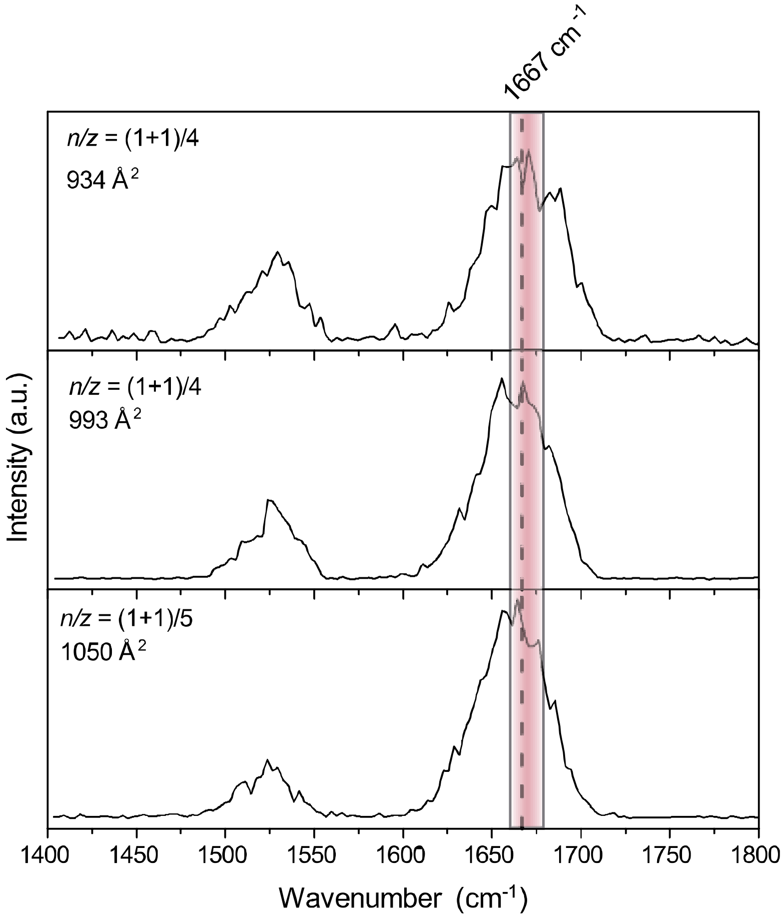

Figure 44. IRMPD spectra of *m/z*- and conformer-selected rIAPP-PrP $_{106–126}$ heterodimers. The region colored in pink demarcates the typical absorption region for α-helix secondary structure.

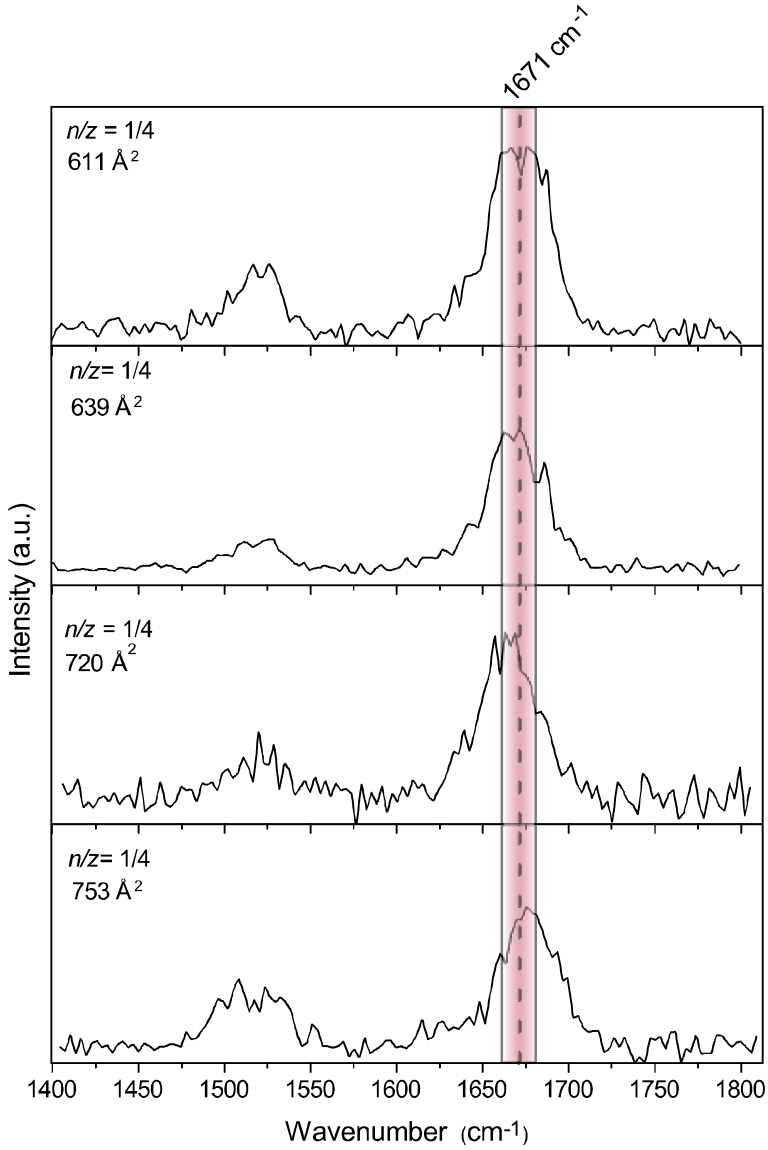

Figure 45. IRMPD spectra of *m/z*- and conformer-selected rIAPP monomers measured from the $PrP_{106-126}$-containing solution. The region colored in pink demarcates the typical absorption region for α-helix secondary structure.

Here we show the advantage of performing IR spectroscopy of *m/z*- and conformer-selected oligomers. Although both peptides show additional structural families of similar cross sections in the presence of PrP, we prove differences between the secondary structures adopted by the distinct conformers. While the most extended hIAPP monomer absorbs at 1664 cm^{-1}, indicating mainly α-helix structures, the most extended rIAPP conformer absorbs at 1677 cm^{-1}, suggesting that this species is predominantly composed by turn-like structures.

4.4.2 HIAPP:VEALYL

Insulin is a hormone cosecreted and coregulated at the expression level with hIAPP. Both peptides share the same secretory pathway in the pancreatic β-cells and have have complementary hormone activities. The inhibitory effect of insulin on hIAPP aggregation *in vitro* has previously been reported and the hIAPP/insulin co-assembly is believed to play an important role in type II diabetes. AFM studies on hIAPP/insulin co-assembly revealed distinctly different fibrillary structures formed by hIAPP in the absence and presence of insulin and these are insulin concentration-dependent.[98] Yet little is known about the mechanism of inhibition and which hIAPP intermediate oligomers are target by insulin peptides. Insulin is composed of an A-chain (IAC) and a longer B-chain (IBC) which includes the high amyloidogenic 12–17 VEALYL sequence. Here we investigate the hIAPP:VEALYL co-assembly using IM-MS and gas-phase IR spectroscopy.

In addition to the singly protonated VEALYL and the hIAPP monomers, the measured mass spectrum shows also the $[\text{hIAPP+VEALYL}]^{+3}$, $[\text{hIAPP+VEALYL}]^{+4}$ and $[\text{2hIAPP+VEALYL}]^{+5}$ heterodimers. The measured ATDs of the *m/z*- selected species are shown in Figure 46. The +3 ion ATD was fitted with a single structure with cross section of 673 Å^2 and two main structural families with cross sections of 698 and 734 Å^2 provided the best fit for the +4 ATD.

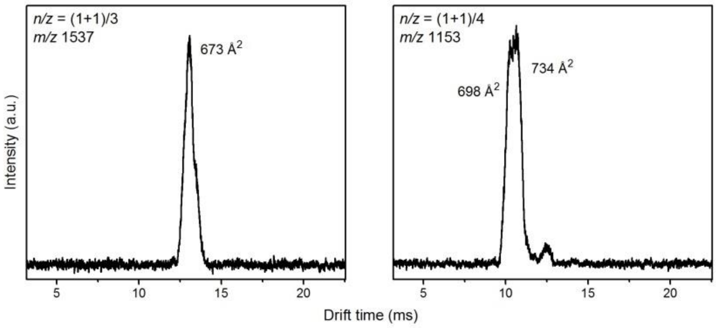

Figure 46. ATDs of *m/z*- selected hIAPP:VEALYL heterodimers.

To obtain structural details on the formed heterodimer, we measured the IR spectrum of *m/z*- and drift-time-selected heterodimer at the +3 charge state (Figure 47). The other two heterodimers observed in the mass spectrum were not detected in a measurable quantity to perform IRMPD spectroscopy. The spectrum shows a narrow and symmetric amide I band centered at 1666 cm^{-1}. This vibrational frequency matches with the position of the band of the model peptide polyalanine.

The spectroscopy data suggests that the helical fraction within the peptide is preserved during its association with VEALYL. Hetero-oligomerization occurs upon formation of intrapeptide hydrogen bondings at the interface between the peptides, and consequently the additional perturbation on the C=O bonds shifts the vibrational frequency to lower wavenumbers. Estimation of helical conformations within the molecule is in agreement with reported simulations on the heterodimer and with the inhibitory mechanism of aggregation by insulin previously proposed.[99] By forming the helix/helix hIAPP:insulin complex, the oligomerization pathway is shifted away from the formation of β-sheet rich oligomers and occasionally the β-barrel toxic structures., thus preventing aggregation.

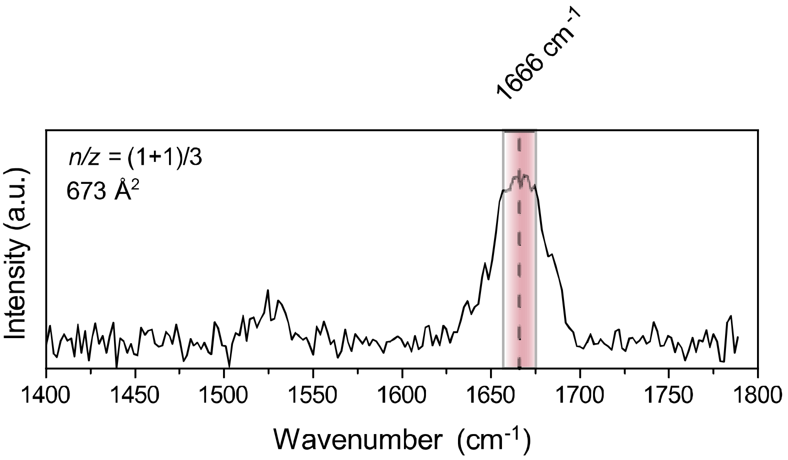

Figure 47. IRMPD spectrum of *m/z*- and conformer-selected [hIAPP+VEALYL]$^{+3}$ heterodimer.

5. CONCLUSION AND OUTLOOK

Type 2 diabetes mellitus is a systemic disorder that affects millions of people around the world. Along with insulin resistance, pathophysiological aggregation of hIAPP is a hallmark of this disease. The amyloid hypothesis associates the amyloid formation with loss of pancreatic β-cell mass. However, the underlying mechanism of aggregation is barely understood to date. The aim of this thesis was to investigate the gas-phase secondary structure of early hIAPP oligomers using ion mobility spectrometry in combination with IR spectroscopy in the gas phase.

Selected hIAPP monomers and dimers from the soluble ensemble were investigated in the gas phase. In previous ion mobility spectrometry studies, a β-hairpin conformation has been assigned to the extended +4 monomeric ion. In contrast, the non-amyloidogenic rIAPP ions were reported to consist mainly of random coil and turn-like structures. The typical IR spectral signature for β-sheet secondary structures is an absorption band around 1630 cm^{-1} (for parallel β-sheet) and a second band around 1690 cm^{-1} (for antiparallel β-sheet). Yet, a β-hairpin IR signature could, not be unambiguously assigned to the IR spectra of the investigated hIAPP species. Nevertheless, the extended +4 monomer and also the investigated dimer show a systematic shift to lower wavenumbers in relation to the +3 monomer indicating a difference in the structure of these ions.

Recent research has speculated the role of transition metals and other peptides in inducing structural transitions in hIAPP and in interfering in its aggregation pathway. Therefore, *m/z*- and conformer-selected of metal-associated hIAPP and heterodimeric ions were interrogated with IR radiation. By comparing the IR spectrum of metal-free hIAPP and metal-hIAPP adducts, coordination with Zn and Cu ions do not seem to induce any significant changes in the secondary structure within the monomers. Moreover, although different interaction modes and mechanisms of aggregation induced by metal-binding have been proposed for both Zn and Cu, Zn- and Cu-hIAPP show a comparable IR signature suggesting similarities in their secondary structure.

Possible changes in the secondary structures resulting from interaction with a fragment of the prion protein and with the hexapeptide VEALYL of the protein insulin were investigated. Both $PrP_{106–126}$ and insulin have been reported to have an impact on hIAPP aggregation. In the investigated species, the heterogeneous co-assembly does not induce significant changes in the secondary structure of hIAPP. The IR spectra of the heterodimers are comparable to the IR spectra of pure hIAPP. Yet, an interesting observation can be made: additional features appear in the IR spectra of the hIAPP monomers ionized from solutions containing $\text{PrP}_{106–126}$. Absorptions at lower and higher vibrational frequencies possibly suggest the transition to a β-sheet-like structure in these species.

ATR-FTIR is an established analytical method to follow the aggregation pathway and secondary structure transition of amyloidogenic peptides in condensed phase. The solution-phase IR spectrum of hIAPP was acquired over 24. The experimental data show that the soluble intermediate oligomers were mainly composed of random-coils and α-helical structures, whereas the insoluble fibrils are mainly composed of β-sheet motifs. In contrast but in agreement with previous publications, the ATR-FTIR spectrum of rIAPP did not suggest any change in secondary structure.

To date, two mechanisms for hIAPP aggregation have been proposed. The first suggests that a large-scale conformational transition from disordered oligomers to highly ordered β-sheet-rich oligomers occurs during the last stages of the aggregation pathway.[100] The second possible mechanism, referred as the “early conformation transition” proposes that a transition to β-sheet structures occurs before nucleation. The results obtained in this work reveal significant contributions of α-helical structural families within the hIAPP monomers and dimers. Recent theoretical work predicts that transition to β-sheet becomes significant starting from hexamers. In order to identify which of the two proposed mechanism takes place, more information on the secondary structure of higher-order oligomers is necessary.

Signatures of β-sheets and β-hairpins, as these are known from classical solution-phase approaches, were also not observed for the model molecules investigated in this thesis. These have well-defined and intensively studied secondary structures in solution. The results suggest that the absence of a β-sheet signature in the IRMPD spectra does not necessarily correlate with the lack of β-sheet motifs in solution. Even though nESI is a soft-ionization method, the native-like structures of these molecules are possibly lost and β-sheet conformations are destabilized during transfer into the gas-phase. In this case, optimization of the experimental conditions that preserve the secondary structure of the peptides could increase the population of the native-like conformations, making their interrogation with laser light possible.

Conformational changes within the molecule could also arise from the IRMPD process. The increase in internal energy due to the sequential absorption of photons might lead not only to bond breakage but to the loss of the β-sheet-like motifs. Consequently, the segments of the molecule that undergo conformational transitions will no longer absorb IR light during the process. This can be overcome by using methods that use other types of action such as cold-ion IR spectroscopy in helium nano-droplets. In conclusion, further research is necessary to solve the “chicken-and-egg” problem, whether hIAPP aggregation causes the β-cell dysfunction or is a consequence of the disease.

6. LITERATURE

[1] D. EISENBERG, M. JUCKER, *CELL* **2012**, *148*, 1188-1203.
[2] S. M. BUTTERFIELD, H. A. LASHUEL, *ANGEWANDTE CHEMIE INTERNATIONAL EDITION* **2010**, *49*, 5628-5654.
[3] C. SOTO, NATURE REVIEWS NEUROSCIENCE **2003**, 4, 49-60.
[4] A. ABEDINI, A. PLESNER, P. CAO, Z. RIDGWAY, J. ZHANG, L.-H. TU, C. T. MIDDLETON, B. CHAO, D. J. SARTORI, F. MENG, H. WANG, A. G. WONG, M. T. ZANNI, C. B. VERCHERE, D. P. RALEIGH, A. M. SCHMIDT, *ELIFE* **2016**, *5*, E12977.
[5] W. HOFFMANN, G. VON HELDEN, K. PAGEL, *CURRENT OPINION IN STRUCTURAL BIOLOGY* **2017**, *46*, 7-15.
[6] S. D. MORAN, M. T. ZANNI, *THE JOURNAL OF PHYSICAL CHEMISTRY LETTERS* **2014**, *5*, 1984-1993.
[7] J. SEO, W. HOFFMANN, S. WARNKE, X. HUANG, S. GEWINNER, W. SCHÖLLKOPF, M. T. BOWERS, G. VON HELDEN, K. PAGEL, *NATURE CHEMISTRY* **2016**, *9*, 39.
[8] N. F. DUPUIS, C. WU, J.-E. SHEA, M. T. BOWERS, *JOURNAL OF THE AMERICAN CHEMICAL SOCIETY* **2009**, *131*, 18283-18292.
[9] C. UETRECHT, R. J. ROSE, E. VAN DUIJN, K. LORENZEN, A. J. R. HECK, *CHEMICAL SOCIETY REVIEWS* **2010**, *39*, 1633-1655.
[10] L. HAATAJA, T. GURLO, C. J. HUANG, P. C. BUTLER, *ENDOCRINE REVIEWS* **2008**, *29*, 303-316.
[11] M. ALGHRABLY, I. CZABAN, Ł. JAREMKO, M. JAREMKO, *JOURNAL OF INORGANIC BIOCHEMISTRY* **2019**, *191*, 69-76.
[12] J. D. SIPE, A. S. COHEN, *JOURNAL OF STRUCTURAL BIOLOGY* **2000**, *130*, 88-98.
[13] M. FÄNDRICH, V. FORGE, K. BUDER, M. KITTLER, C. M. DOBSON, S. DIEKMANN, *PROCEEDINGS OF THE NATIONAL ACADEMY OF SCIENCES* **2003**, *100*, 15463.
[14] R. NELSON, M. R. SAWAYA, M. BALBIRNIE, A. Ø. MADSEN, C. RIEKEL, R. GROTHE, D. EISENBERG, *NATURE* **2005**, *435*, 773-778.
[15] L. A. WOODS, S. E. RADFORD, A. E. ASHCROFT, *BIOCHIMICA ET BIOPHYSICA ACTA (BBA) - PROTEINS AND PROTEOMICS* **2013**, *1834*, 1257-1268.
[16] M. C. OWEN, D. GNUTT, M. GAO, S. K. T. S. WÄRMLÄNDER, J. JARVET, A. GRÄSLUND, R. WINTER, S. EBBINGHAUS, B. STRODEL, *CHEMICAL SOCIETY REVIEWS* **2019**.
[17] J.-X. LU, W. QIANG, W.-M. YAU, CHARLES D. SCHWIETERS, STEPHEN C. MEREDITH, R. TYCKO, *CELL* **2013**, *154*, 1257-1268.
[18] T. SANKE, G. I. BELL, C. SAMPLE, A. H. RUBENSTEIN, D. F. STEINER, *JOURNAL OF BIOLOGICAL CHEMISTRY* **1988**, *263*, 17243-17246.
[19] P. CAO, P. MAREK, H. NOOR, V. PATSALO, L.-H. TU, H. WANG, A. ABEDINI, D. P. RALEIGH, *FEBS LETTERS* **2013**, *587*, 1106-1118.
[20] P. WESTERMARK, A. ANDERSSON, G. T. WESTERMARK, *PHYSIOLOGICAL REVIEWS* **2011**, *91*, 795-826.
[21] T. A. LUTZ, CELLULAR AND MOLECULAR LIFE SCIENCES **2012**, 69, 1947-1965.
[22] A. YOUNG, IN *ADVANCES IN PHARMACOLOGY, VOL. 52*, ACADEMIC PRESS, **2005**, PP. 151-171.
[23] M. STRIDSBERG, C. BERNE, S. SANDLER, E. WILANDER, K. ÖBERG, *DIABETOLOGIA* **1993**, *36*, 843-849.

[24] M. Pettersson, B. Ahrén, *Acta Physiologica Scandinavica* **1990**, *138*, 389-394.

[25] J. D. Knight, J. A. Williamson, A. D. Miranker, *Protein Sci* **2008**, *17*, 1850-1856.

[26] P. Westermark, Z.-C. Li, G. T. Westermark, A. Leckström, D. F. Steiner, *FEBS Letters* **1996**, *379*, 203-206.

[27] G. T. Westermark, D. F. Steiner, S. Gebre-Medhin, U. Engström, P. Westermark, *Upsala Journal of Medical Sciences* **2000**, *105*, 97-106.

[28] J. D. Knight, A. D. Miranker, *Journal of Molecular Biology* **2004**, *341*, 1175-1187.

[29] X. Zhang, J. R. St. Clair, E. London, D. P. Raleigh, *Biochemistry* **2017**, *56*, 376-390.

[30] M. F. M. Sciacca, J. R. Brender, D.-K. Lee, A. Ramamoorthy, *Biochemistry* **2012**, *51*, 7676-7684.

[31] J. A. Williamson, J. P. Loria, A. D. Miranker, *Journal of Molecular Biology* **2009**, *393*, 383-396.

[32] Y. A. Domanov, P. K. J. Kinnunen, *Journal of Molecular Biology* **2008**, *376*, 42-54.

[33] M. F. M. Engel, Chemistry and Physics of Lipids **2009**, 160, 1-10.

[34] S. Luca, W.-M. Yau, R. Leapman, R. Tycko, *Biochemistry* **2007**, *46*, 13505-13522.

[35] J. J. W. Wiltzius, S. A. Sievers, M. R. Sawaya, D. Eisenberg, *Protein Sci* **2009**, *18*, 1521-1530.

[36] W. Hoffmann, K. Folmert, J. Moschner, X. Huang, H. von Berlepsch, B. Koksch, M. T. Bowers, G. von Helden, K. Pagel, *Journal of the American Chemical Society* **2018**, *140*, 244-249.

[37] A. L. Serrano, J. P. Lomont, L.-H. Tu, D. P. Raleigh, M. T. Zanni, *Journal of the American Chemical Society* **2017**, *139*, 16748-16758.

[38] L. E. Buchanan, E. B. Dunkelberger, H. Q. Tran, P.-N. Cheng, C.-C. Chiu, P. Cao, D. P. Raleigh, J. J. de Pablo, J. S. Nowick, M. T. Zanni, *Proceedings of the National Academy of Sciences* **2013**, *110*, 19285-19290.

[39] L. M. Young, P. Cao, D. P. Raleigh, A. E. Ashcroft, S. E. Radford, *Journal of the American Chemical Society* **2014**, *136*, 660-670.

[40] G. Nardai, T. Korcsmáros, E. Papp, P. Csermely, *BioFactors* **2003**, *17*, 259-267.

[41] D. C. Rodriguez Camargo, K. Tripsianes, K. Buday, A. Franko, C. Göbl, C. Hartlmüller, R. Sarkar, M. Aichler, G. Mettenleiter, M. Schulz, A. Böddrich, C. Erck, H. Martens, A. K. Walch, T. Madl, E. E. Wanker, M. Conrad, M. H. de Angelis, B. Reif, *Scientific Reports* **2017**, *7*, 44041.

[42] J. A. Williamson, A. D. Miranker, *Protein Sci* **2007**, *16*, 110-117.

[43] R. P. R. Nanga, J. R. Brender, S. Vivekanandan, A. Ramamoorthy, *Biochimica et Biophysica Acta (BBA) - Biomembranes* **2011**, *1808*, 2337-2342.

[44] N. F. Dupuis, C. Wu, J.-E. Shea, M. T. Bowers, *Journal of the American Chemical Society* **2011**, *133*, 7240-7243.

[45] R. Kayed, J. Bernhagen, N. Greenfield, K. Sweimeh, H. Brunner, W. Voelter, A. Kapurniotu, *Journal of Molecular Biology* **1999**, *287*, 781-796.

[46] S.-H. Shim, R. Gupta, Y. L. Ling, D. B. Strasfeld, D. P. Raleigh, M. T. Zanni, *Proceedings of the National Academy of Sciences* **2009**, *106*, 6614.
[47] A. S. Reddy, L. Wang, S. Singh, Y. L. Ling, L. Buchanan, M. T. Zanni, J. L. Skinner, J. J. de Pablo, *Biophysical Journal* **2010**, *99*, 2208-2216.
[48] Y. Sun, A. Kakinen, Y. Xing, E. H. Pilkington, T. P. Davis, P. C. Ke, F. Ding, *Biochimica et Biophysica Acta (BBA) - Molecular Basis of Disease* **2019**, *1865*, 434-444.
[49] Y. Sun, A. Kakinen, Y. Xing, P. Faridi, A. Nandakumar, A. W. Purcell, T. P. Davis, P. C. Ke, F. Ding, *Small* **2019**, *15*, 1805166.
[50] A. Laganowsky, C. Liu, M. R. Sawaya, J. P. Whitelegge, J. Park, M. Zhao, A. Pensalfini, A. B. Soriaga, M. Landau, P. K. Teng, D. Cascio, C. Glabe, D. Eisenberg, *Science* **2012**, *335*, 1228.
[51] T. D. Do, N. E. LaPointe, R. Nelson, P. Krotee, E. Y. Hayden, B. Ulrich, S. Quan, S. C. Feinstein, D. B. Teplow, D. Eisenberg, J.-E. Shea, M. T. Bowers, *Journal of the American Chemical Society* **2016**, *138*, 549-557.
[52] Y. Sun, B. Wang, X. Ge, F. Ding, *Physical Chemistry Chemical Physics* **2017**, *19*, 28414-28423.
[53] A. Quist, I. Doudevski, H. Lin, R. Azimova, D. Ng, B. Frangione, B. Kagan, J. Ghiso, R. Lal, *Proceedings of the National Academy of Sciences of the United States of America* **2005**, *102*, 10427.
[54] C. S. Goldsbury, G. J. S. Cooper, K. N. Goldie, S. A. Müller, E. L. Saafi, W. T. M. Gruijters, M. P. Misur, A. Engel, U. Aebi, J. Kistler, *Journal of Structural Biology* **1997**, *119*, 17-27.
[55] J. R. Brender, E. L. Lee, K. Hartman, P. T. Wong, A. Ramamoorthy, D. G. Steel, A. Gafni, *Biophysical journal* **2011**, *100*, 685-692.
[56] A. I. Ilitchev, M. J. Giammona, J. N. Schwarze, S. K. Buratto, M. T. Bowers, *The Journal of Physical Chemistry B* **2018**, *122*, 9852-9859.
[57] S. Salamekh, J. R. Brender, S.-J. Hyung, R. P. R. Nanga, S. Vivekanandan, B. T. Ruotolo, A. Ramamoorthy, *Journal of Molecular Biology* **2011**, *410*, 294-306.
[58] E. Atrián-Blasco, P. Gonzalez, A. Santoro, B. Alies, P. Faller, C. Hureau, *Coordination Chemistry Reviews* **2018**, *371*, 38-55.
[59] M. Rowińska-Żyrek, *Dalton Transactions* **2016**, *45*, 8099-8106.
[60] J. R. Brender, K. Hartman, R. P. R. Nanga, N. Popovych, R. de la Salud Bea, S. Vivekanandan, E. N. G. Marsh, A. Ramamoorthy, *Journal of the American Chemical Society* **2010**, *132*, 8973-8983.
[61] J. R. Brender, J. Krishnamoorthy, G. M. L. Messina, A. Deb, S. Vivekanandan, C. La Rosa, J. E. Penner-Hahn, A. Ramamoorthy, *Chemical Communications* **2013**, *49*, 3339-3341.
[62] P. Nedumpully-Govindan, Y. Yang, R. Andorfer, W. Cao, F. Ding, *Biochemistry* **2015**, *54*, 7335-7344.
[63] A. Masad, L. Hayes, B. J. Tabner, S. Turnbull, L. J. Cooper, N. J. Fullwood, M. J. German, F. Kametani, O. M. A. El-Agnaf, D. Allsop, *FEBS Letters* **2007**, *581*, 3489-3493.
[64] Y.-P. Yu, P. Lei, J. Hu, W.-H. Wu, Y.-F. Zhao, Y.-M. Li, *Chemical Communications* **2010**, *46*, 6909-6911.

[65] I. Riba, P. E. Barran, G. J. S. Cooper, R. D. Unwin, *International Journal of Mass Spectrometry* **2015**, *391*, 47-53.

[66] C. Sánchez-López, R. Cortés-Mejía, M. C. Miotto, A. Binolfi, C. O. Fernández, J. M. del Campo, L. Quintanar, *Inorganic Chemistry* **2016**, *55*, 10727-10740.

[67] S. J. C. Lee, T. S. Choi, J. W. Lee, H. J. Lee, D.-G. Mun, S. Akashi, S.-W. Lee, M. H. Lim, H. I. Kim, *Chemical Science* **2016**, *7*, 5398-5406.

[68] M.-J. Kim, H.-T. Kim, *European Journal of Mass Spectrometry* **2012**, *18*, 51-58.

[69] A. Magrì, D. La Mendola, V. G. Nicoletti, G. Pappalardo, E. Rizzarelli, *Chemistry – A European Journal* **2016**, *22*, 13287-13300.

[70] H. Li, E. Ha, R. P. Donaldson, A. M. Jeremic, A. Vertes, *Analytical Chemistry* **2015**, *87*, 9829-9837.

[71] in Fourier Transform Infrared Spectrometry, pp. 19-55.

[72] A. Barth, Biochimica et Biophysica Acta (BBA) - Bioenergetics **2007**, 1767, 1073-1101.

[73] in Fourier Transform Infrared Spectrometry, pp. 321-348.

[74] S. E. Glassford, B. Byrne, S. G. Kazarian, *Biochimica et Biophysica Acta (BBA) - Proteins and Proteomics* **2013**, *1834*, 2849-2858.

[75] A. M. Rijs, J. L. Alonso, Gas-phase IR spectroscopy and structure of biological molecules / Anouk M. Rijs
... eds. With contributions by J. L. Alonso, Springer, Cham [u.a.], **2015**.

[76] J. Oomens, B. G. Sartakov, G. Meijer, G. von Helden, *International Journal of Mass Spectrometry* **2006**, *254*, 1-19.

[77] P. Y. Chou, G. D. Fasman, *Biochemistry* **1974**, *13*, 222-245.

[78] M. F. Jarrold, *Physical Chemistry Chemical Physics* **2007**, *9*, 1659-1671.

[79] R. R. Hudgins, M. A. Ratner, M. F. Jarrold, *Journal of the American Chemical Society* **1998**, *120*, 12974-12975.

[80] F. Schubert, M. Rossi, C. Baldauf, K. Pagel, S. Warnke, G. von Helden, F. Filsinger, P. Kupser, G. Meijer, M. Salwiczek, B. Koksch, M. Scheffler, V. Blum, *Physical Chemistry Chemical Physics* **2015**, *17*, 7373-7385.

[81] M. Rossi, V. Blum, P. Kupser, G. von Helden, F. Bierau, K. Pagel, G. Meijer, M. Scheffler, *The Journal of Physical Chemistry Letters* **2010**, *1*, 3465-3470.

[82] L. VÉRtesy, V. Oeding, R. Bender, K. Zepf, G. Nesemann, *European Journal of Biochemistry* **1984**, *141*, 505-512.

[83] A. D. Kline, W. Braun, K. Wüthrich, *Journal of Molecular Biology* **1988**, *204*, 675-724.

[84] S. Warnke, G. von Helden, K. Pagel, *Journal of the American Chemical Society* **2013**, *135*, 1177-1180.

[85] C. Zscherp, H. Aygün, J. W. Engels, W. Mäntele, *Biochimica et Biophysica Acta (BBA) - Proteins and Proteomics* **2003**, *1651*, 139-145.

[86] H. Jang, Fernando T. Arce, M. Mustata, S. Ramachandran, R. Capone, R. Nussinov, R. Lal, *Biophysical Journal* **2011**, *100*, 1775-1783.

[87] S. S. L. Harwig, A. Waring, H. J. Yang, Y. Cho, L. Tan, R. I. Lehrer, *European Journal of Biochemistry* **1996**, *240*, 352-357.

[88] D. Gidalevitz, Y. Ishitsuka, A. S. Muresan, O. Konovalov, A. J. Waring, R. I. Lehrer, K. Y. C. Lee, *Proceedings of the National Academy of Sciences of the United States of America* **2003**, *100*, 6302-6307.

[89] W. T. Heller, A. J. Waring, R. I. Lehrer, H. W. Huang, *Biochemistry* **1998**, *37*, 17331-17338.

[90] R. Capone, M. Mustata, H. Jang, F. T. Arce, R. Nussinov, R. Lal, *Biophysical Journal* **2010**, *98*, 2644-2652.

[91] M. Svoboda, W. Meister, W. Vetter, *Journal of Mass Spectrometry* **1995**, *30*, 1562-1566.

[92] R. R. Julian, M. Akin, J. A. May, B. M. Stoltz, J. L. Beauchamp, *International Journal of Mass Spectrometry* **2002**, *220*, 87-96.

[93] R. L. Fahrner, T. Dieckmann, S. S. L. Harwig, R. I. Lehrer, D. Eisenberg, J. Feigon, *Chemistry & Biology* **1996**, *3*, 543-550.

[94] H. Jang, B. Ma, R. Nussinov, *BMC Structural Biology* **2007**, *7*, 21.

[95] J. Kubelka, T. A. Keiderling, *Journal of the American Chemical Society* **2001**, *123*, 12048-12058.

[96] A. E. Butler, J. Jang, T. Gurlo, M. D. Carty, W. C. Soeller, P. C. Butler, *A New Model for Type 2 Diabetes* **2004**, *53*, 1509-1516.

[97] A. I. Ilitchev, M. J. Giammona, C. Olivas, S. L. Claud, K. L. Lazar Cantrell, C. Wu, S. K. Buratto, M. T. Bowers, *Journal of the American Chemical Society* **2018**, *140*, 9685-9695.

[98] P. Liu, S. Zhang, M.-s. Chen, Q. Liu, C. Wang, C. Wang, Y.-M. Li, F. Besenbacher, M. Dong, *Chemical Communications* **2012**, *48*, 191-193.

[99] A. C. Susa, C. Wu, S. L. Bernstein, N. F. Dupuis, H. Wang, D. P. Raleigh, J.-E. Shea, M. T. Bowers, *Journal of the American Chemical Society* **2014**, *136*, 12912-12919.

[100] F. Chiti, C. M. Dobson, *Annual Review of Biochemistry* **2006**, *75*, 333-366.

7. APPENDIX

Table A1. Correlations between amide I frequencies and secondary structure[72].

Secondary structure	Amide I band (cm^{-1})
Aggressed strands	1620–1628
β-sheet	1610–1640
Random coil	1640–1648
α-Helix	1648–1660
3_{10}-Helix, type II β-turn	1660–1685
Antiparallel β-sheet and aggregated strands	1675–1695

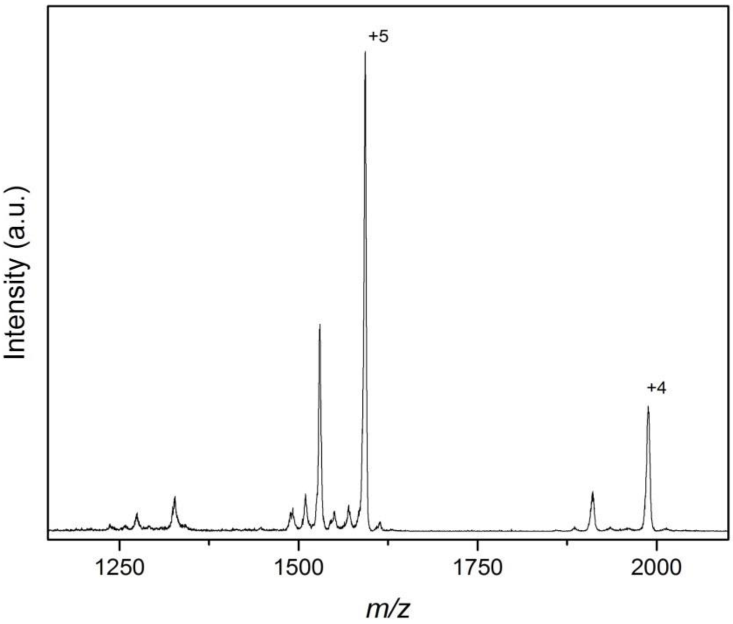

A1. nESI time-of-flight of tendamistat solution.

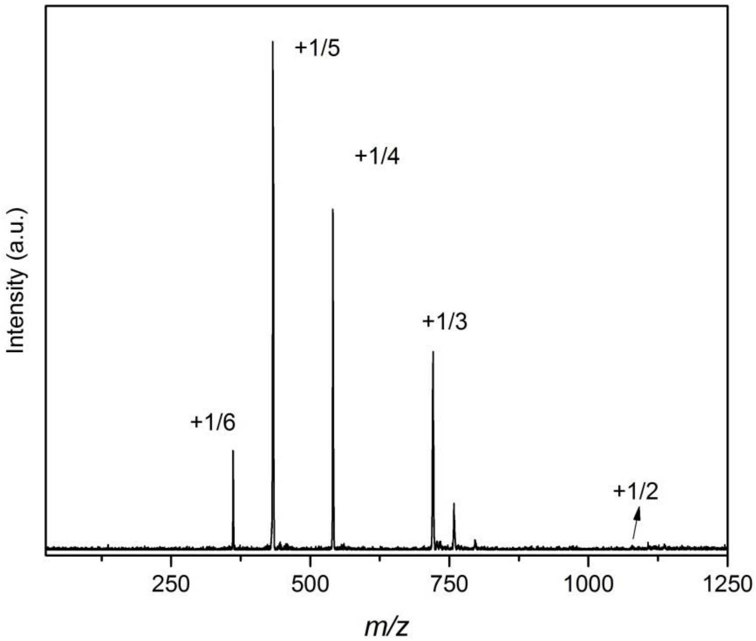

A2. nESI time-of-flight of PG-1 solution.

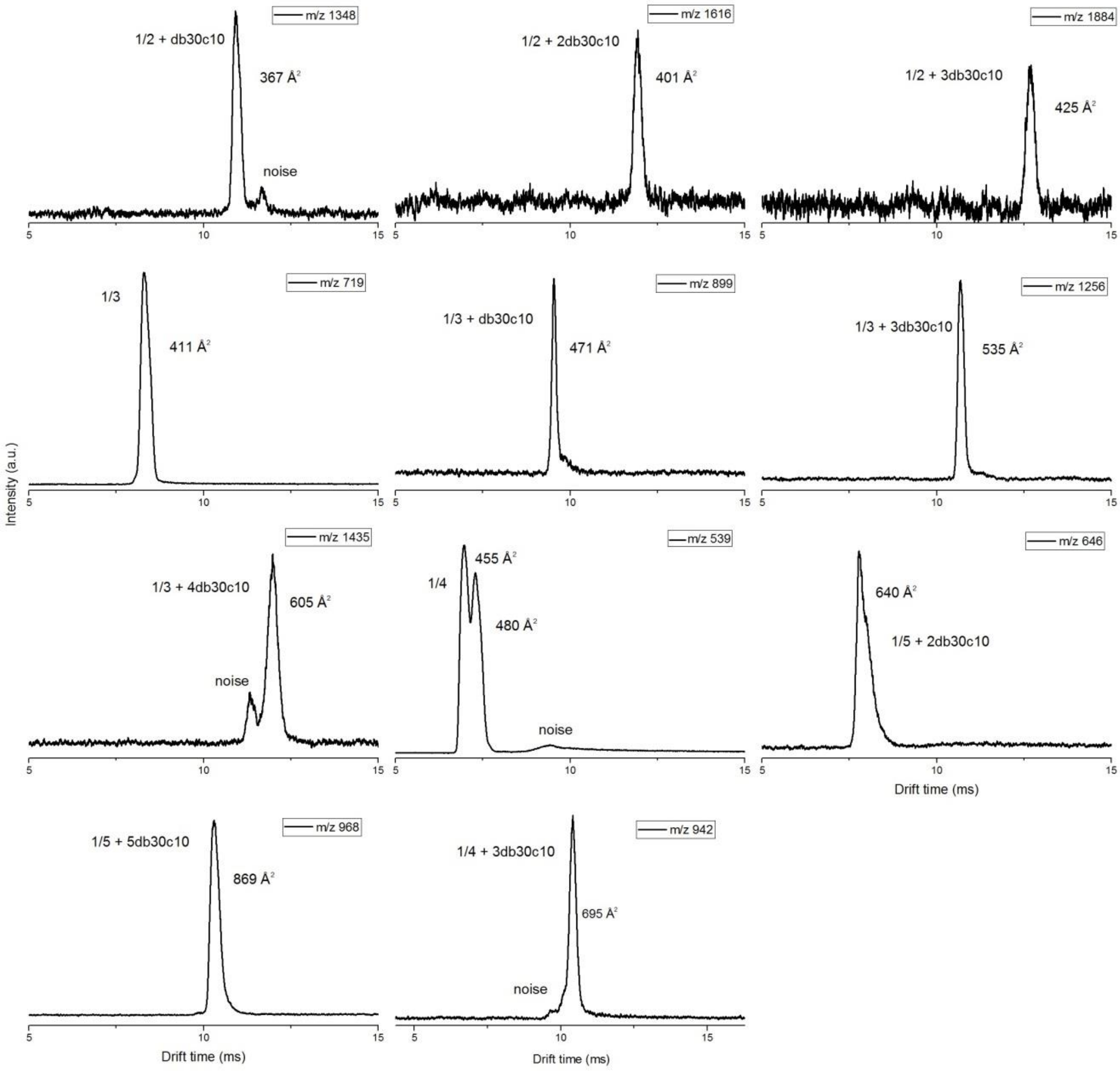

A3. ATDs of PG-1 and PG-1-db30c10 adducts. All the ATDs were obtained from the solution containing crown ether.

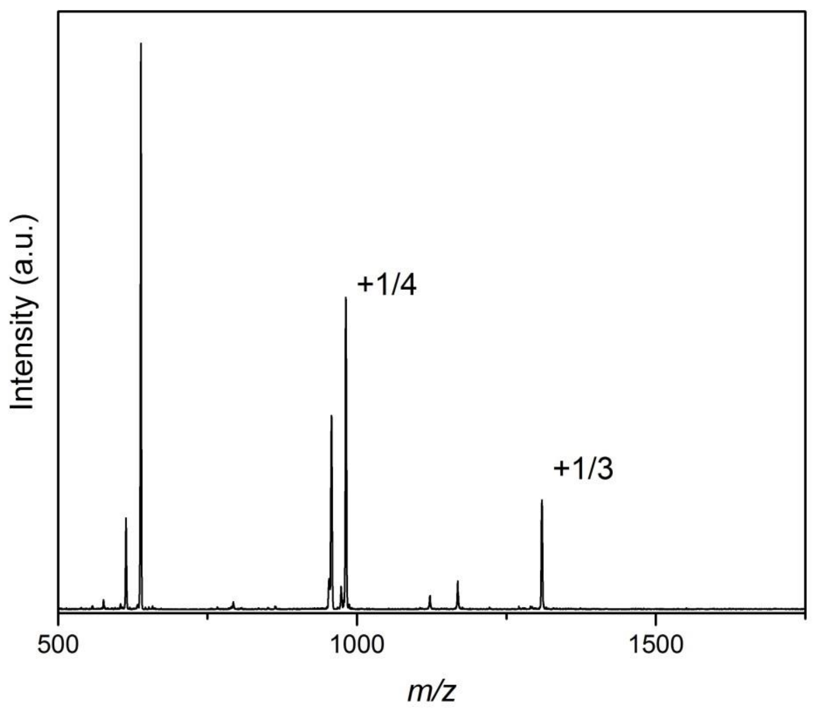

A4. nESI time-of-flight of rIAPP solution.

Table A2. CCS of the PG-1-db30c10 adducts

n	z	n. of db30c10	*m/z*	CCS (Å^2)
1	2	1	1348	367
1	2	2	1616	401
1	2	3	1884	425
1	3	1	899	471
1	3	3	1256	535
1	3	4	1435	605
1	5	2	646	640
1	5	5	968	869

$\text{PrP}_{106\text{-}126}$: KTNMKHMAGAAAAGAVVGGLG

A5. Primary sequence of $\text{PrP}_{106–126}$.

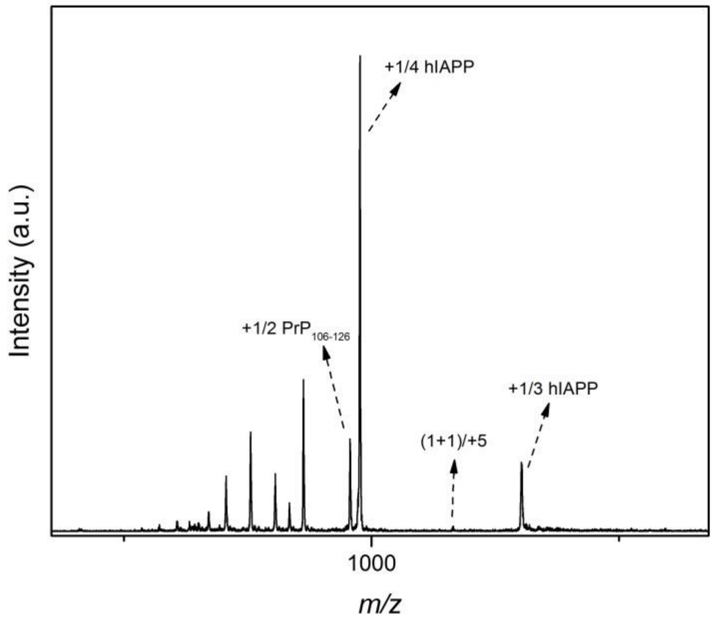

A6. nESI time-of-flight of the 25 μM: 25 μM solution hIAPP:$\text{PrP}_{106–126}$

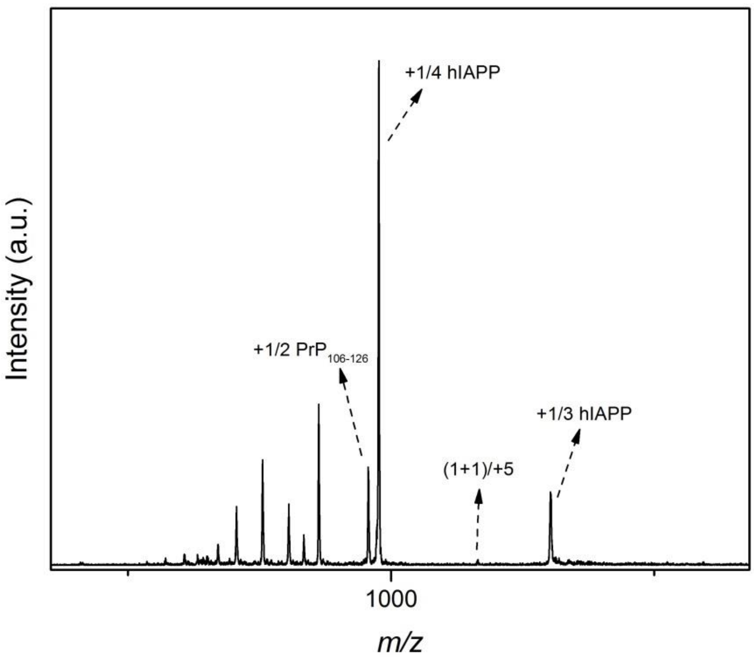

A7. nESI time-of-flight of the 25 μM: 25 μM solution rIAPP:PrP$_{106–126}$

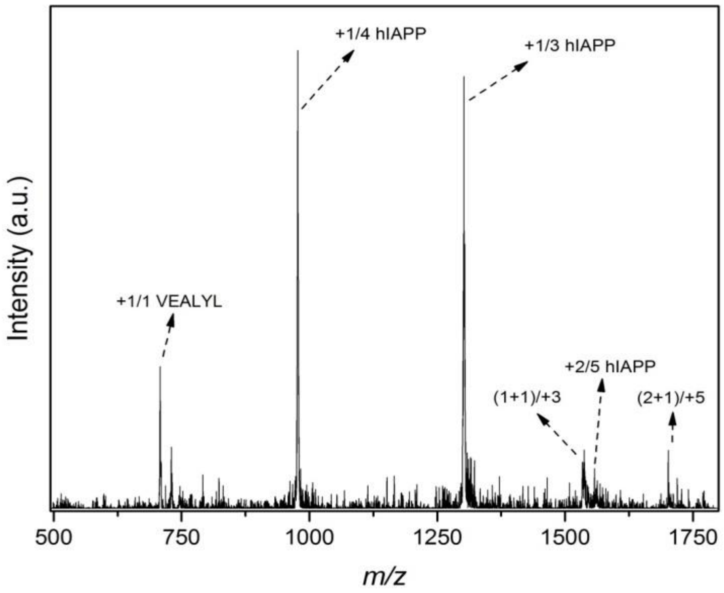

A8. nESI time-of-flight mass spectra of a 1:1 mixture of hIAPP and VEALYL.